Title

Mapping and Modeling of Fires in the Wildland-Urban Interface

Author

Kumar, Mukesh

Publication Date

2022

UNIVERSITY OF CALIFORNIA,
IRVINE

Mapping and Modeling of Fires in the Wildland-Urban Interface

DISSERTATION

submitted in partial satisfaction of the requirements
for the degree of

DOCTOR OF PHILOSOPHY

in Civil and Environmental Engineering

by

Mukesh Kumar

Dissertation Committee:
Assistant Professor Tirtha Banerjee, Chair
Professor James T. Randerson
Professor Amir AghaKouchak
Dr. Branko Kosović

2022

DEDICATION

This dissertation is dedicated to my parents. I am eternally grateful to my parents and siblings for being constant anchors in my life's journey so far. My successes and accomplishments would not have been possible without their unconditional support and sacrifice.

TABLE OF CONTENTS

LIST OF FIGURES

Page

LIST OF TABLES

ACKNOWLEDGMENTS

First and foremost, I would like to thank my advisor, Professor Tirtha Banerjee, for his support and guidance over the years. His knowledge and experience in the field of micrometeorology and turbulence was extremely valuable in identifying gaps in the existing research on wildfires and in the formulation of research ideas for my doctoral dissertation. His suggestions helped me polish my manuscripts and guided me in perceiving the bigger picture. His hardwork is exemplary and his dedication to scientific research has always been an inspiration to me.

I would like to thank my co-advisor, Professor James T. Randerson, for providing his thoughtful comments that helped me improve the quality of my work. His suggestions were very helpful in making my manuscripts more concise, clear, and accessible to the general audience. His wisdom will always be a guiding light for me in my future work as a scientific researcher. I would especially like to thank him for encouraging me to conduct scientific research that would positively impact humanity at large.

I would like to extend my gratitude to Professor Amir AghaKouchak and Dr. Branko Kosović for being a part of my doctoral committee. Dr. Branko Kosović was very meticulous in his attention to detail in our research discussions and meetings. He was also very influential in motivating me to obtain a deeper understanding of my research outcomes. I am particularly grateful to Professor Amir AghaKouchak for inspiring me with his work ethic and for instilling in me the confidence required for pursuing a successful career as a scientist.

I am much obliged to Dr. Maria E. Frediani for hosting me and supervising my research at NCAR. I would like to thank my collaborators, Dr. Alex Jonko, Dr. William Lassman, Dr. Jeff Mirocha, Dr. Hara Nayak, Dr. Timothy W. Juliano, Professor William Porter, Professor Phu Nguyen for their helpful insights and valuable suggestions during our project discussions. I also stand in recognition of the support that I received from Professor Russell Detwiler, Professor Gillian Hayes, and Professor Efi Foufoula-Georgiou during my sojourn as a Ph.D. student at UCI.

I appreciate the support and feedback that I have received on my work from my colleagues in the BLT Lab during our numerous discussions. I also thank Yang and Jin from the Randerson Lab for their help in troubleshooting roadblocks in my research.

I thank my friends Ajinkya, Mrityunjay, Avinash, Anmol, Keiland, Marina, Bayo, and Rohit for their moral support and words of comfort when the time were tough. I owe my deepest gratitude to my parents and siblings for being a constant anchor in my life's journey so far. Their loving support and sacrifices have played an indispensable role in my successes and achievements.

Finally, I would like to acknowledge the funding support that I received from the Dean's Dissertation Fellowship Award of the Henry Samueli School of Engineering at UCI. Furthermore, I would like to acknowledge funding support from the Research Applications Laboratory

Visitor Grant awarded to me by the National Center for Atmospheric Research (NCAR). I acknowledge the Los Alamos National Laboratory Institutional Computing Program and resources provided by NCAR's high-performance computing systems through the University Request Program under the project UCIR0048. I am grateful for the support from the publishers and co-authors of my Ph.D. research projects.

VITA

Mukesh Kumar

EDUCATION

Doctor of Philosophy in Civil and Environmental Engineering **2022**
University of California, Irvine

Master of Technology in Climate Science and Technology **2019**
Indian Institute of Technology (IIT), Bhubaneswar

Bachelor of Engineering in Mechanical Engineering **2017**
Rajiv Gandhi Proudyogiki Vishwavidyalaya, Bhopal

RESEARCH EXPERIENCE

Graduate Research Assistant **2019–2022**
University of California, Irvine

Research Intern **Jun 2022–Sep 2022**
LANL, Los Alamos, NM

Guest Scientist **Apr 2020–Jun 2022**
LANL, Los Alamos, NM

Graduate Visitor **May 2022–Jun 022**
NCAR, Boulder, CO

Research Intern **Jun 2018–Apr 2019**
Indian Institute of Tropical Meteorology, Pune

Research Intern **Summer 2015**
Bharat Heavy Electricals Limited, Bhopal

TEACHING EXPERIENCE

Teaching Assistant **Winter 2020**
University of California, Irvine

Lab Mentor for undergrads **Spring 2020–Spring2022**
BLT Lab, University of California, Irvine

Engineering Math & IIT-JEE Tutor **Oct 2013–Feb 2019**
Arrowhead Classes and UrbanPro

SCHOLARSHIPS & AWARDS

RAL Visitor Grant **May 2022**
Research Applications Laboratory (RAL), NCAR, Boulder, CO

Graduate Dean's Dissertation Fellowship Award **Apr 2022**
Graduate Division, University of California, Irvine

Semifinalist in Grad Slam Competition **Jan 2021**
Graduate Division, University of California, Irvine

International Travel Grant for EGU 2019 **Apr 2019**
MHRD, Government of India

Master's Degree Fellowship **Jul 2017–May 2019**
MHRD, Government of India

First Division with Honors in Mechanical Engineering **Jun 2017**
RGPV, Bhopal, India

ACADEMIC SERVICES

Peer Reviewer: Water Resources Research **Jan 2022–Present**
American Geophysical Union (AGU)

Mentor: Mentoring365 **Jan 2021–Present**
American Geophysical Union (AGU)

Volunteer: AGU 2022 **Dec 2022**
American Geophysical Union (AGU), Chicago

Students' Gymkhana: Elected Secretary of Hostel (Mess) **Apr 2018–Mar 2019**
IIT Bhubaneswar, India

REFEREED JOURNAL PUBLICATIONS

Kumar, M., Li, S., Nguyen, P. and Banerjee, T., 2020. Examining the existing definitions of wildland-urban interface for California. **2022**
Ecosphere; Wiley online library

Baijnath-Rodino, J.A., Kumar, M., Rivera, M., Tran, K.D. and Banerjee, T. How Vulnerable Are American States to Wildfires? A Livelihood Vulnerability Assessment, 4(3), p.54. **2021**
Fire

Li, S., Dao, V., Kumar, M., Nguyen, P. and Banerjee, T. Mapping the wildland-urban interface in California using remote sensing data, 12(1), pp.1-12 **2022**
Scientific reports
.

Baijnath-Rodino, J.A., Li, S., Martinez, A., Kumar, M., Quinn-Davidson, L.N., York, R.A. and Banerjee, T. Historical seasonal changes in prescribed burn windows in California, p.155723. **2022**
Science of the total environment

Haupt, S.E., Arthur, R., Decastro, A., Gagne, D.J., Jonko, A., Kosovic, B., Mccandless, T., Rai, R.K., Berg, L.K., Dettling, S., Hawbecker, P, Kumar, M., and co-authors. FY 2020 Report of the Atmosphere to Electrons Land-Based Mesoscale-to-Microscale Coupling Project (No. PNNL-30841). **2020**
Pacific Northwest National Lab. (PNNL), Richland, WA (United States)

PUBLICATIONS (UNDER REVIEW)

Kumar, M., Dao, V., Nguyen, P., Randerson, J., and Banerjee, T. Mapping the Wildland-Urban Interface in California using a vector-based edge approach. **2022**
Under review at ERL

Kumar, M., Kosovic, B., Randerson, J., and Banerjee, T. Simulating a Southern California wildfire event using the Weather Research and Forecasting model. **2022**
Under review

Kumar, M., Jonko, A., Mirocha, J., Lassman, W., Kosovic, B., and Banerjee, T. Impact of momentum perturbation on convective boundary layer turbulence. **2022**
Under review

Kumar, M., Frediani, M., Juliano, T., Kosovic, B., Randerson, J., and Banerjee, T. The Role of Fire-induced Turbulence on Ember Transport. **2022**
Under preparation

SOFTWARE

Models

QUIC-Fire, Weather Research and Forecasting (WRF), WRF-LES, WRF-FIRE, Regional Ocean Modeling System (ROMS), Fire Dynamics Simulator (FDS)

Software

MS Office, NOAA HYSPLIT, AutoCAD, ESRI ArcGIS & ArcGIS PRO, QGIS, Jupyter Notebook

Languages

GrADS, MATLAB, LaTeX, Python, Fortran 95, R (basic)

ABSTRACT OF THE DISSERTATION

Mapping and Modeling of Fires in the Wildland-Urban Interface

By

Mukesh Kumar

Doctor of Philosophy in Civil and Environmental Engineering

University of California, Irvine, 2022

Assistant Professor Tirtha Banerjee, Chair

The severity and frequency of wildfires have risen dramatically in recent years, drawing attention to the wildland-urban interface (WUI), the region where human-made structures meet wildland vegetation. The focus of my doctoral research is to obtain an improved understanding of wildfires at the WUI through mapping and modeling approaches. First, I revisit the existing definitions of WUI for California and then propose a novel, finer-resolution WUI-mapping method that is based on the linear intersection of flammable vegetation and building footprints. From this mapping exercise, it appears that the dominant mode of fire-induced damage in the WUI is from firebrands, which can travel long distances away from the fire-front. Next, I proceed to test the capability of a non-hydrostatic, mesoscale weather research and forecasting (WRF) model to capture the meteorological parameters of different geographical regions in Southern California, during the 2007 Witch Fire. Hereafter, I use a large eddy simulation (LES) version of WRF to analyze the mechanisms of turbulence generation using momentum perturbation, since turbulence plays a vital role in ember transport during fires that are driven by heavy wind events, such as the Santa Ana winds. Finally, I discuss the potential of using a coupled fire-atmosphere model, called WRF-Fire, to investigate ember transport over complex terrain as a major driver of wildfires in the WUI. My research advances the science of fire prediction, with potential benefits for fire and ecosystem managers and communities living within or near the WUI.

Chapter 1

Introduction

1.1 Background

The goal of this Ph.D. project is to improve the existing understanding of fires in the WUI through modeling and mapping approaches. In chapter 1, I first briefly discuss key background information that provides context and theory for the proposed research, separated into the following topics: (1) fires in the WUI (section 1.2); (2) ember transport and spot fires (section 1.3); and (3) complex terrain (section 1.4). The objectives and results of the Ph.D. research are presented in five chapters, from chapter 2 to chapter 6, followed by the dissertation conclusions in chapter 7.

1.2 Fires in the WUI

The intensity and frequency of wildland fires over the contiguous United States (CONUS) have been increasing remarkably and caused much economic damages in the last two decades [Massada et al., 2009, Bowman et al., 2009, Radeloff et al., 2018]. The damages due to these extreme events are mainly located at Wildland-Urban Interfaces (WUI), which are regions where houses and man-made structures meet or overlap the wildland vegetation as defined in the Federal Register (US Department of Interior (USDI) and US Department of Agriculture (USDA)), 2001. The current definition of WUI includes the concepts of ‘Intermix’ and ‘Interface’. ‘Intermix’ is the area where human developments and wildland vegetation overlap, while ‘Interface’ is that region which is nearby to a densely vegetated wildland. This definition of WUI is in concurrence with the National Fire Plan (NFP) which was based on the WUI fire risk report [Teie, 1999]. This framework consists of three main parameters: (1) housing density threshold of 6.18 houses per sq. km (1 house per 40 acres); (2) vegetation type and (3) proximity of 1.5 miles (2.4 km) from dense vegetation (over an area of 5 sq. km with more than 75% vegetation cover). Out of these 3 parameters, the housing density threshold is the most sensitive parameter in the existing definition of WUI as studied by Stewart et al. [2007], Radeloff et al. [2005b]. Earlier definitions of WUI were centered on the metric of population density [Glickman and Babbitt, 2001, Liu et al., 2003]. However, it was later recognized by Liu et al. [2003] that housing density was a more appropriate metric compared to population density for mapping WUI. Therefore, the WUI criteria had been modified and the housing density threshold was included in WUI definition in the Federal Register (2001) for WUI (for both intermix & interface).

Wildland fires destroy thousands of buildings in the US annually. In recent years, CA wildfires have burned the highest number of acres of all states in the US, according to the National Interagency Fire Center (NIFC) report (2018). This wildfire season gained the title of ’giga fire’ in the year 2020 and burned more than a million acres of land compared to previous years during which the burned area had been recorded as a few hundred thousand acres (’mega fire’). In 2020, 4,177,855 acres of California burned with a total of 9,639 wildfire incidents that destroyed 10,488 buildings and caused 33 fatalities according to the 2020 CAL FIRE summary report. In the same year, out of nearly 17,700 total damaged structures in the US, 11,253 buildings were destroyed and affected by wildfires in CA which made it one of the most devastating wildfire seasons on record. From 2010 to 2020, a total of 52,955 buildings were destroyed in CA on its own (Headwater economics, November 2020: https://headwaterseconomics.org/natural hazards/structures-destroyed-by-wildfire/). The biodiversity of nature was affected with the total extinction of a few species of flora and fauna in the local and regional forested lands. Whenever homes are constructed near flammable vegetation, it poses two types of major issues: first, the risk of human sparked fires increases, and second, it also escalates the risk of damage caused by wildfires [Radeloff et al., 2018]. Recent studies suggest that most of the CA wildfires destroyed houses in the WUI but occurred outside the existing WUI regions [Kumar et al., 2020, Kramer et al., 2018].

1.3 Ember transport and spot fires

There is a higher risk of structural damage due to wildfires in the WUI. However, it is not clear whether the structural damage reported in the literature has been a result of the wildfires penetrating the WUI. If it is found that most wildfires burn inside the WUI, it would mean significant investments in fuel treatments are required within and nearby the WUI area. If most of the wildfires are found to burn nearby but not within the WUI area itself, it would mean that ember/firebrand ignitions play a significant role in property damage in the WUI and therefore strong investments in home hardening in terms of more fire-resistant materials and other fireproofing techniques are also equally important. Moreover, wildfires burning near the WUI areas would also complicate firefighter access and evacuation efforts thereby complicating suppression and overall firefighting strategy. Some modeling studies such as by Koo et al. [2012] investigated firebrand transport during a wildfire event using a coupled atmosphere/wildfire behavior model i.e., HIGRAD/FIRETEC. Firebrand spot ignition is one of the main techniques of fire spreading. The effects of topography on these winds have a major impact on firebrand transport as firebrands are being carried and moved by the fire-induced winds. The shape of the firebrand also impacts the distance traveled by it. For example, disc shaped firebrands travel farther than cylindrical firebrands because they are more aerodynamically favorable [Koo et al., 2012]. Similarly, fire size and types also impact firebrand transport - in the case of canopy fires it travels larger distances than in the case of surface fires [Koo et al., 2010]. Fernandez-Pello [2017] studied wildfire spot ignition by firebrands and found that topography and weather conditions play an important role in ember transport and therefore, wildfire spread models can be computed as a function of these variables.

1.4 Complex terrain

In states like California (and many of the western states in the US), a significant area of the WUI might be situated on complex topography. If the presence of the WUI is generally perceived to be associated with heightened fire risk, it is worth knowing how much of the WUI is on complex topography. This is important from a planning and policy perspective, given that firefighting, rescue, and evacuation operations are significantly complicated due to the presence of complex topography. The presence of topography adds to uncertainties in wildfire behavior (Linn et al., 2007) and leads to the creation of micro-meteorological conditions which changes the wind patterns and turbulence levels in the atmospheric boundary layer over the WUI. This orographic effect might lead to differences in how far firebrands can travel and where they land compared to flat terrain. Therefore, relying on a buffer zone of 1.5 miles from a densely vegetated area as a general criterion is worth analyzing further. Graham et al. (2012) showed very interesting results that embers are not the only cause of ignition away from the ignition points, and low intensity surface fires can also lead to significant damages.

Topography is one of the most influential factors in the fire spread rate. Wildland fires travel much faster uphill than downhill, and the spread and intensity of a fire on an uphill slope are further increased by wind, due the enhanced efficiency of convective preheating of fuel elements on an upslope, downwind of the flame front. Wildfires are easier to control over a flat surface and burn less intensely than over a moderate or steep slope. Moreover, complex topography influences wind flow and local turbulence patterns, thereby altering the uplift and dispersion of firebrands. It has been already established that firebrand exposure is extremely important while considering structural and property damage in the WUI. To better understand the perception of fire risk in the WUI, I analyzed the locations of the existing WUI in California, which is associated with a very complex topography. Firebrands can statistically travel more than 1.5 miles (2.4 km) distance as assumed in the USFS WUI mapping method; and the meteorological factors like wind speed are more favorable for higher rate of fire spread and firefighting is difficult due to complex terrain.

Chapter 2

Examining the existing definitions of wildland-urban interface for California

2.1 Introduction

The intensity and frequency of wildland fires over the contiguous United States (CONUS) have been increasing remarkably and caused much economic damages in the last two decades [Massada et al., 2009, Bowman et al., 2009, Radeloff et al., 2018]. The damages due to these extreme events are mainly located at Wildland-Urban Interfaces (WUI), which are regions where houses and man-made structures meet or overlap the wildland vegetation as defined in the Federal Register (US Department of Interior (USDI) and US Department of Agriculture (USDA)), 2001. The current definition of WUI includes the concepts of 'Intermix' and 'Interface'. 'Intermix' is the area where human developments and wildland vegetation overlap, while 'Interface' is that region which is nearby to a densely vegetated wildland. This definition of WUI is in concurrence with the National Fire Plan (NFP) which was based on the WUI fire risk report [Teie, 1999]. This framework consists of three main parameters: (1) housing density threshold of 6.18 houses per km^2 (1 house per 16.2 hectares or 40 acres); (2) vegetation type and (3) proximity of 2.4 km (1.5 miles) from dense vegetation (over an area of 5 km^2 with more than 75 % vegetation cover). Out of these 3 parameters, the housing density threshold is the most sensitive parameter in the existing definition of WUI as studied by Stewart et al. [2007] and Radeloff et al. [2005b]. Earlier definitions of WUI were centered on the metric of population density [Glickman and Babbitt, 2001]. However, it was later recognized by Liu et al. [2003] that housing density was a more appropriate metric compared to population density for mapping WUI. Therefore, the WUI criteria had been modified and the housing density threshold was included in WUI definition in the Federal Register (2001) for WUI (for both intermix & interface). Several earlier studies had been devoted to analyze the expansion of WUI areas across North America over the past several decades and the drivers behind it. A few studies [Radeloff et al., 2001, Johnson et al., 2005] identified the cultural aspect of human inclination to live near the natural amenities provided by forested lands, mountainous regions and seashores. Housing growth was widespread in rural and suburban areas in the United States during the mid-1900s. Its continued trend contributed to a 41 % growth in the construction of new homes within the WUI from 1990 to 2010 [Radeloff et al., 2005a, 2018]. Housing density has grown faster than population density in recent decades and the same trend is reflected in the context of WUI [Martinuzzi et al., 2015]. Also, more than 50 % houses present in the WUI were damaged in California due to large wildfires [Caggiano et al., 2020]. Thus, there is a higher risk of structural damage due to wildfires in the WUI. The existence of the WUI terminology was already in place before the wildland fire policies had taken it into consideration in the 2000s but it was not as widespread in the wildfire literature. It had only become a widely used term in the recent years due to the increasing/maximum damages in this land-use type due to wildfires [Martinuzzi et al., 2015, Radeloff et al., 2018]. Vaux [1982] had discussed about future risks due to the emerging interface areas and called WUI as the “hotseat of forestry”. Also, Bradley [1984] had focused on this new interface in their famous book on resource management, but none of them had related WUI with wildfires. Finally, Davis et al. [1990] connected the idea of WUI with the wildland fires. Currently, the term WUI is used mostly in the context of wildfires as the maximum damages due to wildfires occur in the WUI [Kramer et al., 2019]. Stewart et al. [2009] demonstrated that WUI definitions vary depending on purpose and context by comparing the two definitions that are based on the NFP and Healthy Forest Restoration Act (HFRA) with the study location over the Los Angeles area. The NFP definition had focused on the number of structures (housing-centric definition) nearby the wildland vegetation within a buffer of 2.4 km (1.5 miles) for the interfaces and therefore it was more helpful to the policymakers in determining the risk prone housing regions and taking possible steps in reducing the growth rate of the homes in these locations. According to the California Fire Alliance (2001), on an average a firebrand can travel up to 2.4 km (1.5 miles) from a wildland fire-front and thus the buffer distance for the interface is the same. The houses within this buffer zone would be at higher risk of burning during wildfire events. On the other hand, the HFRA definition of WUI was more helpful to the land managers and has the aim of finding the sources of fuels for future wildfires within the vicinity of the houses/structures and therefore can be considered a fuel-centric definition. The HFRA defined interfaces that are present within a buffer of 805 m (0.5 miles) from the houses and called it as a mitigation zone for the Community Wildfire Protection Plans [Wilmer and Aplet, 2005]. Apart from these many existing definitions of WUI, a new WUI mapping called Fire and Resource Assessment Program (FRAP) was developed by CAL FIRE, the agency to serve and safeguard the people and protect the property and resources of California. The FRAP modified the definition of WUI (intermix and interface) in terms of the housing density thresholds in concurrence with the NFP policy and mapped it for California for 2010. Platt [2010] compared five different WUI models, including FRAP, based on the choice of wildland vegetation, housing density with and without public lands, buffer distance from wildland vegetation or human settlements and its magnitude as well as the point and zonal based approach of defining housing density. It was found that the WUI mapping methods were characterized by different degrees of accuracy, which vary with their utilization and extent of study [Stewart et al., 2009]. For example, in the point-based approach of defining housing density, structures were represented as points and mapped from parcel centroid excluding remote buildings which were farther than 569 m (0.35 miles) from another building [Platt, 2010]. Many other WUI definitions [Pereira et al., 2018] were based on different data sources such as remote sensing, census block or their combination. Furthermore, there were different WUI mapping methodologies based on purpose, for example - housing centric, fuel centric, etc. as mentioned in Platt [2010]. However, none of the studies analyzed and compared the predominant definitions of WUI with the context of wildfire occurrence. Syphard et al. [2019] demonstrated the impact of climate change and urbanization on loss of buildings in California. They quantified that building losses are high in low density buildings and with housing development it might further increase. Kramer et al. [2019] also highlighted that more destructive wildfires threatened and damaged more buildings in the interface WUI and fewer in rural regions. Also, the rate of building destruction is higher in the urban areas where there is higher population density than the rural areas. They reported that in the last three decades, 50 % of buildings destroyed in California were at WUI interfaces and 32 % of buildings destroyed were in WUI intermix areas [Kramer et al., 2019]. On an annual basis in the WUI (1999–2014), an average of 2.5 million homes (2.2–2.8 million, 95 % confidence interval) were threatened by human-started wildfires (within the perimeter and up to 1 km away) as reported in a recent study by Mietkiewicz et al. [2020]. Therefore, increasing trends of the expansion of WUI areas would mean that more lives and properties are at risk from wildfire induced damage. Wildfire events have been increasing within the WUI in the CONUS [Platt, 2010, Martinuzzi et al., 2015]. In California, the frequency of even smaller fires ($<$ 202.3 hectares or 500 acres) caused by human activities have increased from 2010 to 2019 [Li and Banerjee, 2021]. The wildfire ignitions are also directly proportional to the WUI expansion [Syphard et al., 2019]. The proportion of buildings destroyed within the WUI and non-WUI zones were 69 % and 31 % respectively in the US [Kramer et al., 2018]. However, on overlapping the area of fire perimeters with the building footprints from 2000 to 2013, only 1.1 % (1,398 km^2) of the buildings were destroyed within the WUI, while this number was 34 % (41,262 km^2 within the non-WUI regions for the US (Kramer et al., 2018). Caggiano et al. [2020] highlighted that more than 85 % building losses occurred in the WUI due to wildfires from 2010 to 2018. However, out of total 2,777 fires, only 70 were used in this study [Caggiano et al., 2020] which damaged more than 50 buildings and were called WUI disasters. Fighting fire is difficult in the WUI due to the unique combination of wildland and structural fuels as firefighters are usually trained in either wildland fires or structural fires but not both [Stewart et al., 2003]. Moreover, wildfire exposure threatens or undermines the community and ecosystem services provided by WUI areas, such as enjoying recreational activities, timber production, habitat conservation for several species, watershed protection and even visual aspects such as scenic beauty [Stewart et al., 2003]. Thereby it is important to understand the modes of fire exposure at the WUI which would impact both aspects of fire prevention, suppression, and fire impacts on the WUI. Recent wildland fire policy has targeted fire prevention, evacuation planning, fuel treatment and home hardening against ignition in WUI areas [Radeloff et al., 2018, 2005b, Cohen, 2000, Haight et al., 2004]. Therefore, it is important to understand the occurrence of wildfires relative to the WUI areas, as well the relative importance of WUI related factors that influence wildfire occurrence and size. Moreover, in states like California (and many of the western states in the US), a significant area of the WUI might be situated on complex topography. If the presence of the WUI is generally perceived to be associated with heightened fire risk, it is worth knowing how much of the WUI is on complex topography. This is important from a planning and policy perspective, given that firefighting, rescue, and evacuation operations are significantly complicated due to the presence of complex topography. The presence of topography adds to uncertainties in wildfire behavior [Linn et al., 2007] and leads to the creation of micro-meteorological conditions which changes the wind patterns and turbulence levels in the atmospheric boundary layer over the WUI. This orographic effect might lead to differences in how far firebrands can travel and where they land compared to flat terrain. Therefore, relying on a buffer zone of 2.4 km (1.5 miles) from a densely vegetated area as a general criterion is worth analyzing further. Graham et al. [2012] showed very interesting results that embers are not the only cause of ignition away from the ignition points, and low intensity surface fires can also lead to significant damages. However, there is always a higher risk of ignition within the fire perimeter than outside it because of the close vicinity to the flame front. Overlapping past wildfire events with WUI along with complex topography would help us understand where wildfires occur relative to the WUI areas; thereby providing a quantified measure of the perceived risk associated with the wildfire-WUI connection. In this work, our objectives are the following: (1) evaluate the two predominant definitions of WUI against the actual occurrences of wildfires in CA; (2) examine the role of the parameters used to define the WUI, such as the buffer distance, in determining the relationship between wildfire occurrence and WUI; (3) evaluate if the presence of complex terrain is an important factor in the WUI, as complex topography might mean more complex rescue, firefighting, and evacuation operations, and presence of complex terrain means further uncertainty in parameters such as buffer distance since they are based on ember transport characteristics; (4) evaluate the relative importance of parameters that define the WUI in wildfire occurrence within or near the WUI. To satisfy these objectives, we will attempt to answer the following research questions: (1) Where are the wildfires (a) igniting and (b) burning relative to the WUI? (2) what is the impact of buffer distance in the percentage overlap of fire perimeters and fire ignition points in the WUI? (3) where is the WUI located in terms of elevation and the complexity of the terrain? and (4) what are the relative importance of WUI parameters that impact wildfire occurrence and size within or near the WUI? Results from this paper will be helpful for the wildfire management and would benefit the policymakers and land managers at the state and local level to focus on the factors that determine the high-risk prone areas for future wildfires.

2.2 Materials and Methods

2.2.1 WUI data

We used two existing WUI data sources for 2010 that were obtained from USFS [Martinuzzi et al., 2015] and CAL FIRE (FRAP, 2015). We designate them WUI-A and WUI-B respectively for our study. We plotted the spatial map of WUIs over CA to analyze the variation in the location of the WUI which includes both WUI intermix and WUI Interface. WUI-A used the definition of Federal Register (2001) following the NFP policy, while CAL FIRE modified the housing threshold and added the wildfire influence zone & moderate or higher levels of fire hazard severity zones.

2.2.2 Wildfire data

Since we wanted to overlap wildfires datasets with WUI which was from 2010; therefore, we can not choose those wildfires that occurred before 2010 to overlap with 2010 WUI data. Perimeters of wildfire events were obtained from the Monitoring Trends in Burn Severity (MTBS) dataset (MTBS, 2020) that includes all fires (2010-2017) in CA having an area greater than 1,000 ac (400 ha). We designate these wildfires as large wildfires Butry et al. [2008]. Landsat imagery of pre-fire and post-fire images at a resolution of 30 were used by Eidenshink et al. [2007] to detect MTBS fire perimeters, which reflect the boundary of the region burned by a wildfire event. The wildfire data obtained from MTBS for CA has a total area of 19,517.675 km^2 of wildfires from 2010 to 2017. It also comprises a total 329 fire ignition points in the state from 2010 to 2017. Also, the fire ignition points data are consistent with the wildfire perimeter datasets. Ignition points of the fires were obtained from MTBS Fire Occurrence Points [Scott et al., 2016] for 8 years i.e., from 2010 to 2017 (MTBS, 2020). The National Wildfire Coordinating Group classified wildfires into seven classes, ranging from A to G, based on their size. In this study, we defined classes A through E as small fires, or wildfires with an extent of less than 404.7 hectares or 1,000 acres. The thresholds for large and small wildfires were determined with reference to the research of Butry (2008). Small wildfire (less than 1000 ac or 400 ha) points were obtained from the fifth edition of spatial wildfire occurrence data originated by Short [2017]. It collected wildfires from 0.001 acre across the United States from 1992 to 2018. Wildfires in California that are smaller than 404.7 hectares or 1,000 acres were extracted from this database and defined as small wildfires in this study.

2.2.3 County and topography data

County boundaries for the state of California have been taken from the CA government geographic boundary (County Boundary, 2019). Elevation data were obtained from Google Earth Engine (GEE) which has used USGS DEM elevation maps available at 1/30 arc-second (GEE, 2012). For our study we resampled the obtained data from GEE at a spatial resolution of 10 m to 30 m using the ArcMap (10.7.1) tool in ArcGIS (ArcGIS, 2020). To calculate the overlap of 2010 WUI and different elevation ranges, we have used the ArcMap 10.7.1 (ArcGIS, 2020) spatial analyst tool, selected the extraction tool, and then chose extraction by mask. First, we reclassified the elevation data into nine separate ranges: the first eight ranges were from 0 to 800 m in 100-meter intervals, while the last range was from 800 to 4,410 m. Then we merged both WUI-A and WUI-B with these ranges to calculate the number of counts falling in each elevation range. Moreover, we have made sure that WUI and Elevation raster layers have the same properties. WUI-A data available in vector form was converted to raster using ArcPy (ArcGIS with python) keeping the same 30 m spatial resolution as the elevation data. We have then divided the number of counts in each elevation range to the total count to find the percentage WUI over different elevation ranges. We performed similar methods for calculating the percentage overlap of WUI and elevation for CA with both WUI-A &

WUI-B for the year 2010. To see the surface roughness for the state which has numerous mountains and complex topography, we have calculated the rugosity of this region, which is defined as the ratio of actual surface area to the planar surface area of a region. Higher value of rugosity shows presence of more complex terrain in that region and vice-versa. We have used the Digital Elevation Map (DEM) surface tool developed by Jenness [2004] in the ArcMap to calculate the rugosity (surface ratio) for the state. The DEM surface tool has one advantage over other existing surface ratio calculation tools. Here, we do not need to do adjustment in Z-units with respect to (w.r.t.) X/Y-units while dealing with data in geographic coordinate systems. Otherwise, we need to get Z-units corrected first to calculate the surface ratio. The WUI (both WUI-A & WUI-B) have been overlapped with rugosity following the same methodology as discussed above for elevation to find its variation with surface roughness for the state.

2.2.4 Analysis methods

The overlap of wildfire perimeters and WUI has been processed in ArcGIS with varying buffer distances using the buffer tool in geoprocessing, followed by the dissolve tool to merge each buffer into one feature. Five different buffer radii from 1 km to 5 km have been selected around wildfire perimeters and WUI (both WUI-A & WUI-B). WUI-A data were available in polygon (vector), so WUI-B raster data were converted to polygon using conversion tools in ArcMAP. Finally, we intersected fire perimeters (WUI buffers) and WUI (fire perimeter buffers) to obtain the overlapped area. For the calculation of fire ignition points within WUI buffers, we have used “select by location” using the selection method as “select from layer”, choosing target layer as fire ignition points and source layer as WUI buffer layers (WUI-A & WUI-B).

2.2.5 Statistical models

To model the relationship among wildfire presence, wildfire area, distance from wildfires to WUIs, housing density and vegetation density, the logistic regression model (LoR) was applied. The dependent variables in the model are the probability of wildfire occurrence (including both large and small wildfires), and large wildfire areas, separately. It is noted again that for wildfire occurrence, data from both large and small wildfires are available as discussed above, while for burned area, only the data for large wildfires (greater than 1000 ac or 400 ha) are available and considered. The ignition points of wildfires extracted from MTBS were assigned a value of 1. Then, as many random points as wildfire points were generated within the boundary of California and out of the large wildfire perimeters. These points were assigned a value of 0, which means there were no large wildfires from 2010 to 2017. The independent variables in this model included distance from wildfires to WUI-A and WUI-B, which was calculated using the "near" function in ArcGIS Pro; housing density, calculated using 2010 Census data; vegetation density, which was calculated using fuel vegetation cover (FVC) from LANDFIRE; and topographic information including elevation, aspect, slope and rugosity. The area under the Receiver-Operating Characteristic curve (ROC) of LoR model is the probability of large wildfire occurrence with a range of 0 to 1. The probability higher than 0.5 represents a strong correlation. When there are more than one independent variable in the model, the estimated coefficients represent the change in the log odds of large wildfire occurrence per unit change in the independent variables. The results table also included the standard error, z statistics and associated p-values in model fitting.

2.3 Results and Discussion

2.3.1 Difference between two types of WUI mappings for California

The definition of WUI varies with different mapping methods and the changes in the major parameters like housing density threshold, buffer distance, etc. Figure 2.1 shows the differences in the WUI distribution for California as mapped by USFS [Martinuzzi et al., 2015] and CAL FIRE (FRAP, 2015) for the year 2010. The housing density threshold used by these two mappings are different and is 6.18 houses per km^2 (1 house per 16.187 hectares 40 acres) in the former while it is $>$ 1 house per 0.08 km^2 ($>$ 1 house per 8 hectares or 19.8 acres) in the latter. CAL FIRE also includes other parameters for the WUI definition and requires moderate to very high fire hazard severity zones (The Fire Hazard Severity Zones (FHSZ) were defined by CAL FIRE to evaluate "the severity of fire hazard that is expected to prevail there" based on various factors such as fuel, slope and fire weather). In addition, their definition warrants spatially contiguous groups of 30 m cells having an area larger than 0.04 km^2 (4 hectares) for the WUI Interface and larger than 0.1 km^2 (10 hectares) for the WUI intermix. Although the buffer distance of 2.4 km (1.5 miles) is the same in both the cases, for WUI-A, it is the distance from a densely vegetated area and is called WUI-intermix. Whereas, for WUI-B, it is the distance up to which flammable vegetation lie from WUI-intermix or WUI-Interface and is known as wildfire influence zone. The WUI-A consists of more area (27,025.683 km^2) than WUI-B (9,606.273 km^2) as shown in Figure 2.1 because of the difference in the housing thresholds and additional vegetation classification parameters used for WUI-B. The overlapping results between WUIs and wildfires are similar for both types of WUIs (WUI-A and WUI-B), where intermixes have higher percentage overlap than interfaces (Table 2.1).

Site	WA (km^2)	WBA (km^2)	OA (km^2)	POWBA	PWI	POA
a) WUI-A		19,517.68				
Interface	8046.64		49.39	0.25	0.30 (1/329)	0.61
Intermix	18, 979.04		747.11	3.83	3.34(11/329)	3.94
Total	27,025.68		796.50	4.08	3.65(12/329)	2.95
b) WUI-B		19,517.68				
Interface	4,232.85		24.43	0.13	1.22 (4/329)	0.58
Intermix	5,373.43		129.17	0.66	0 (0/329)	2.40
Without	9,606.27		153.60	0.79	1.22(4/329)	1.60

Table 2.1: The overlap between wildfire burned areas and fire ignition points with WUI-A and WUI-B. Here, POA-percentage of overlapped area; PWI-percentage of wildfires ignited; POWBA- percent overlap in wildfire burned area; OA-overlapping area; WBA-wildfire burned area; WA-WUI area.

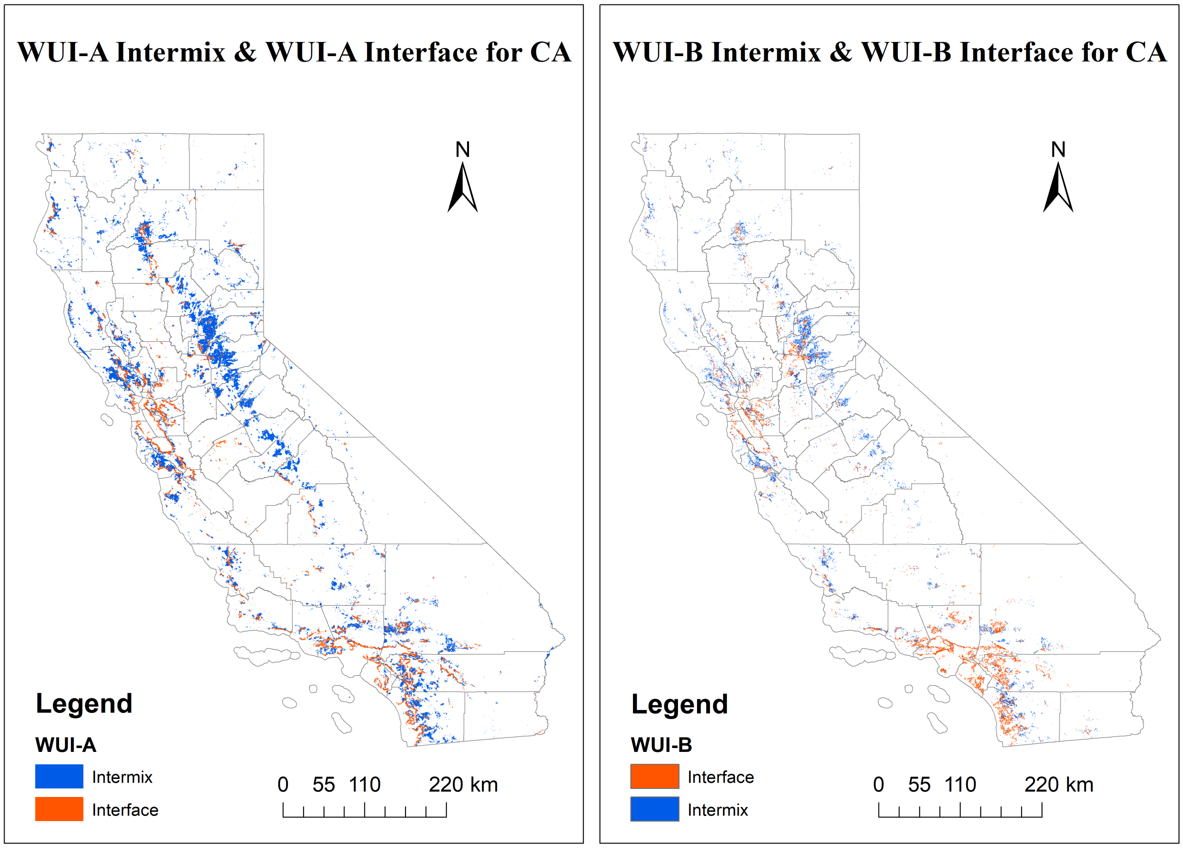

Figure 2.1: The figure on the left and right panels shows the spatial plots of WUI in 2010 over California using WUI data from USFS (Martinuzzi et al., 2015) and CAL FIRE (FRAP, 2015) and we designate them as WUI-A and WUI-B respectively for our study. "Intermix" represents the area where human developments and wildland vegetation overlap, while "Interface" is that region which is nearby to a densely vegetated wildland.

2.3.2 Overlap of WUI with wildfire burned areas

The wildfire data used in this study obtained from MTBS report a total burned area of 19,517.675 km^2 for CA. These historical wildfire datasets are from 2010 to 2017 and include all fire events with burned areas greater than 1,000 ac (400 ha or 4 km^2). Table 2.1 shows total area of WUI-A in CA to be 27,025.683 km^2 with both interface (8,046.643 km^2) and intermix (18,979.040 km^2) types of WUI-A. WUI-A interface has less (49.387 km^2) overlap between wildfire burned areas and WUI-A than WUI-A intermix (747.113 km^2). The percentage of overlap in wildfire burned areas in intermix WUI-A (3.83 %) is higher than interface WUI-A (0.25 %), making a total of almost 4.1 % of wildfire areas that burned within WUI-A. Note that these (aforementioned) percentages are computed as compared to the total wildfire burned areas (i.e., overlap area/wildfire burned area). The percentage of overlap between WUI areas and wildfire burned areas can also be computed relative to the area of WUI itself (overlap area/WUI area shown in the rightmost column in Table 2.1). From this perspective, the percentage overlap in WUI-A intermix is 3.94 %, i.e., more than six-times the overlap in WUI-A interface (0.61 %). Therefore, only 2.947 % of WUI-A areas have been directly burned by wildfires during this study period. Table 2.1 also shows the total area of WUI-B in CA to be 9,606.273 km^2 with a lower proportion of WUI-B interface (4,232.847 km^2) than WUI-B intermix (5,373.426 km^2). Clearly, the percentage of overlap between WUI-B interface and wildfire perimeters relative to wildfire burned areas is lower (0.125 %) than intermix WUI-B (0.662 %) for the state. Hence, only 0.79 % of wildfire burned areas are contained within WUI-B in CA. When the overlapped area is expressed relative to WUI-B areas, there is a higher percentage overlap in the WUI-B intermixes (2.4 %) compared to WUI-B interfaces (0.58 %). Therefore, only 1.6 % of WUI-B in CA has burned directly during the study period. Moreover, the intermixes have more wildfire burned area than interfaces for both types of WUIs. The percentage overlap of wildfire burned areas with respect to (w.r.t) WUI areas is less for WUI-B (1.6 %) as compared to WUI-A (2.95 %)

because of the exclusion of the influence zone from WUI-B definition (Figure 2.1).

2.3.3 Analysis of buffer distance from wildfire perimeters

From the discussion above, it is clear that a very small percentage of wildfires burn within the WUI areas in CA. This invokes the question of whether these wildfires burn in the vicinity of the WUI areas. To investigate the occurrence of wildland fires outside and away from the existing WUIs, we performed a buffer analysis, varying the distance from 1 km to 5 km from wildfire burned areas (Table A.1 in the supplementary file) and recalculating the previous statistics reported in Table 2.1. Appendix A: Table A.1 shows an increase in the percentage overlap of wildfire burned areas and WUI-A with buffer distance relative to the wildfire buffer area (fifth column) and relative to the WUI area (sixth column). When the buffer radius increased from 0 km to 5 km around the wildfire burned areas, the overlapped region increased by more than 9 times (from 796.5 km to 7,580.4 km). The percentage of this overlapped region in the WUI-A increased from almost 3 % (for no buffer) to 28 % (for 5 km buffer distance) respectively. On the other hand, we observed a small change of only 4 % was in the percentage overlap in wildfire buffers by increasing buffer distance from 0 km to 5 km. This is expected because the wildfire buffer area relative to which the percentages are calculated also increases with the buffer distance. Similarly, the percentage overlap relative to WUI-B (sixth column) increased to 25.5 % (Appendix A: Table A.1) with 5 km buffer distance from wildfire burned areas. On the other hand, the increase in the percentage of overlap relative to the wildfire buffers is from 0.8 % to 2.5 % with no buffer to 5 km buffer distance, respectively. However, the effects of WUI types on the percentage overlap is not different between WUI-A & WUI-B; increasing the buffer distance from wildfires increased percentage overlap in both the WUIs (Appendix A: Table A.1).

Figure 2.2 shows the spatial distribution of overlap between varying buffer distances from

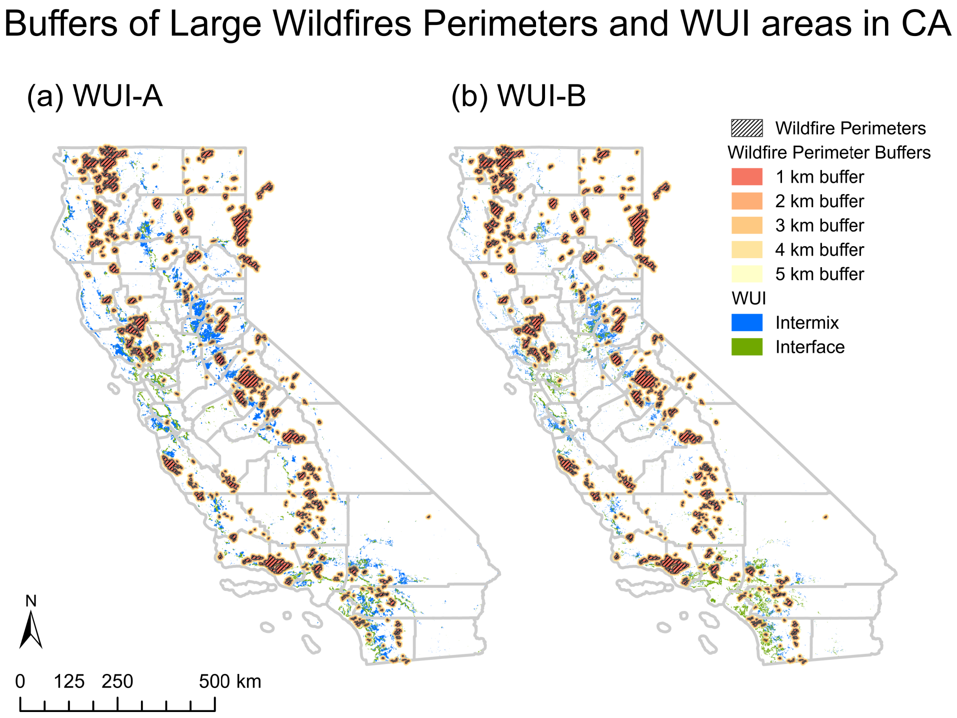

Figure 2.2: The figure on the left panel shows a spatial plot of buffers of fire perimeters (large fires only, having an area greater than 1,000 ac) and WUI-A for CA; similarly, the figure on the right panel represents buffers of large wildfires and WUI-B in CA. Legends in these spatial plots show types of WUI (intermix and interface) and the varying wildfire perimeter buffer distances.

Site	**Parameters**	**Large Wildfires**				**Small Wildfires**			
WUI-A		Estimate	Std. Error	z value	Pr($>\|z\|$)	Estimate	Std. Error	z value	Pr($>\|z\|$)
	(Intercept)	-1.00000	0.17480	-5.72	0.00000	0.97320	0.01064	91.46	$< 2e^{-16}$
	D2WUIA	-0.00003	0.00001	-3.11	0.00183	-0.13680	0.00121	-112.82	$< 2e^{-16}$
	RhoHou	-0.00032	0.00013	-2.56	0.01021	0.00001	0.00000	40.02	$< 2e^{-16}$
	FVC	0.03545	0.00370	9.59	$< 2e^{-16}$	-0.01663	0.00029	-57.53	$< 2e^{-16}$
WUI-B		Estimate	Std. Error	z value	Pr($>\|z\|$)	Estimate	Std. Error	z value	Pr($>\|z\|$)
	(Intercept)	-1.05100	0.17550	-5.99	0.00000	1.17000	0.01131	103.46	$< 2e^{-16}$
	D2WUIA	-0.00002	0.00001	-2.62	0.00862	-0.10100	0.00087	-116.54	$< 2e^{-16}$
	RhoHou	-0.00032	0.00013	-2.54	0.01102	0.00001	0.00000	29.32	$< 2e^{-16}$
	FVC	0.03621	0.00368	9.84	$< 2e^{-16}$	-0.02119	0.00029	-73.62	$< 2e^{-16}$

Table 2.2: Results of logistic regression model for parameters in WUI definition and wildfire occurrence probability. Here, * FireIdx - Fire Index, presence/absence of large wildfires; D2WUIA/D2WUIB - Distance to WUI-A/WUI-B, the distance from fire and random non-fire points to WUI areas; RhoHou - Housing density, the number of houses per km^2 in each Census blocks; FVC - Fuel vegetation cover, the percentage cover of vegetation.

the existing wildfire perimeters and two types of WUI used in this study (WUI-A and WUI-B). Wildfire perimeters are nearer to WUI-A as seen in Figure 2.2 on the left panel and thus will result in higher percentage overlap between wildfire burned area and WUI-A (also shown quantitatively in Appendix A: Table A.1). Also note that the total area of WUI-B: 9,606.273 km^2 is less than that of WUI-A: 27,025.683 km^2. Figure 2.3 shows that the percentage overlap with increasing buffer distance with respect to the WUI area in the red line and with respect to the wildfire buffer area in black line. Both increasing trends are found to regress well with a linear trend. These linear trends are found for both WUI types. However, the slope in case of WUI-B is higher as compared to WUI-A, and thus, there is a higher rate of increase in the percentage overlap. On the other hand, the percentage overlap with respect to wildfire buffer areas does not increase in the similar manner for both the cases with varying buffer distances. However, the rate of increase in percentage overlap in wildfire buffers is higher for WUI-B (from 0.8 % to 2.6 %) as compared to WUI-A (from 4 % to almost 8 %).

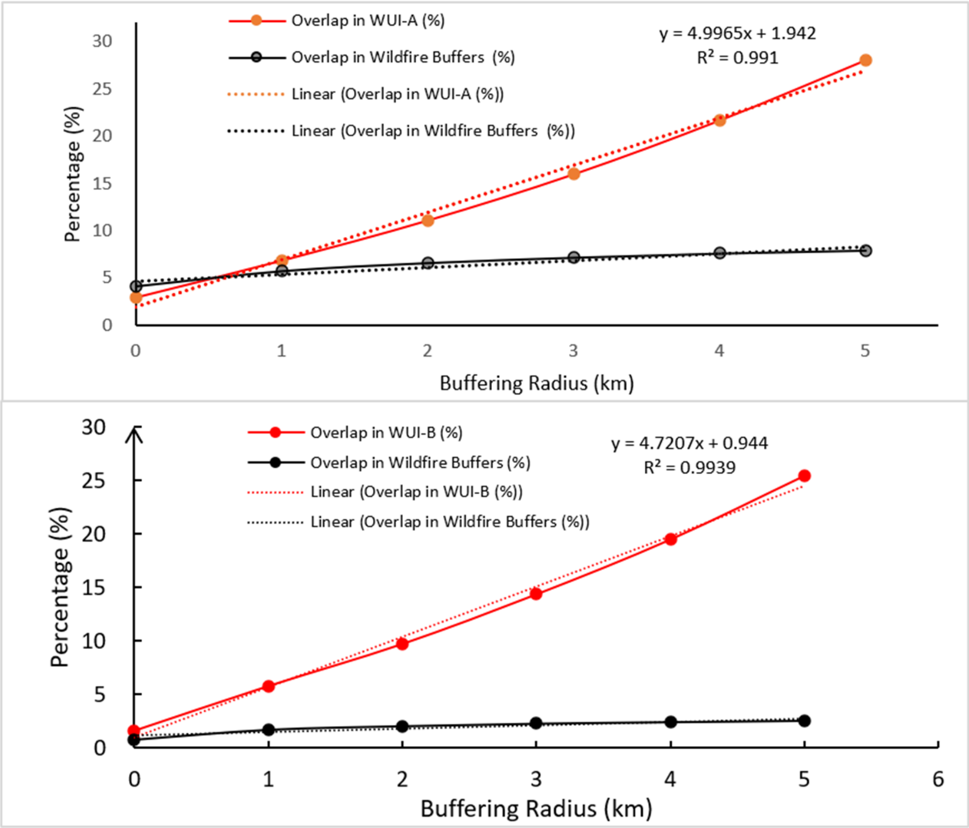

Figure 2.3: The figure on the top panel shows percentage overlap between wildfire burned area with WUI-A with respect to WUI-A area (solid red line) and percentage overlap with respect to wildfire buffer area (solid black line). The figure in the bottom panel shows the same for WUI-B. Here, Y-axis represents the percentage overlap, while X-axis represents the buffer distance (in km). The dotted line indicates curve fitting (linear) for the percentage overlap in different types of WUIs (WUI-A & WUI-B).

Site type	**Parameters**	**Estimate**	**Std.Error**	**z value**	**Pr($>|t|$)**
WUI-A	(Intercept)	-729.00000	3749.00000	-0.19400	0.84587
	D2WUIA	199.30000	162.40000	1.22700	0.22012
	RhoHou	0.00319	0.13560	0.02300	0.98126
	FVC	292.40000	78.75000	3.71300	0.00022
WUI-B	(Intercept)	-3393.00000	3786.00000	-0.89600	0.37000
	D2WUIB	296.10000	119.10000	2.48700	0.01300
	RouHou	0.02858	0.13570	0.21100	0.83300
	FVC	310.10000	78.05000	3.97200	0.00008

Table 2.3: Results of linear model for large wildfire area. Here, * FireIdx - Fire Index, presence/absence of large wildfires; D2WUIA/D2WUIB - Distance to WUI-A/WUI-B, the distance from fire and random non-fire points to WUI areas; RhoHou - Housing density, the number of houses per km^2 in each Census blocks; FVC - Fuel vegetation cover, the percentage cover of vegetation.

Site	**Parameters**	**Large Wildfires**				**Small Wildfires**			
WUI-A		Estimate	Std. Error	z value	Pr($>|z|$)	Estimate	Std. Error	z value	Pr($>|z|$)
	(Intercept)	1.95514	2.81267	0.69500	0.48698	1.24000	0.02670	46.42	$< 2e^{-16}$
	D2WUIA	-0.02901	0.00922	-3.14600	0.00165	-0.13610	0.00122	-111.35	$< 2e^{-16}$
	RhoHou	-0.00028	0.00011	-2.52800	0.01149	0.00001	0.00000	39.28	$< 2e^{-16}$
	FVC	0.02712	0.00397	6.83800	0.00000	-0.01520	0.00030	-51.29	$< 2e^{-16}$
	ELE	0.00016	0.00011	1.51600	0.12944	-0.00036	0.00001	-34.43	$< 2e^{-16}$
	ASP	0.00120	0.00069	1.73900	0.08209	0.00164	0.00006	27.12	$< 2e^{-16}$
	SLP	0.05763	0.01944	2.96400	0.00304	-0.03489	0.00084	-41.71	$< 2e^{-16}$
	RUGO	-3.54702	2.82999	-1.25300	0.21007	0.01077	0.02318	0.46	0.642
WUI-B		Estimate	Std. Error	z value	Pr($>|z|$)	Estimate	Std. Error	z value	Pr($>|z|$)
	(Intercept)	1.76137	2.81130	0.62700	0.53097	1.43800	0.02540	56.62	$< 2e^{-16}$
	D2WUIA	-0.02017	0.00660	-3.05700	0.00223	-0.10070	0.00088	-115.03	$< 2e^{-16}$
	RhoHou	-0.00029	0.00011	-2.53500	0.01125	0.00001	0.00000	28.62	$< 2e^{-16}$
	FVC	0.02733	0.00396	6.90700	0.00000	-0.01981	0.00029	-67.18	$< 2e^{-16}$
	ELE	0.00020	0.00011	1.78900	0.07355	-0.00035	0.00001	-34.15	$< 2e^{-16}$
	ASP	0.00130	0.00069	1.89800	0.05764	0.00168	0.00006	27.43	$< 2e^{-16}$
	SLP	0.05641	0.01945	2.90100	0.00372	-0.03532	0.00085	-41.68	$< 2e^{-16}$
	RUGO	-3.38495	2.83051	-1.19600	0.23174	0.00563	0.02127	0.26	0.791

Table 2.4: Results of logistic regression model for parameters in WUI definition, topographic parameters, and wildfire occurrence probability. Here, * FireIdx - Fire Index, presence/absence of large wildfires; D2WUIA/D2WUIB - Distance to WUI-A/WUI-B, the distance from fire and random non-fire points to WUI areas; RhoHou - Housing density, the number of houses per km^2 in each Census blocks; FVC - Fuel vegetation cover, the percentage cover of vegetation; ELE-Elevation; ASP-Aspect;SLP-Slope;RUGO-Rugosity.

Site type	**Parameters**	**Estimate**	**Std.Error**	**z value**	**t**
WUI-A	(Intercept)	4684.000	64760.000	0.072	0.94235
	D2WUIA	311.800	123.400	2.526	0.01169
	RouHou	0.020	0.136	0.146	0.88382
	FVC	232.800	85.860	2.711	0.00682
	ELE	-1.452	2.526	-0.575	0.56557
	ASP	23.990	15.580	1.540	0.12395
	SLP	328.300	452.900	0.725	0.46865
	RUGO	-11360.000	65150.000	-0.174	0.86161
WUI-B	(Intercept)	4684.000	64760.000	0.072	0.94235
	D2WUIB	311.800	123.400	2.526	0.01169
	RouHou	0.020	0.136	0.146	0.88382
	FVC	232.800	85.860	2.711	0.00682
	ELE	-1.452	2.526	-0.575	0.56557
	ASP	23.990	15.580	1.54	0.12395
	SLP	328.300	452.900	0.725	0.46865
	RUGO	-11360.000	65150.000	-0.174	0.86161

Table 2.5: Results of linear model for parameters in WUI definition, topographic parameters, and large wildfire area. Here, * FireIdx - Fire Index, presence/absence of large wildfires; D2WUIA/D2WUIB - Distance to WUI-A/WUI-B, the distance from fire and random non-fire points to WUI areas; RhoHou - Housing density, the number of houses per km^2 in each Census blocks; FVC - Fuel vegetation cover, the percentage cover of vegetation; ELE-Elevation; ASP-Aspect;SLP-Slope;RUGO-Rugosity.

2.3.4 Analysis of Buffer distance from WUI perimeters

In subsection 3.2.1, the buffer distances were calculated from the wildfire perimeters. In this section, the buffer distances are calculated from the WUI perimeters and similar statistics are calculated. The percentage overlap of wildfire burned areas with varying buffer distance from WUI-A has been shown in Appendix A: Table A.2 and depicted in Figure 2.4. The percentage of overlapped regions w.r.t. wildfire burned areas (19,517.675 km^2) increased from 4 % to 56 % when the buffer distance from WUI-A changed from 0 km to 5 km. Even with a buffer distance of 1 km, there is a 13 % increase in the percentage overlap (from 4 % to 17 %). Whereas the same overlapped areas w.r.t. WUI-A areas do not increase in percentage overlap (from 3 % to 5 %) with 5 km buffer distance, given that the WUI buffer area also increases significantly (the denominator increases as well). Similarly, Appendix A: Table A.2 shows that the overlap of wildfire burned areas with varying buffer distance from WUI-B. The percentage overlapped w.r.t. wildfire perimeters increased up to 36 % with a buffer distance of 5 km from almost 0.8 % overlap without a buffer around WUI-B. While the percentage overlap in WUI-B buffers did not increase in the same manner and changed to 4.2 % from 1.6 % with 5 km buffer distance (again, due to the increase of the buffer area itself). Figure 2.5 shows that the percentage overlap w.r.t. wildfire perimeters increase linearly with buffer distance for both types of WUIs. However, the rate of increase in percentage overlap is higher in case of WUI-A (top panel) as seen from the slope of the linear equation as compared to WUI-B (bottom panel). On the other hand, the percentage overlap w.r.t. WUI areas do not increase significantly for both the cases.

Therefore, these results (Appendix A: Table A.2, Figure 2.4, and Figure 2.5) give a clear visualization that wildfire events are not limited to the existing WUI, but are more widespread outside it i.e., in the extended WUI. Fire risk maps associated with WUI areas should consider the buffer regions as well. These results also highlight how the two mapping approaches have different sensitivities to the proximity to wildfire events. The discussion above only con-

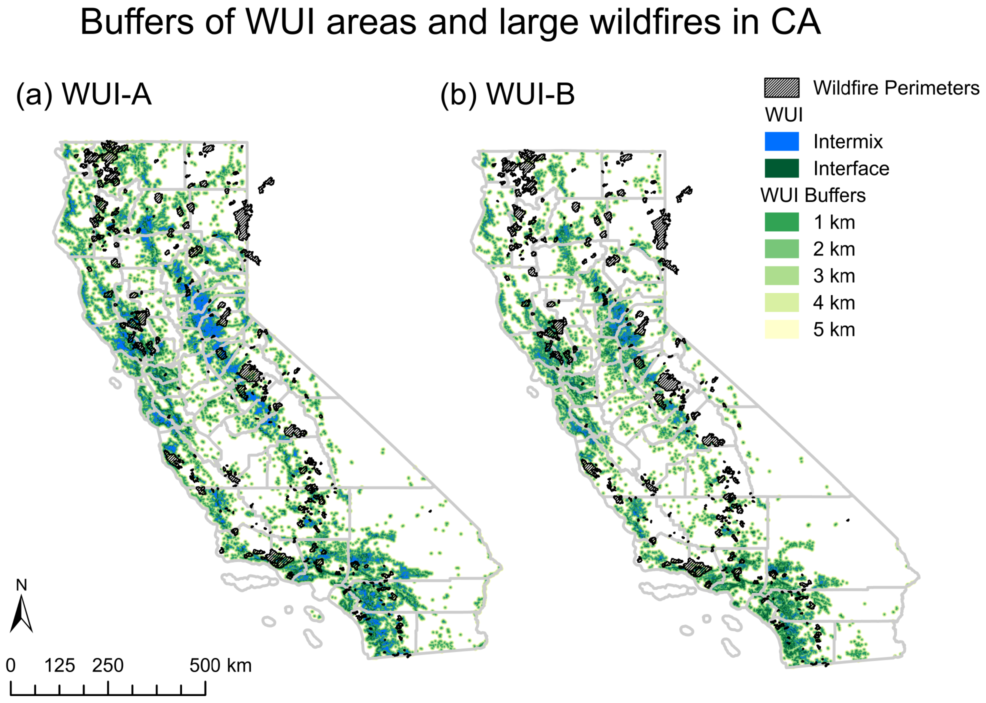

Figure 2.4: The figure on the left panel shows the spatial plot of overlap of buffers of WUI-A with fire perimeters (large fires only, with area > 1,000 ac). While the figure on the right panel shows the spatial plot of overlap between buffers of WUI-B and fire perimeters (large fires only having area > 1,000 ac). Legend in these spatial plots show types of WUI, wildfire perimeters and the areas of WUI-A & WUI-B with varying buffer distance from WUI. Overall, the percentage overlap between the buffers of the existing WUI and wildfire perimeters are higher in WUI-A than WUI-B, and it increases in both the cases on increasing buffer radius.

siders fire perimeters, and it is worth asking whether fire ignitions also originate within or outside these WUI perimeters. This is discussed in the following subsection.

2.3.5 Overlap of WUI with fire ignition points for larger fires (greater than 1,000 ac or 400 ha)

Table 2.1 shows that total 12 wildfires ignited in the WUI-A, out of which only 8 % (1 out of 12) occurred in the WUI-A interface, while 92 % (11 out of 12) ignited in the WUI-A intermix. While only 4 wildfires ignited in the WUI-B out of total 329 fires, and all of those occurred in WUI-B interface, and zero fires ignited in the WUI-B intermix zone (Table 2.1). Thus, more wildfires ignited in WUI-A (3.6 %) as compared to WUI-B (1.2 %) in California. The percentage overlap of fire ignition points with varying buffer distance from WUI-A has been shown in Appendix A: Table A.2 and plotted in Figure 2.5. Here, the number of wildfire ignition points within WUI-A increases drastically when the area of WUI-A increases with buffer distances. The number of ignition points was 72 out of 329 when there was a 1 km buffer around WUI-A and it increased to 217 ignition points at a buffer radius of 5 km, making the percentage overlap to 66 % from 22 %. In addition, Figure 2.5 shows the logarithmic increase in the percentage overlap of fire ignition points within the WUI buffers. However, WUI-A (figure 2.5 on the top panel) shows a higher rate of increase than WUI-B (figure 2.5 on the right panel). Also, Appendix A: Table A.2 shows the number of fire ignition points within WUI-B, increases to 150 out of 329 (almost 46 %) at 5 km buffer radius as compared to 4 out of 329 ignition points (1.2 %) within WUI-B buffers. Clearly, there is a noticeable increase in the number of fire ignition points falling in these WUIs (WUI-A & WUI-B) when the buffer radius increases from WUI. Therefore, our analysis shows that wildfire events do not occur in these predefined WUIs only, rather its frequency and burned area increases as we increase the buffer distance from existing WUIs.

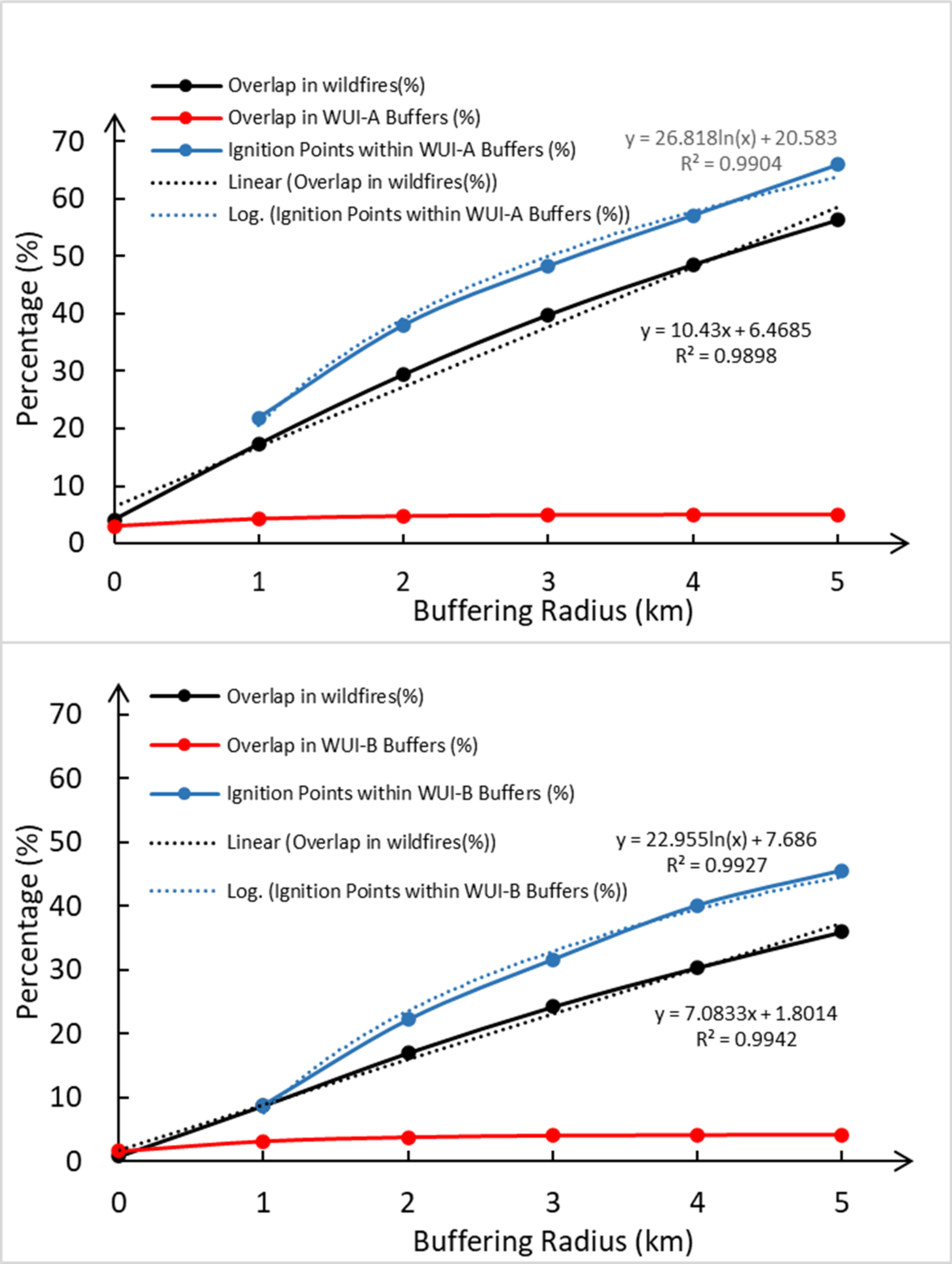

Figure 2.5: The figure on the top panel represents the percentage overlap of wildfire burned areas with WUI-A buffer areas. The solid red line represents the overlap w.r.t. WUI-A buffer perimeters. Percentage overlap w.r.t. wildfire perimeters is shown by solid blue lines and the fire ignition points within the WUI-A buffers are shown by solid black lines. The bottom panel shows the same for WUI-B. Here, X-axis shows the percentage overlap, while buffer distance (km) has been represented on Y-axis. The dotted line indicates linear curve fitting for the percentage of overlap in the area of wildfire perimeters and logarithmic curve fitting for fire ignition points within WUI buffers.

2.3.6 Overlap of WUI with fire ignition points of smaller fires (less than 1,000 ac or 400 ha)

In our analysis with smaller fires (less than 1,000 ac or 400 ha), we found that a total of 63,723 smaller wildfires ignited in the WUI, with only 32.42 % of them igniting in the WUI-A (Appendix A: Table A.7). In WUI-B, smaller fires ignited 18.51 % (Appendix A: Table A.7). As a result, more wildfires erupted in WUI-A than in WUI-B in California. Appendix A: Table A.7 and Figure 2.6 shows the percentage overlap of smaller fire ignition points with varying buffer distances from WUI-A. When the area of WUI-A increases with buffer distances, the number of wildfire ignition points within WUI-A increases. The percentage of ignition points within WUI buffers was 60.17 % with a 1 km buffer radius around WUI-A and increased to 85.11 % with a 5 km buffer radius. Figure 2.6 also depicts the linear increase in the percentage overlap of fire ignition points within WUI buffers (figure 2.6, bottom panel). Similarly, it also shows that the number of smaller wildfire ignition points within WUI-B increased to 79.70 % at a 5 km buffer radius as compared to 50.96 % at a 1 km buffer radius. Furthermore, we revealed that WUI-B has a higher rate of increase than WUI-A (figure 2.6, bottom panel). When the buffer radius from WUI increases, the number of fire ignition points falling in these WUIs (WUI-A & WUI-B) significantly increases. As a result, this study demonstrates that even smaller wildfire events do not occur only in these predefined WUIs, but that their frequency and burned area increase as the buffer distance from existing WUIs increases. It is interesting to note that only a small percentage of ignitions from both small and large wildfires starts at the WUI, and the number of ignitions increases as we move further away from the WUI.

In the previous sections, the existing definitions of WUI have been discussed in the context of wildfire ignition and burned areas to investigate the risk of wildfires in the WUI. One of the three factors that influence fire risk and fire behavior is topography, namely slope, aspect, elevation and surface roughness (along with fuel and weather). Therefore, whether the WUI

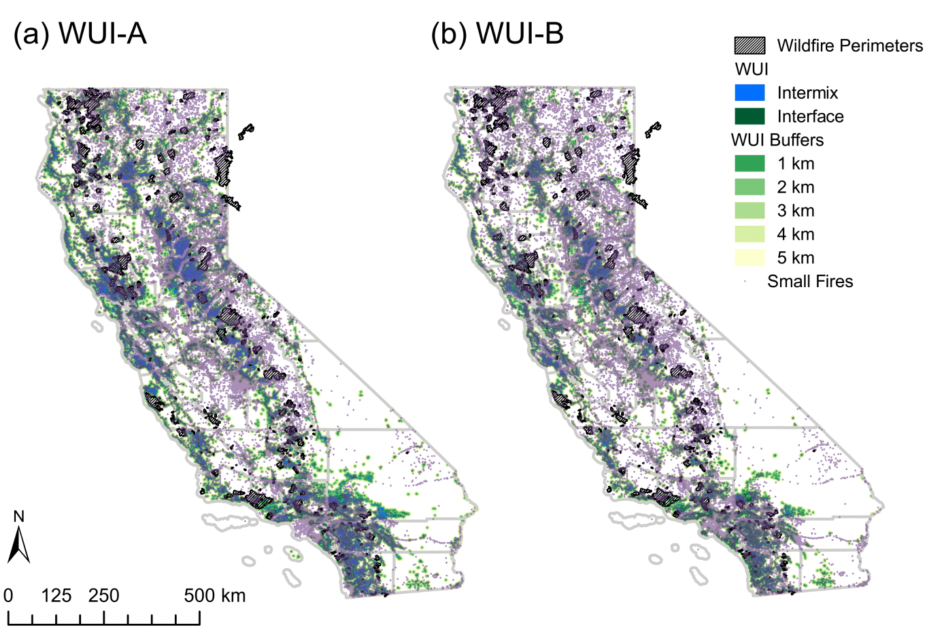

Buffers of WUI areas and Small Wildfire Points in CA

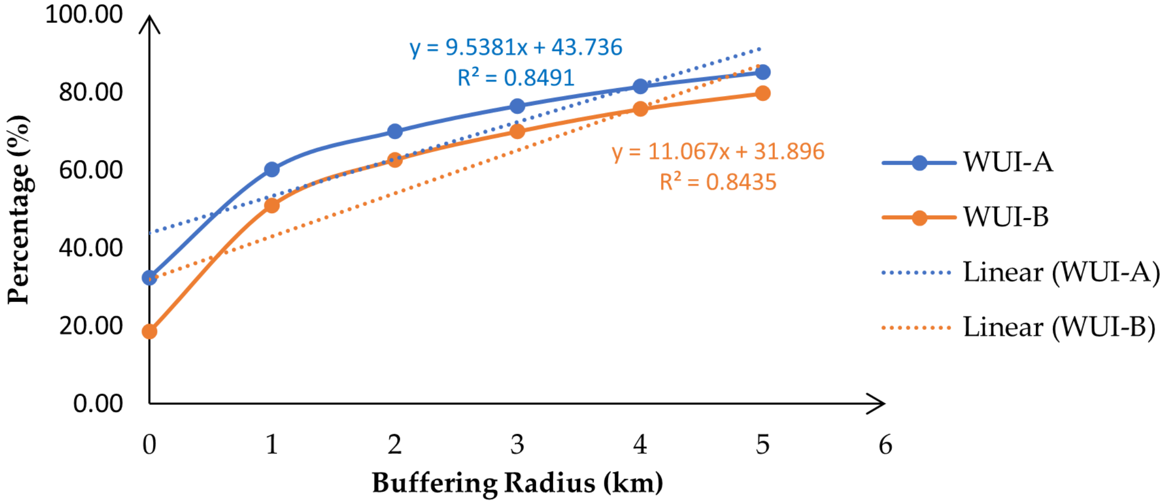

Percentage of small wildfires within WUI-A & WUI-B Buffers

Figure 2.6: The figure on the top left and top right panel shows a spatial plot of WUI-A and WUI-B in CA respectively with the buffers of smaller wildfire ignition points (small fires only, having an area less than 1,000 ac). Legends in these spatial plots show types of WUI (intermix and interface) and the varying buffer distances surrounding WUIs. The figure on the bottom panel represents the percentage overlap of smaller wildfire ignition points with WUI-A and WUI-B buffer areas. Percentage overlap w.r.t. the fire ignition points within the WUIs buffers are shown by solid lines. Here, X-axis shows the percentage overlap, while buffer distance (km) has been represented on Y-axis. The dotted line indicates linear curve fitting for smaller fire ignition points within WUI buffers.

areas in CA are strongly associated with complex topography is worth investigating, to place the WUI fire risk into context and this is discussed in the next subsection.

2.3.7 WUI on the complex topography

Elevation

Figure A.1a (given in the Appendix A) shows the distribution of elevation ranges in CA. Figure A.2a (top left panel) shows the spatial distribution of elevation across CA with a maximum elevation of 4,410 m. In Appendix A.1: Table A.3, we show the percentage overlap of WUI-A in 2010 with 9 ranges of elevation for CA. The histogram plot (Figure 2.7a) shows that a significant WUI percentage lies in the elevation range of 0-100 m for WUI-B (20.17 %) and above 800 m for WUI-A: (21.4 %).

Rugosity

Figure A.2b (top right panel) shows the spatial distribution of surface roughness or rugosity over CA. In Figure 2.7b, analysis of percentage overlap between WUI areas and rugosity for CA yields an interesting outcome. It shows that only 0.4 % of the WUI (WUI-A) are present on the regions with planar surfaces, having rugosity equal to 1. While this number grows to 92.7 % and 97.2 % for WUI-A and WUI-B respectively for surfaces with the rugosity values greater than 1 and less than or equal to 1.1 (Appendix A: Table A.4 in the supplementary file). A significant portion of terrain (55 % and 62 % for WUI-A and WUI-B respectively) is still situated on very low or moderate rugosity between 1.0 and 1.01. Moreover, it shows that almost 99.6 % and 99.8 % of the WUI-A and WUI-B respectively are in the non-planar regions within CA. Therefore, a significant portion of the WUI in this state are located on mild to moderately rough terrain where fire spread rate is higher than the flat surface and controlling large fires are more difficult.

Slope and Aspect

Figure A.2c on the bottom left panel shows spatial distribution of slope over California and most of the regions are in the lower slope ranges. The percentage overlap of WUI-A (WUI-B) with the slope ranges 0-30, 30-60 and 60-86 of the state are 97.72 % (99.4%), 2.27 % (0.6 %) and 0.0003 % (0.003 %) respectively as can be seen in Figure 2.7c (Appendix A: Table A.5 in the supplementary file). The direction that a surface slope faces is called aspect and is defined as the angle between the positive x axis and the projection of the normal onto the x, y plane. In Figure A.2d (bottom right panel), the spatial variation of the aspect has been shown for California and there is almost similar distribution of the direction of the surface slopes as represented by the aspect in all the four quadrants. However, there is almost similar distribution of the percentage overlap of WUI-A and aspect for California in the three quadrants having first (23.82 %), second (23.61 %), fourth (23.4 %) and with a little higher (29.17 %) in the third quadrant (Figure 2.7d; Appendix A: Table A.6). Also, Figure 2.7d shows the percentage overlap of WUI-B and aspect for California and it is highest in the second quadrant (30 %), while the other three quadrants have 23.4 % (first), 23.4 % (third), and 23.1 % (fourth), that is, almost equal percentages.

2.3.8 The importance of parameters in WUI definition to wildfires

The importance of current parameters to wildfire occurrence probability

The pairs plots for current parameters in WUI mapping definition are shown in Appendix A: Figure A.3 and A.4. The red points represent wildfire ignition points and black points represent the random non-fire points. It shows intuitively that the distance to WUI areas

(a) Percentage overlap of WUI-A and WUI-B with elevation over California

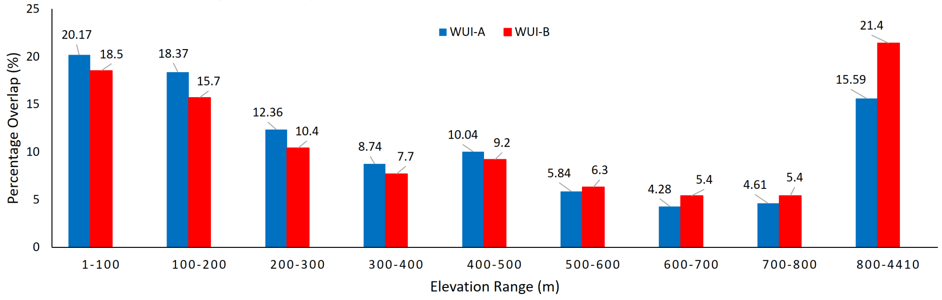

(b) Percentage overlap of WUI-A and WUI-B with rugosity over California

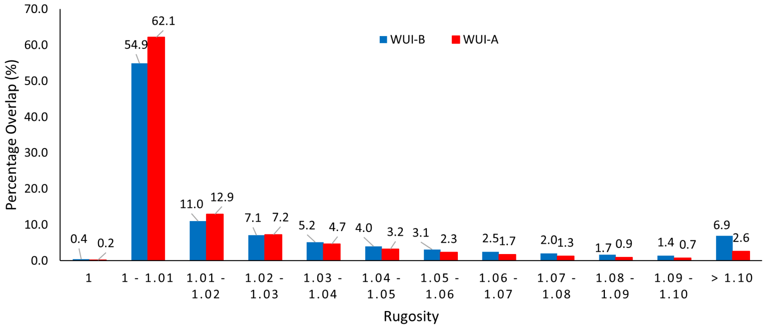

(c) Percentage overlap of WUI-A and WUI-B with slope over California

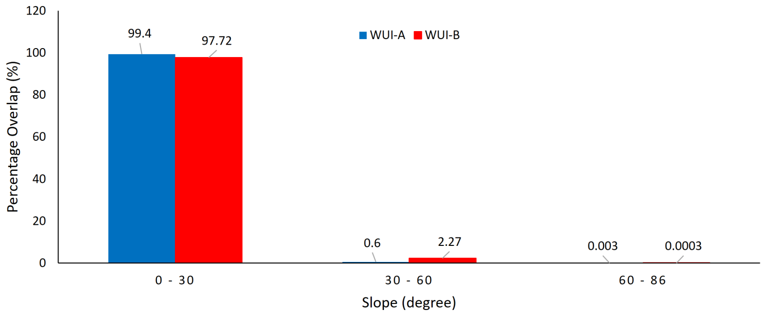

(d) Percentage overlap of WUI-A and WUI-B with aspect over California

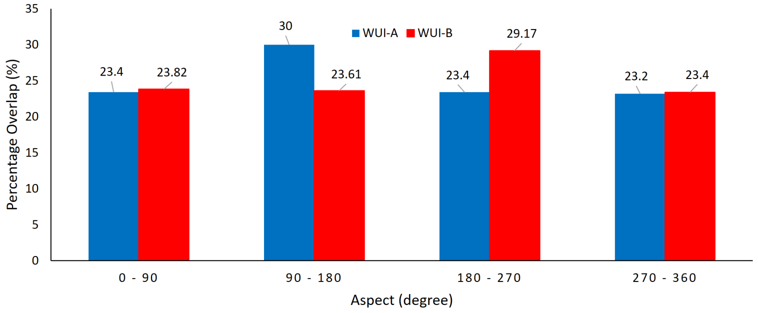

Figure 2.7: Histogram showing the percentage overlap of WUI for California (CA) with (a) different elevation ranges (b) rugosity (c) slope, and (d) aspect. Two colored columns are used to show the different WUI data sources used here for comparison; red column shows the WUI data from Martinuzzi et al. (2015) while blue column is used for CAL FIRE (FRAP, 2015) WUI data set. Here, Y-axis represents overlaps in percentage, while X-axis shows different elevation ranges over CA in meters.

and housing density have significant correlation with wildfire occurrence: both large and small wildfires tend to occur close to WUI areas; large wildfires were concentrated in non-developed areas, while small wildfires occurred at all housing density levels. To further understand the relationship between parameters in WUI definition and wildfire occurrence probability, logistic regression models were fitted to each parameter as a function of wildfire occurrence probabilities. Due to the differences of large and small wildfires in Appendix A: Figure A.3 and A.4, they were fitted separately. As shown in Figure 2.8, within WUI areas and within 10 km of the periphery, the occurrence probability of wildfires is higher than the threshold (0.5), and increases with the shortening of the distance. In terms of the housing density, large wildfires were most likely to occur in low housing density areas. The probability of fire occurrence decreases monotonously with the increase of housing density, and the housing density at the probability threshold is 252 houses per km^2. While most small fires also occurred in relative non-developed areas, their occurrence probabilities are not stable, and there is no significant correlation with the housing density. The relationships between the occurrence probability of large and small wildfires and vegetation density are completely opposite. The occurrence probability of large wildfires increases monotonically as vegetation density increases; while the small wildfire occurrence probability decreases with the increase of vegetation density.

After analyzing the relationship between individual WUI parameters and wildfire occurrence, a logistic regression model integrating all parameters was fitted to show the relative importance of parameters in WUI definition in wildfire occurrence. The estimated coefficients in Table 2.2 show that for large wildfires, vegetation density contributes the most and has positive correlation with occurrence probability. Distance to WUI and housing density have very little effect on large wildfires. While in the small fires, distance to WUI areas contributes the most to their occurrence, followed by vegetation density. Housing density still has little effect on small wildfires.

The importance of WUI parameters in describing wildfire area

In the previous section, the estimated probability of large and small wildfires varies greatly with respect to the corresponding housing and vegetation density. Therefore, we changed the analysis object from the presence of wildfires to the area of wildfires, and integrated all parameters to fit the linear model, so as to observe the changes in the importance of parameters. Due to the limitation of data, only large wildfire areas were analyzed here. The fitted linear model results are shown in Table 2.3. Both the vegetation density and distance to WUI have significant positive correlation with large wildfire areas. Wildfire area would increase with the increase of these two parameters. Thus, the distance to the WUI area has an impact on wildfire occurrence probability, but compared with vegetation density, its contribution can be ignored. However, when it comes to wildfire size, the effects of the distance to WUI areas are significant, large wildfires tend to occur far away from the WUI area, which usually occurs deep in the forests or mountains. The impact of housing density on wildfire size is still negligible.

The importance of complex terrain on wildfires in WUI

Per results in section 3.4, the terrain in WUI is complex, which could also have an impact on wildfire occurrence. Thus four topographic variables (elevation, aspect, slope and rugosity) were fitted in the logistic regression model as functions of wildfire occurrence probability and fire area to show how they relate. As shown in Table 2.4, contributions of each parameter in models for WUI-A and WUI-B are similar, especially for large wildfires. After adding terrain information, the contribution of rugosity to the large wildfire occurrence became prominent. Apart for rugosity, slope also contributes more to large wildfire occurrence, compared to other parameters. In terms of small fires, distance to WUI is still the most prominent parameter in occurrence probability, followed by slope, vegetation density and rugosity. The results from

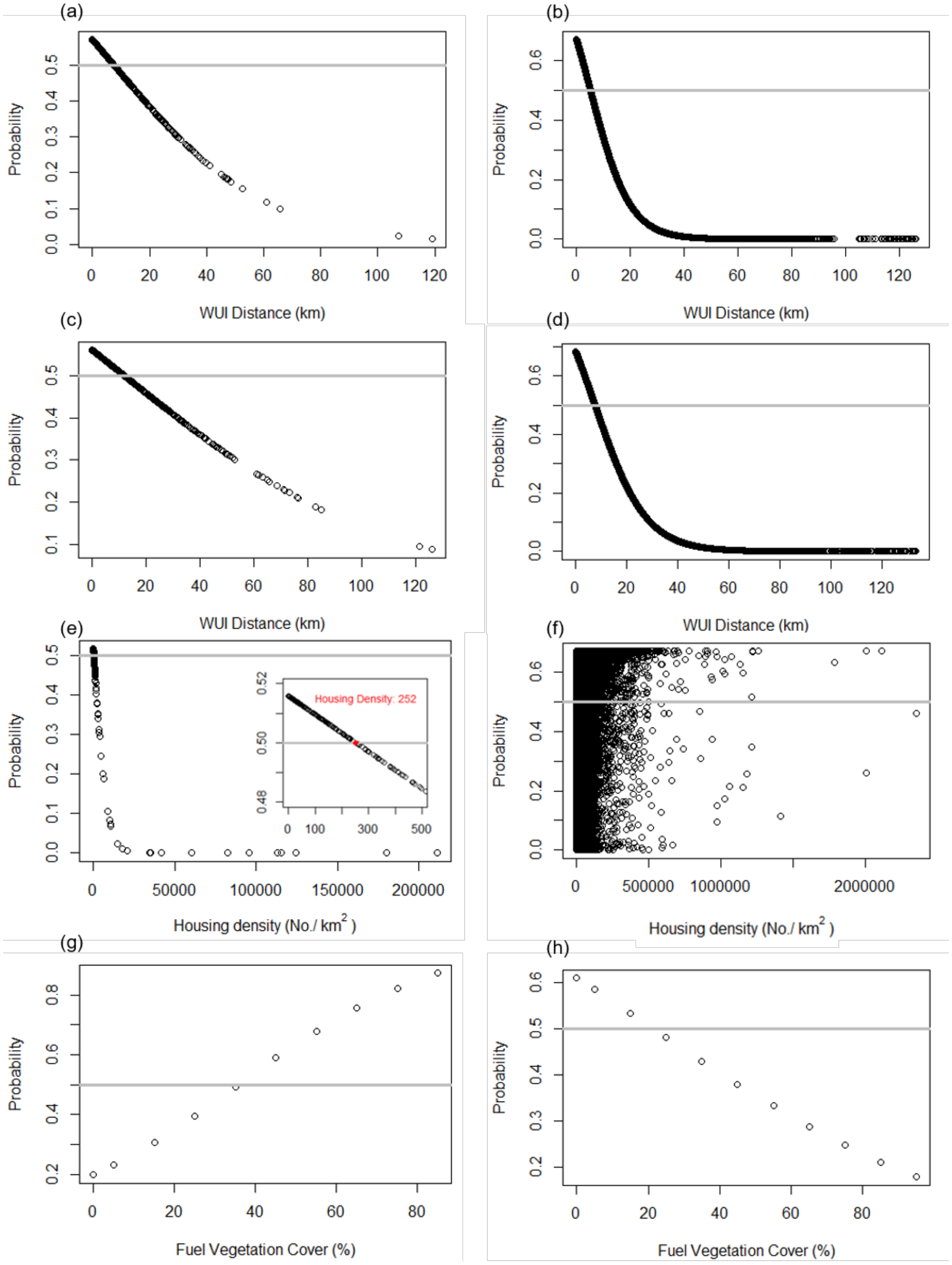

Figure 2.8: Probability curves for the occurrence of wildfires as a function of distance to WUI, housing density and vegetation density, separately: (a) large wildfires, distance to WUI-A; (b) small wildfires, distance to WUI-A; (c) large wildfires, distance to WUI-B; (d) small wildfires, distance to WUI-B; (e) large wildfires, housing density; (f) small wildfires, housing density; (g) large wildfires, vegetation density; (h) small wildfires, vegetation density.

these two models illustrate the complex topography within WUI have an impact on wildfire occurrence.

In addition to the above estimates, the impact of parameters in WUI definition and topographic parameters were explored by fitting a linear regression. The estimated results of models for WUI-A and WUI-B are still similar. Among all the parameters, rugosity affects the large wildfire area much more than other variables, followed by slope, distance to WUI and vegetation density. It provides another confirmation of the influence of topography on the wildfires close to WUI. Comparing Table 2.4 and Table 2.5, the distance to WUI, housing density and elevation contribute to wildfires in different directions but to similar degrees.

2.4 Conclusions

Current wildland fire policy has placed a significant interest in the wildland urban interface (WUI) areas, where increasingly more resources will be allocated for fire prevention, fuel treatment, home hardening against ignition and general fire preparedness such as removal of flammable materials around structures, as well as evacuation planning. In this work we examine the modalities of WUI exposure to wildfires in California by comparing two pre-existing definitions of WUI with respect to past wildfire events. We specifically asked the following questions: (1) Where are the wildfires (a) igniting and (b) burning relative to the WUI? (2) what is the impact of buffer distance in the percentage overlap of fire perimeters and fire ignition points in the WUI? (3) where is the WUI located in terms of elevation and the complexity of the terrain? And (4) what are the relative importance of WUI parameters that impact wildfire occurrence and size within or near the WUI? It was found that a very small percentage of wildfire burned areas were within the WUI areas. Additionally, only a very few numbers of wildfires were ignited within WUI areas. However, when we introduce a buffer distance from the existing WUI perimeters, there is a significant increase in the percentage of wildfire events in terms of fire ignition points. More than 50% of wildfire events occurred at a buffer distance of 5 km from the existing WUIs. This shows that not only WUIs are the zones of wildfires occurrence but also the non-WUI or areas larger than the existing WUI (extended WUI) are highly prone to wildfires. Our results highlight a rapid rate of increase in the percentage overlap of wildfire burned areas and fire ignition points in the extended WUIs. The buffer distance analysis shows the importance of considering spotting fire behavior when considering fire risk in the WUI. While the actual fire front might not burn significantly within the WUI areas, firebrands and burning embers originating from the fire front might travel these buffer distances and under favorable conditions, might be able to ignite structures (Storey et al., 2020). Anecdotal evidence of unburnt and unconsumed trees adjacent to destructed structures in the WUI during high intensity fires (such as Paradise, California, during the Thomas Fire, 2018) bears evidence of these effects. WUI areas do not need to see a 'tsunami or flood of flames', rather they are at a higher risk from firebrand ignitions, also reported in wildfire today (2020). The topography of a landform plays an important role and knowing the location of existing WUIs relative to topographic factors would give us a better understanding of fire dynamics and planning adequate firefighting strategies. This study highlights that a significant portion of the existing WUI in California is on complex topography where, the meteorological factors like wind speed are more favorable for higher rate of fire spread, increased spotting distances and firefighting is difficult due to complex terrain. Last but not the least, we also studied the relative importance of WUI parameters in explaining wildfire occurrence and wildfire area in the WUI. Density of vegetation in the WUI was found to be strongly related to both the occurrence and areas of large wildfires (greater than 1000 ac or 400 ha), while the distance between the wildfire ignition points and the WUI was found to be most significant in describing occurrence of smaller wildfires (less than 1000 ac or 400 ha). When including topographic parameters, surface roughness and slope plays a significant role in describing the occurrence and burned areas of large wildfires. On the other hand, topography plays a less dominant role in explaining the occurrence of smaller wildfires compared to distance to WUI areas. The two existing maps of WUI in California are not found to be significantly different when it comes to the relative importance of WUI parameters in determining wildfire occurrence or burned areas, however, they have different sensitivities in the context of buffer distance or overlaps with previous wildfire events and their relative proportions of interface and intermix areas. This analysis can provide context while planning fuel treatment and home hardening projects and resource allocation for wildfire preparedness in the wildland urban interface areas in the state of California and elsewhere.

Chapter 3

Mapping the wildland-urban interface in California using a vector-based edge approach

3.1 Introduction

People like to live near and within forests for a variety of reasons [Radeloff et al., 2001, Johnson et al., 2005, Bartlett et al., 2000]. In the past few decades, there has been a dramatic proliferation in the number of regions where human-made structures are present within or near wildland vegetation, known as the Wildland-Urban Interface (WUI) [Radeloff et al., 2018, Martinuzzi et al., 2015]. This growth has been attributed to the increasing number of houses near forests and densely vegetated lands in the US since the mid-1900s [Radeloff et al., 2018, Martinuzzi et al., 2015]. In recent years, the term WUI has gained tremendous popularity and has been widely used in the context of wildfire studies. For the purpose of a more accurate analysis of the wildfire occurrence, tracking the location of wildfires, and land use planning, different WUI mapping methodologies have been developed in the past using a wide range of datasets across many countries including Europe, Australia, and Canada [Hanberry, 2020, Miranda et al., 2020, Bento-Gonçalves and Vieira, 2020]. A few studies have used point-based house locations (Li et al., 2022, Risk-factor by First Street Foundation (available on https://riskfactor.com)), while others have implemented a zone-based approach such as census block data for WUI mapping [Radeloff et al., 2005b, Wilmer and Aplet, 2005]. In addition, these maps also depend on the context and purpose of the study; for example, housing-centric or fuel-centric WUI mapping, as demonstrated in Stewart et al. [2009]. WUI maps in Canada show that these features could also be developed for different types of human infrastructure, and a recent study mapped the wildland industrial interface for dense industrial locations, as well as for interfaces for urban regions and commercial properties or infrastructure elements [Johnston and Flannigan, 2017].

In the US, WUI mapping was based on the 2001 federal register definition of the US Department of Interior (US DOI) and the US Department of Agriculture (USDA) which states that WUI are those areas where houses are present within or near wildland vegetation. In the original definition of 2001 federal register, it was not specified whether the intersection of these two types of land use were based on the intersected area or the common boundary of two polygons. However, previous studies were based on areal intersection, i.e., in terms of intersection of the area of these two features. Defined in this way, the resulting WUI has units in in m^2 or km^2. In addition, past WUI maps focus on providing WUI area and do not account for the length of the interface. Moreover, existing WUI maps are based on zonal approaches where either a housing density is defined or a point-based approaches is used (in these cases individual housing locations are identified). These approaches lack consistency on accurate information for all three components of the WUI definition together - housing and vegetation information, an equitable definition of the interface, and the proximity of buildings to large, vegetated areas.

To address this gap, Pereira et al. [2018] argued that a semantically correct definition of an interface (Webster's Third New International Dictionary [Gove, 1986]) should be a plane or other surface forming a common boundary of two bodies or spaces. Therefore, ideally, the result of WUI mapping would be a line segment that could show the common boundary or the physical contact between the boundaries of two features. A vector-based WUI offers greater simplicity in the storage and utilization of information over previous WUI mappings because each WUI line segment can be tagged with information about its surroundings, such as distance to nearby roads, fuel types, population, building and vegetation density, etc. [Pereira et al., 2018].

In this work we aim to develop a vector-based WUI map for the state of California at a high resolution (30 m). Further statistical analysis using these new maps and past wildfires may help with land use planning and identifying high-risk sites. The distance between previous wildfire ignition points and WUI lines will show how far wildfires occurred from the vector-based WUI. In addition, the wildfire burned area with respect to the WUI line segments will provide more information on the severity of the fire as well as the respective risk level.

The resulting WUI features from this approach will be in vector format as opposed to rasters, which have been provided by the previous WUI mapping approaches. In geospatial analysis, vector data are associated with higher geographic accuracy because they depend less on grid size. Moreover, storing, handling, and appending new data layers to vector data is significantly more efficient compared to rasters which are considerably larger in size. In comparison to raster, vector data are much more scalable, amenable to defining connections between topology and network structures, and easier for delineating boundaries and administrative maps in fine resolution. Moreover, storing of vector data is possible without the loss of generalization. It is also possible to preserve geolocation information. Therefore, it is envisioned that developing wildland fire policies under a changing climate and growing trends in WUI land use features will be more efficient using the vector-based

WUI approach as developed in this manuscript.

The key objectives of this study are as follows: (i) map the vector-based WUI in terms of direct and indirect interfaces and determine which WUI is more widespread in CA; (ii) determine the percentage of wildfire perimeters intersecting with the vector-based WUI in CA; (iii) examine the distance between wildfire ignition points and the vector-based WUI to see how far the fires ignited from them since 2010 in CA.

To the authors' knowledge, this paper is one of the first attempts to map the WUI of California using a vector-based approach. This means that rather than providing the areas that WUIs contain, the focus of this approach is to map the boundaries that mark the edges of the interface, which is more useful compared to rasters as discussed in the previous paragraph. This paper is organized as follows. Data and methodology that are used to generate WUI maps for CA are presented in section 2. Section 3 describes the results and discussions of our novel vector-based WUI calculations using building footprint datasets. Finally, conclusions and implementation of this study are given in section 4.

3.2 Data and Methodology

3.2.1 Vegetation data

The vegetation data used for this study was the Landsat-based National Land Cover Database (NLCD, 2016) [Jin et al., 2019], a new generation of NLCD products, released by the U.S. Geological Survey (USGS). It was downloaded from Multi-Resolution Land Characteristics (MRLC) Consortium (available on https://www.mrlc.gov/) and was available at 30 m spatial resolution. The accuracy and robustness of the NLCD 2016 map were also shown by recent studies including Jin et al. [2019] and Homer et al. [2020]. It contained a total of 28 different types of land cover classes over the CONUS. For the purpose of mapping the vector-based WUI, we chose only those vegetation categories which were flammable vegetation and included shrubland, grassland, woody wetlands, and all kinds of forest vegetation (California fire alliance 2001; Radeloff et al., 2005). Specific steps used for extracting the vegetation layer using the ArcMap (10.7.1) tools in ArcGIS (available online: https://desktop.arcgis.com/en/arcmap/) will be discussed in methodology section 2.4.

3.2.2 Building data

A new method of rasterizing building footprint was developed by Heris et al. [2020] and was used in this study. The building dataset was extracted from the Microsoft dataset containing 124,885,597 computer-generated building footprints in GeoJSON format for the US. Regarding the accuracy metrics, the precision of the evaluation set is 99.3 % and the recall is 93.5 %. The California building footprint file implemented in this study contained 10,988,525 computer-generated building footprints in California and was extracted from the US building footprint dataset by Microsoft (2018), then converted to shape file format. We used a rasterized format of Microsoft building footprint datasets, available at 30 m spatial resolution, and used the boundaries of houses for producing the vector-based WUI feature [Heris et al., 2020, Li and Banerjee, 2021]. This boundary data was obtained from Heris et al. [2020] in which the value of each cell represents the area of the cell that was covered by building footprints. The cell values were calculated by developing an algorithm that used High Performance Computing (HPC) [Heris et al., 2020]. This algorithm created a small meshgrid (a 2D array) for each building's bounding box, generating unique values for each meshgrid cell that was further coordinated with NLCD products to make it more usable (projected using Albers Equal Area Conic system) [Heris et al., 2020]. The range of values was from 0 to 900 m^2. To better aid the implementation of building footprint data into large-scale computation, these values are represented as raster layers with a 30 m cell size covering each of the 48 conterminous states.

3.2.3 Wildfire data

Wildfire perimeter data were downloaded from Monitoring Trends in Burn Severity (MTBS), (available on https://www.mtbs.gov/direct-download). MTBS is an interagency initiative whose purpose is to continuously monitor the intensity of wildfires in terms of burn severity and the size of major fires from 1984 to present in the US. It does not cover small fires and includes all those fires in the Western US of 1000 or more acres (400 ha), and 500 or greater acres (200 ha) in the Eastern part of the US (MTBS, 2021). In this study, we used two kinds of MTBS datasets, namely, wildfire occurrence dataset that showed wildfire ignition points, and burned area boundaries datasets, representing wildfire perimeters following the analysis presented by Kumar et al. [2020]. For analyzing the overlap of previous wildfires with the vector-based WUI features, we used wildfire perimeters. While detecting the distance of previous wildfire events from the vector-based WUI features, we used wildfire ignition points data. Since the liner WUI was mapped using the recent land cover and housing information, therefore, to better analyze the WUI maps and their relationship with the previous wildfires, we included only those fires which occurred in the last decade i.e., from 2010 to 2020. The dataset includes 492 fire perimeters in California from 2010 to 2020.

3.2.4 Methodology

The NLCD data were clipped for California from CONUS (see the flowchart in Figure 3.1). The clipped land cover data were converted to polygons from the original raster data using the conversion tool from the ArcMap (10.7.1) geoprocessing tool in ArcGIS (available online: https://desktop.arcgis.com/en/arcmap/). A wildland vegetation layer was generated for WUI mapping using selection by attributes from the attribute table using the ArcMap

(10.7.1) tool in ArcGIS. Only shrub/grassland, herbaceous, woody wetlands, emergent herbaceous wetlands, and forests including evergreen, mixed, and deciduous were selected for the wildland vegetation layer Martinuzzi et al. [2015], Radeloff et al. [2018]. The building raster layers were converted into vectors. The boundaries of the buildings were intersected with the wildland vegetation areas to map the WUI. We computed direct WUI and indirect WUI line segments from these data. These two different data products are defined below.

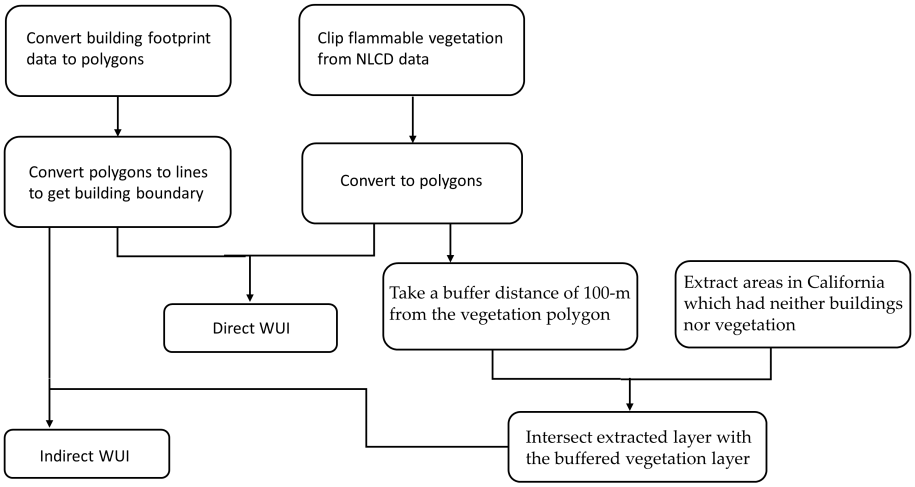

Figure 3.1: Flowchart for mapping vector-based WUI. WUI stands for wildland urban interface and NLCD stands for National Land Cover Data.

Direct WUI was calculated using the intersection tool from the ArcMap (10.7.1) in ArcGIS using the vegetation polygon and housing boundary, and it represents the direct physical contact of buildings with the flammable vegetation. There is always a higher risk of damage to the communities living at the direct WUI feature as compared to those living at the indirect WUI as studied by Pereira et al. [2018]. To map the indirect WUI, first, we took a buffer distance of 100 m from the vegetation polygon and then extracted those areas in California which had neither buildings nor vegetation using the erase tool from the ArcMap (10.7.1) in ArcGIS. We then intersected the extracted layer with the buffered vegetation layer. Finally, we intersected the previously intersected layer with the housing boundary to get the Indirect WUI (see Figure 3.1). We did not intersect the vegetation layer with a buffer and housing boundary to avoid the repetition/duplication of indirect WUI lines with the direct WUI. The resulting WUI, both direct and indirect, have units of length in meters (m) with $[L]1$ dimension. It is important to note that the 100 m buffer distance was taken following the approach of Pereira et al., 2018, however, the indirect WUI could be recalculated using any buffer distance deemed necessary following our workflow.

3.3 Results and Discussion

3.3.1 Wildland fire ignition frequency

A total of 492 wildfires occurred in California from 2010 to 2020 according to MTBS. These included both human-caused fires as well as lightning-caused fires. In the left panel of Figure 3.2, we show the countywide fire frequency in California. Some counties are characterized by the occurrence of more than 20 wildfires, as shown with the colorbar. Figure 3.2 (right panel) depicts the wildland vegetation cover used in the mapping of vector-based WUI. More information on both the fire ignition points and the vegetation layer can be found in the supplementary materials. Further information on the fire ignition data and the building footprints can be found in section S1 in the supplementary materials.

3.3.2 Vector-based WUI features in California

Direct WUI is a vector-based WUI feature that is shown in Figure 3.3, with lengths in meters (m) and is represented with a green colorbar. Enlarged portion of Figure 3.3 on the right panel depicts a clearer visualization of the different vector-based WUI segments (direct

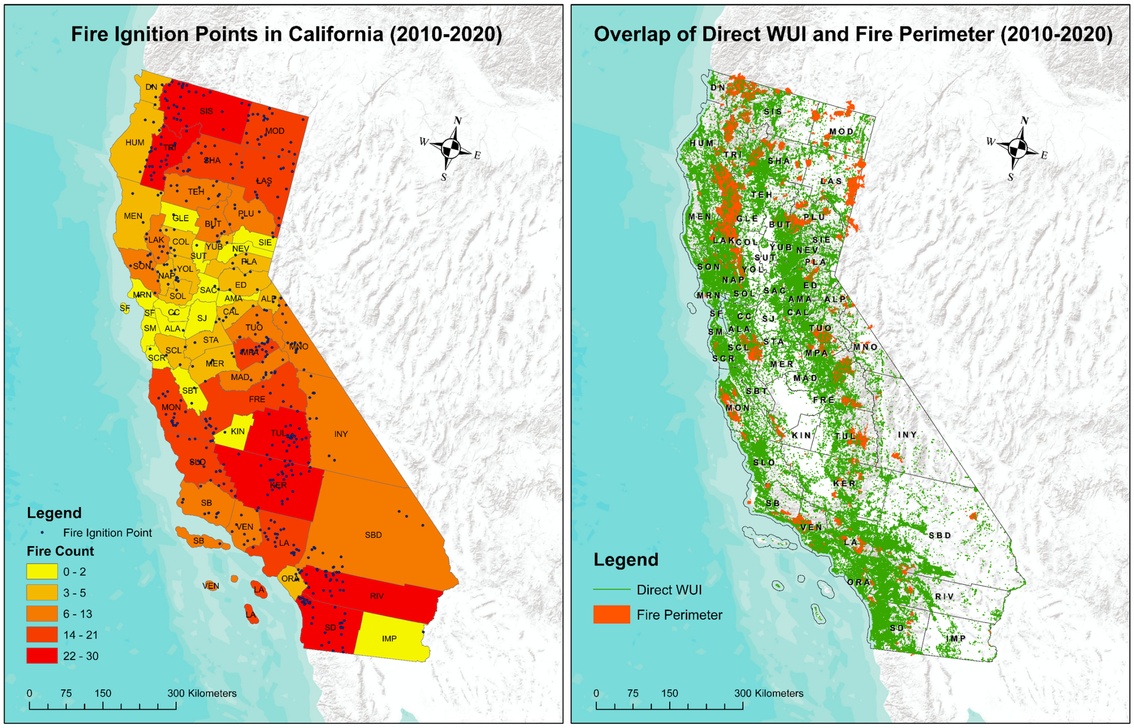
Fire Ignition Points in California (2010-2020)

Overlap of Direct WUI and Fire Perimeter (2010-2020)

Figure 3.2: The left panel on the figure above shows wildfire frequency in all the counties of California from 2010 to 2020. The blue markers represent the wildfire ignition points in the respective counties, while the colorbar shows the fire counts for each county during this time period. The right panel on the figure above shows the spatial pattern of NLCD data, the wildland vegetation data used to map the vector-based WUI for California at 30 m resolution; it includes three kinds of forest, shrubs, and emergent herbaceous & woody wetlands; white color represents the water bodies and other vegetation types that were not included for mapping the vector-based WUI.

and indirect WUI) and Non-WUI segments. It became possible only due to the finer-scale mapping using building footprint data at 30-m resolution. In addition, such a fine-scale WUI map provides more detailed information related to both housing and wildland vegetation. Figure B.1 shows an enlarged map of Figure 3.3 where the empty spaces near the indirect WUI are the regions that have neither buildings nor vegetation. It is interesting to note that this vector-based approach clearly identifies and delineates the boundaries between wildland vegetation and buildings which might be at risk due to wildfires as opposed to traditional raster based zonal approaches. Clear identification of WUI boundaries at such a fine resolution might also help develop more precise fuel treatment (such as fuel breaks) and home hardening strategies down to individual building footprints.

We calculated that the total length of direct WUI in California is 119,640,741 m. It has 672,435 segments with a maximum segment length of 5,958 m. In contrast, indirect WUI has a total length of 164,706,030 m, which comprises a total number of 3,009,978 segments, with the maximum length of a segment being 5,022 m. Therefore, the direct WUI has a lower total segment length than the indirect WUI. In addition, the maximum length of a segment and the statistical parameters like mean, median, and mode are higher for the direct WUI. However, the total number of segments is lower for direct WUI as compared to indirect WUI. This difference in segment counts reveals that the direct WUI is less fragmented than the indirect WUI (Figure 3.4).

A greater length of vector-based WUI in a region corresponds to a higher likelihood of wildfire risk due to the presence of flammable vegetation nearby. Moreover, a greater length of WUI segments also indicates the presence of extended interfaces between flammable vegetation and human settlements which would mean a higher risk of damage to the lives, properties, and health of a larger number of communities nearby that region. In the next section, we examine the relationship between fire ignitions and the classes of vector-based WUI segments mapped in this study.

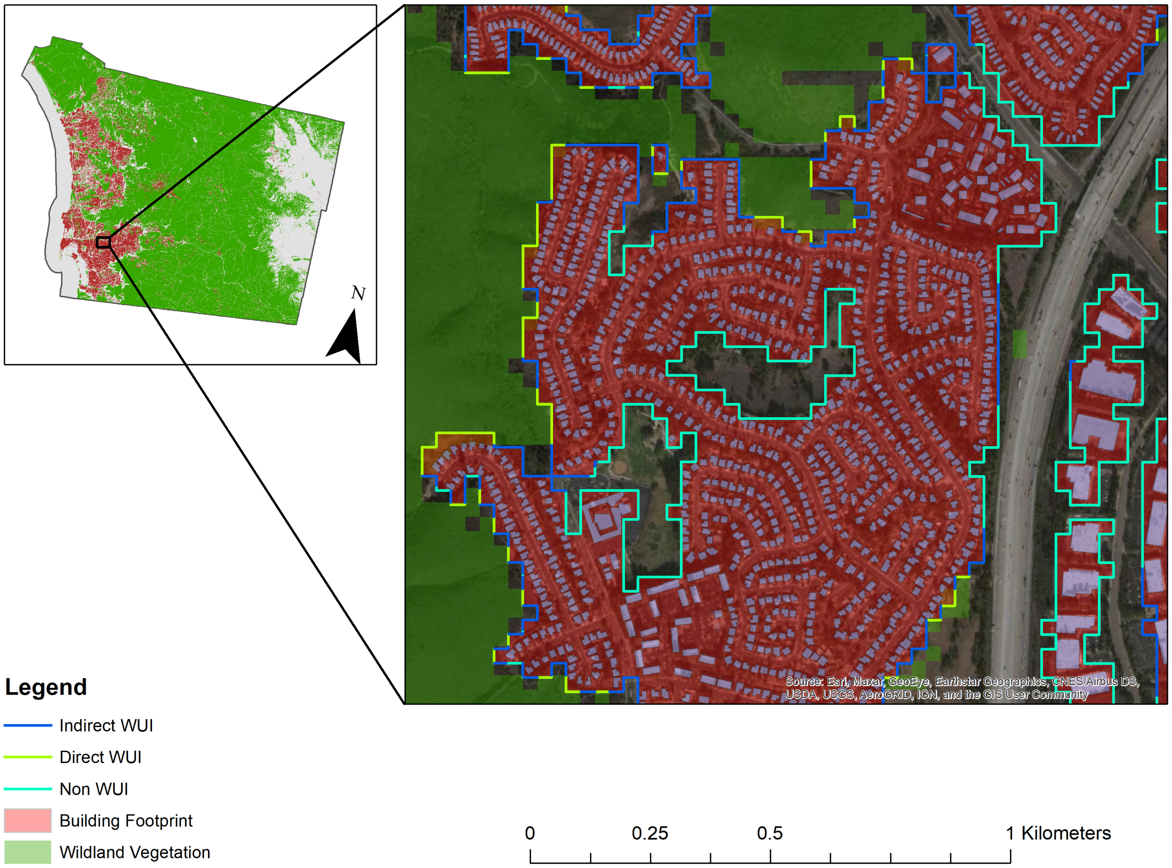

Source: Esri, Maxar, GeoEye, Earthstar Geographics, CNES/Airbus DS, USDA, USGS, AeroGRID, IGN, and the GIS User Community

Figure 3.3: The left panel on the figure above shows the spatial pattern of Microsoft building footprints and vegetation data in San Diego. A section of the County map has been enlarged to depict the direct, indirect, and non-WUI lines as well as their actual visualization at 30 m resolution. This is displayed in the right panel of the figure above.

3.3.3 Overlap of wildfires and vector-based WUI

Figure 3.4 depicts the overlap of wildfire perimeters with direct and indirect WUI from 2010 to 2020. This result clearly indicates that overall, there is a low percentage of overlap between the direct WUI and previous large wildfire perimeters. However, a maximum of up to 19 % of all direct WUI segments in a California county overlap with past wildfire perimeters (left panel, Figure 3.5) and this percentage is 26 % for indirect WUI. Thus, the results show that the majority of the WUI segments did not encounter wildfire perimeters during the last decade. This finding is consistent with the recent observations by Kumar et al., 2022. In the case of indirect WUI, though, the percentage overlap between indirect WUI segments and wildfire perimeters, while still low, is higher than what we observe with direct WUI (Figure 3.5). Moreover, some counties have higher overlap between the vector-based WUI segments and large wildfire perimeters. This is attributed to some recent wildfires with a significantly large burned area. For example, due to the devastating wildfire in Butte County in 2018 (i.e., the 2018 Camp Fire), the maximum value of percentage overlap increases significantly. However, we also note that the percentage overlap of wildfire perimeters and indirect WUI might vary depending on how we choose the wildland vegetation perimeters when mapping the indirect WUI. On the other hand, 76 % of all fires burning in or into CA encountered direct WUI segments and 51 % of all wildfires encountered an indirect WUI segment in CA between 2010 and 2020.

3.3.4 Distance of fire ignition points from vector-based WUI features

Using the fire ignition data points for the large wildfires obtained from MTBS, we computed the distance between the ignition points and the nearest direct and indirect WUI lines, using

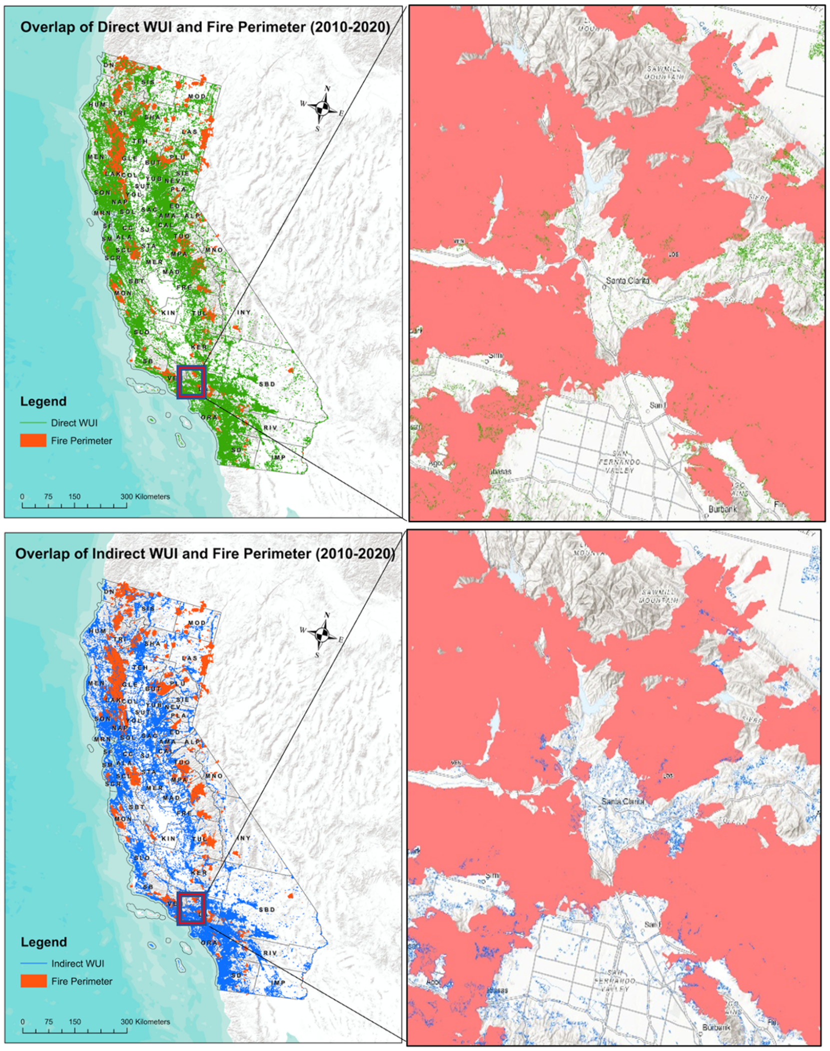

Figure 3.4: The figure shows the overlap of California historic wildfire perimeters (2010-2020) with direct WUI (top left panel) and indirect WUI (top right panel). Legends with green and blue lines represent direct and indirect WUI respectively in the above figure. The right-hand panels present enlarged views of the relevant sections of the two maps for clearer visualization.

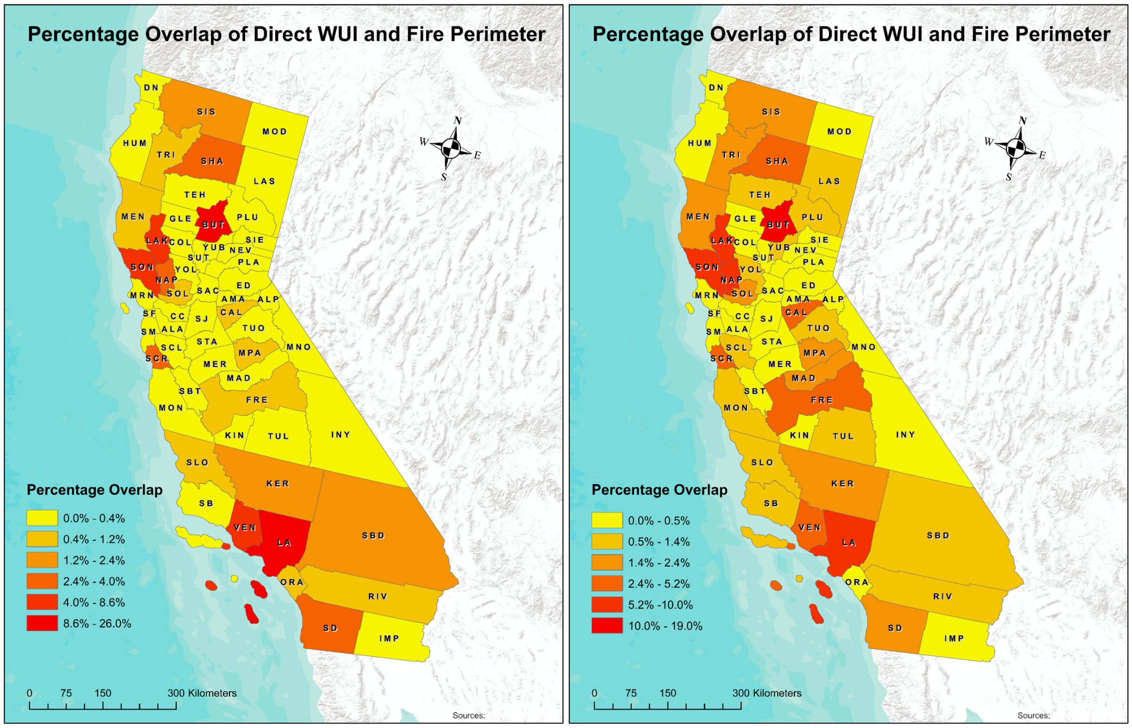

Figure 3.5: The figure shows the countywide percentage overlap of total direct WUI (left panel) and total indirect WUI (left panel) of California with wildfire perimeters from 2010 to 2020. Colorbar shows the increase from yellow (low) to red (high) for the respective counties in California.

the proximity near function of the ArcMap (10.7.1) tool in ArcGIS. We found that a higher percentage of fires ignited in close proximity to direct WUI as compared to those in the vicinity of indirect WUI (see Table B.1 in the supplementary materials or Figure 3.6) which is elaborated further below.

In Figure 3.6, we show the histogram plots for the distribution of distance of wildfire ignition points from the direct, and indirect WUI segments against the proportion of total number of fires that occurred between these distance classes. We observe that in case of the direct WUI, 157 fires ignited out of a total of 492 fires i.e., 32 % of fires ignited within the range of 0-1 km on either side of direct WUI. The percentage of fire ignition has decreased continuously as we increase the distance farther away from the direct WUI. And it dropped to only 6 % of total fires that were ignited beyond 5 km of the direct WUI in California. In case of indirect WUI, we found a different trend of the fire ignitions with distance ranges on the either side of the indirect WUI. Only 75 fires ignited within 1 km distance on either side of the indirect WUI, which accounts for 15 % fires within this range. However, the percentage ignition has increased from 15 % to 21 % in the range of 0-1 km to 1-2 km distance from indirect WUI features respectively. Additionally, a significant portion of the fires i.e., 28 % ignited beyond 5 km on either side of the indirect WUI and this accounts for 139 fires out of a total 492 fires that ignited past 5 km from the indirect WUI in California from 2010 to 2020.

To summarize, more than 60% of the fires ignited within 2 km of the direct WUI segments, while about 35% of the fires ignited within 2 km of the indirect WUI segments. As a result, even though direct WUI has a lower total segment length in California, it has a larger potential of fire ignitions in its vicinity based on prior fire incidence data. As a result, we can observe that there are lower risks of wildfire ignition close to indirect WUI than to direct WUI.

To further quantify how far fires ignited from the vector-based WUI features we performed

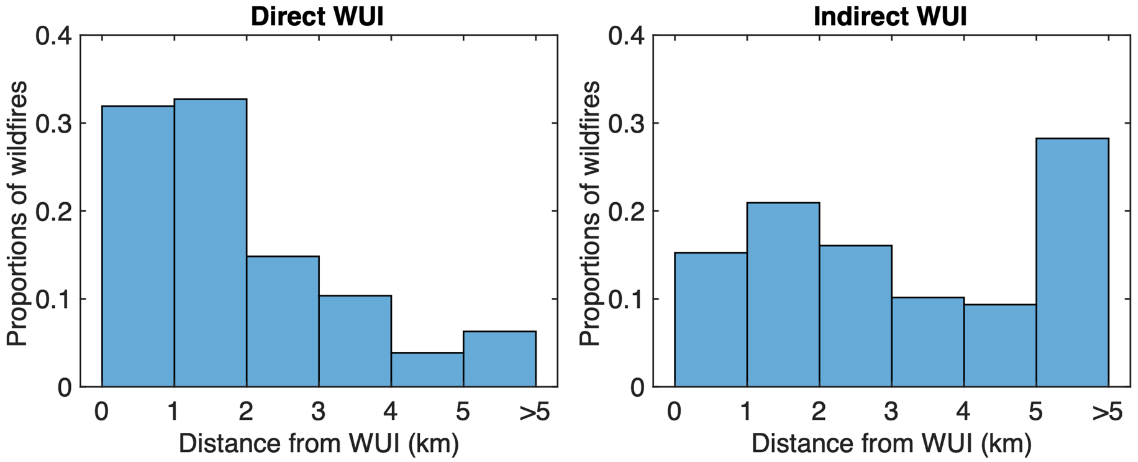

Figure 3.6: The figure shows two histograms for the distribution of distance of wildfire ignition points (2010-2020) on the either side from vector-based WUI features (left panel: direct WUI and right panel: indirect WUI). Histogram for the direct WUI shows a continuous decreasing percentage of wildfires; while it is neither continuously increasing nor continuously decreasing and has two peaks for the indirect WUI).

statistical analyses and used different curve fittings to choose the best fit curve for the distance between fire ignition points and both direct and indirect WUI. We chose 14 different distributions to test the best fit as shown in Table B.2 and Table B.3 in the supplementary information. Our analysis reveals that the 'gamma with three parameters' distribution is the best fit curve for the direct WUI (see top panel of Figure 3.7). This curvature had the highest p-value of the 14 possible distributions at 0.225 (see Table B.2 in supplementary materials). However, for indirect WUI, the 'lognormal with three parameters' distribution with a p-value of 0.956 is the best fit curve as can be seen in the bottom panel of Figure 3.7 (see Table B.3 in supplementary materials). Further information on the curve fitting procedure can be found in section S2 in supplementary materials.

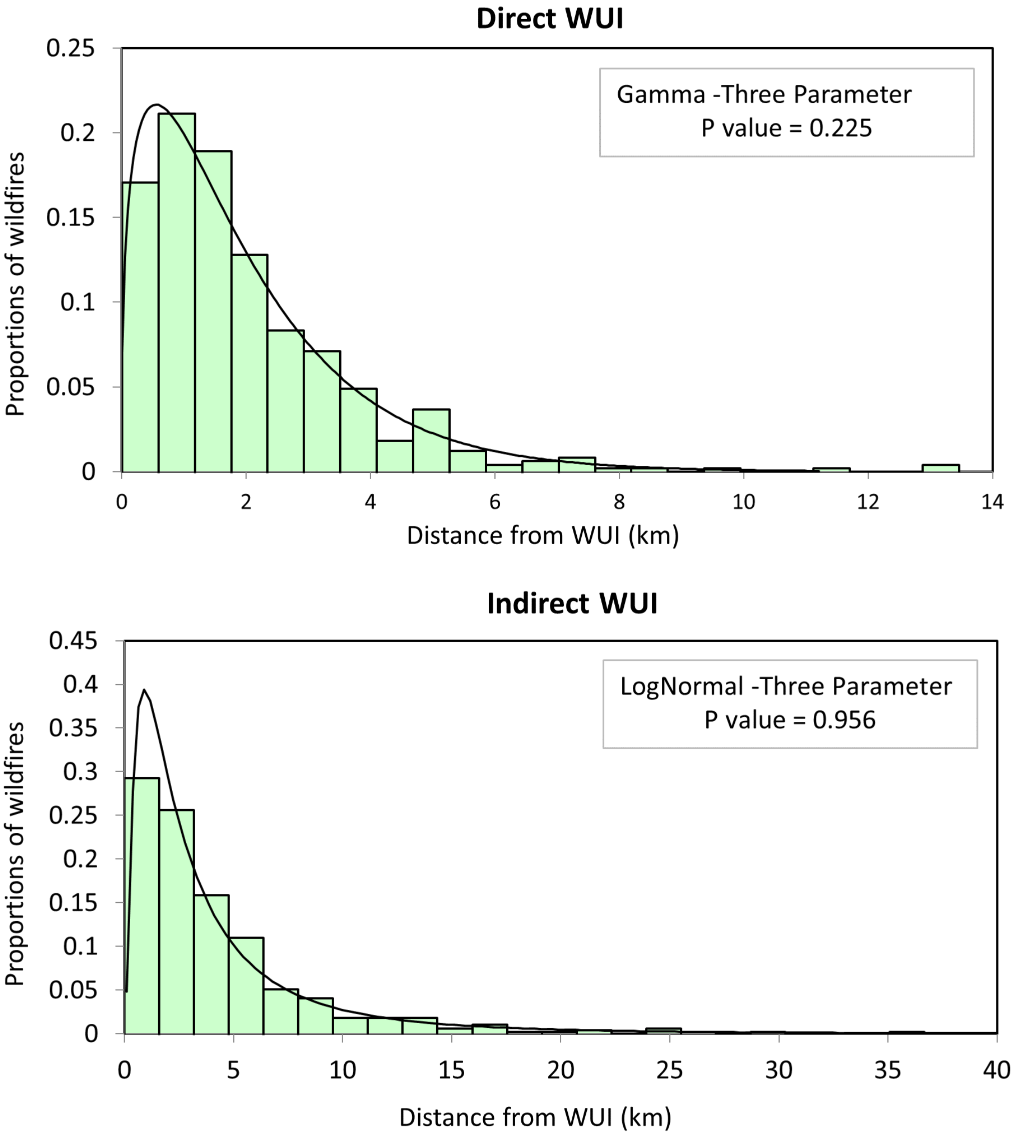

Figure 3.7: The figure shows the distribution of the best fit plot for distance (km) of wildfire ignition points (2010-2020) from direct WUI (top panel) and indirect WUI (bottom panel).

3.4 Conclusions

Past studies showed that different WUI maps were developed for the CONUS using a variety of datasets and different mapping methodologies. However, none of these focused on WUI mapping based on the vector-based intersection of vegetation and housing boundary. In this study, we mapped vector-based WUI at 30 m resolution using building footprint and NLCD land cover data. We defined two types of vector-based WUI i.e., direct, and indirect WUI. Direct WUI has direct physical contact between flammable vegetation and housing boundary and thus, has a higher risk of fires. While indirect WUI is mapped by the intersection of housing, and 100 m buffer boundary surrounding flammable vegetation and therefore it has a lower probability of fires. We had three objectives in the study – namely: (i) map the vector-based WUI in terms of direct and indirect interfaces and determine which WUI is more widespread in CA; (ii) determine the percentage of wildfire perimeters intersecting with the vector-based WUI in CA; (iii) examine the distance between wildfire ignition points and the vector-based WUI to see how far the fires ignited from them since 2010 in CA.

Regarding objective 1, results revealed that the direct WUI had a lower total segment length and is less scattered than the indirect WUI in California.

Regarding objective 2, we found that the overlap between wildfire burned areas and WUI segments is generally low for most counties. A maximum of up to 19 % of all direct WUI segments in a California county overlap with the past wildfire perimeters and this percentage is 26 % for indirect WUI. Therefore, the majority of the WUI segments did not encounter wildfire perimeters during the last decade in California. On the other hand, a majority (76 %) of all fires burning in or into CA encountered direct WUI segments and about half (51 %) of all wildfires encountered indirect WUI segments in CA between 2010 and 2020.

Regarding objective 3, we found that higher percentage of fires ignited in the vicinity of direct WUI because of a higher extent of human activities as compared to indirect WUI.

Hence, even though direct WUI has a lower total segment length in California, it has a larger potential of fire ignitions in its vicinity based on the historical wildfires. More specifically, 63 % of large wildfires between 2010 and 2020 ignited within 0-2 km range of direct WUI and 35 % ignited within the same range of indirect WUI in California. Therefore, in this study, we show that the direct WUI are more prone to wildfire ignition as compared to the indirect WUI. Moreover, the distribution of the distance from the fire ignition points from the vector-based WUI features follow a 'gamma with three parameters' and a 'lognormal with three parameters' distribution for direct and indirect WUI respectively. The advantage of the proposed vector-based framework in this work is that it can be appended with additional geospatial information and remote sensing data. It can also be rapidly updated with different values of the parameter such as the buffer distance used to map the indirect WUI for a specific location at the same fine scale resolution. This flexibility is not currently available with the raster based zonal approaches to map WUI which uses census data that be updated once per decade. Moreover, clearly delineating the actual boundaries of the wildland urban interfaces will be also useful for land managers and fire authorities to identify precise strategies for home hardening, fuel treatment and overall wildfire risk mitigation.

Chapter 4

Evaluating the performance of the WRF model in simulating winds and surface meteorology during a Southern California wildfire event

4.1 Introduction

Wildfires are associated with high suppression costs and have significant socioeconomic consequences [Burke et al., 2021, Stephens and Ruth, 2005, Stephens et al., 2016]. The intensity and frequency of wildland fires in California (CA) have increased in recent years, causing significant damages to human health, lives, and properties [Bowman et al., 2020, 2011, Cannon and DeGraff, 2009]. Reliable simulation of wildfire behavior can help decision-makers mitigate the impacts of these extreme events [Andrews et al., 2007, Jiménez et al., 2018, Wang et al., 2022].

One specific type of wildfire events which are characterized by high fire intensity and a significantly high rate of spread, are the Santa Ana wind driven wildfires. Santa Ana wind (SAW) events are associated with specific weather conditions where hot, dry, and gusty wind blows from the deserts east of the Sierra Nevada to the coast of southern California [Glickman, 2000, Raphael, 2003, Westerling et al., 2004, Jin et al., 2015, Brewer and Clements, 2019], usually occurring in the months of fall, spring, and winter. The SAW events during fall are known to considerably elevate fire risk because these events often co-occur with times when live fuel moisture is very low following the hot and dry Mediterranean summer [Westerling et al., 2004, Keeley and Syphard, 2019].The wind events are usually easterly or northwesterly, and characterized as foehn-type winds. The hot, dry, and gusty conditions associated with SAW events have fanned many large fires, including, the Camp Fire in 2018, the Woolsey Fire in 2018, the Thomas Fire in 2017, the Witch Fire in 2007, and the 2003 Cedar Fire, among many others [Masoudvaziri et al., 2021, Brewer and Clements, 2019].

In this study, we focus on one of the SAW driven wildfire events, the Witch Fire, to evaluate the performance of the WRF model with several different parameterizations. On Sunday, October 21, 2007, at 12:35 PM PDT, the Witch Creek Fire or Witch Fire started in Witch Creek Canyon near Santa Ysabel as a result of strong SAW blowing down a power line and releasing sparks into the wind (California Department of Forestry and Fire Protection (CAL FIRE) 2019 report). After burning 400 acres (1.6km^2), the fire was quickly contained on October 23 (10news.com, 2007), although spot fires within its perimeter continued to burn until October 26, when it eventually merged with the expanding Witch Fire (Orange County Authority report of 2007). It caused an estimated damage of 1.3 billion (2007 USD) as reported in CAL FIRE (2007).

Large wildfire events, such as the SAW driven Witch Fire event, create their own weather [Coen et al., 2013]. A variety of models exists which can be used to predict wildfire behavior and estimate fire-weather characteristics, such as, WRF, WRF-Fire (Sullivan [2009], Coen et al. [2013]). However, conventional fire behavior models fail in predictive efforts for highly severe wildfire events [Mölders, 2008, Di Giuseppe et al., 2016, Clarke et al., 2013]. This is because large-scale and high-intensity fire events release a significant amount of heat and energy, and the dynamical processes that characterize the resulting fire-atmosphere interaction are not represented well in fire behaviour models [Lindley et al., 2019, Varga et al., 2022, Neary, 2022, Cruz and Alexander, 2013, Jiménez et al., 2018].

While using mesoscale models to predict the fire weather associated with a wildland fire, it is important to understand how well the models are able to simulate the transport of mass, momentum, heat, and energy occur [Bryan and Fritsch, 2002, Coen, 2018, Mallia et al., 2020]. The Fire-atmosphere interaction takes place primarily (since can be feedback with plumes in troposphere or stratosphere) within the atmospheric boundary layer. The predictability, thus, depends on the choice of PBL parameterization schemes, which parameterize vertical mixing, and near surface turbulent processes. Some of the most widely used PBL schemes are categorized into local and non-local schemes [Skamarock et al., 2019], based on how they represent the interaction among different columns of the atmospheric layers within the PBL. Some of the previous studies on wildfire simulation used the WRF model to investigate how well these PBL schemes can capture smoke transport and meteorological conditions during a wildland fire [Lu et al., 2012, Brewer and Clements, 2019, Fovell and Cao, 2017, Fovell et al., 2022]. However, the sensitivity of the WRF model to the PBL schemes in resolving the fire weather during large scale wildfire events is not clear from the existing literature.

Another factor that is important while resolving atmospheric boundary layer processes in Numerical weather prediction (NWP) models, is the grid resolution. In order to resolve the atmosphere, NWP models must use a three-dimensional grid. Higher grid resolution usually results in better predictability of small scale turbulent processes. Small horizontal grids necessitate more levels in the vertical direction and faster time steps, which requires higher computational cost [Collins et al., 2013].

Forecasts for numerical weather prediction are typically generated at 10 km for global models and around 1 km for regional models [Jiménez et al., 2018]. The HRRR model provides one of the highest resolution forecasts over a 3 km grid resolution over the contiguous United States [Jiménez et al., 2018, Benjamin et al., 2016]. Even though this resolution is widely advocated as high, it is insufficient to resolve the interaction between wind and topography around complex terrains [Jiménez et al., 2018]. Therefore, the choice of grid resolution plays an important role in predicting weather [Giunta et al., 2019, Collins et al., 2013, Wedi, 2014].

Some of the existing convectional mesoscale models, such as, WRF, WRF-Fire, have the capability to capture the day-to-day weather as well as related processes and parameters of the extreme events. On contrary, when it comes to capture the fire-weather conditions with such models during a wildfire, it is important to use coupled fire-weather fire models. This is because of the ability of coupled fire-atmosphere [Lagouvardos et al., 2019, Coen et al., 2013] to implement changes in the mass, momentum, and heat fluxes, relatively well than weather model (WRF) during fire-atmosphere interaction.

In the WRF model, there is a capability to compute the feedback of fire-atmosphere interaction at each time step and improve the performance of the model. This is done using a two-way nested domain at which the fire and atmosphere interact and feeds information back and forth. The operational forecast stations do not use coupled fire-atmosphere to predict the fire-weather associated with wildfires. In addition, the grid resolutions are not that high to avoid the higher computational cost. We do not know how well the WRF model would simulate a wildfire event at a finer grid resolution when fire model in not coupled with it, especially, the Mega fires like the 2006 Witch Fire. To fulfill the gap, we test the capability of the WRF model to simulate a Mega fire, without the fire model coupled with it and with finer horizontal grids, two widely used PBL schemes (YSU & MYNN), and an active feedback.

The goals of this study are as follows:(1) to quantify the predictability of a NWP model in capturing fire-weather; (2) to evaluate the sensitivity of the PBL scheme in capturing fire weather; and (3) to examine the effect of horizontal grid resolution on the prediction of meteorological parameters associated with a wildfire. We use the Weather Research and Forecasting (WRF) model to simulate the weather conditions during the wildfire event. Our results will advance the understanding of optimal strategies for operational forecast of fire-weather associated with large wildfires using mesoscale model simulations.

This study is organized into four main sections. Section 1 provides the background and motivation for this study. The data and methodology used to perform the sensitivity of PBL schemes and grid resolutions are presented in section 2. Section 3 describes the results and discussion of our analysis. Conclusions are presented in section 4.

4.2 Data and Methodology

4.2.1 Datasets used

We use the North American Regional Reanalysis (NARR) dataset (Mesinger et al. [2006]) that is available at 12 km horizontal grid resolution and at every three hourly interval to provide initial and boundary conditions to the Weather Research and Forecasting (WRF) model (Skamarock et al. [2019]). In this study, we run the model for five days i.e., from 21th October 2007 to 26th October 2007. In addition, we use the hourly surface measurements (wind speed at 10 m, temperature at 2 m, and relative humidity at 2 m) from the U.S. Environmental Protection Agency (EPA) Air Quality System (AQS) data (https://www.epa.gov/aqs) for model validation. Meteorological data, such as wind speed at 10 m, temperature at 2 m, and relative humidity at 2 m, are extracted from individual AQS surface stations within the WRF innermost domain and are compared against the WRF predictions. Finally, we use AmeriFlux data from the SCw station to compare surface heat and momentum flux observations against WRF outputs.

4.2.2 Model configuration and experimental set-up

We use WRF model version 4.3.1 [Skamarock et al., 2019] with three two-way nested domains. The initial and boundary condition for the model are provided from NARR data at every three hourly interval. We choose two sets of PBL schemes, namely, the Yonsei University (abbreviated as YSU throughout this manuscript) [Hong et al., 2006] and the Mellor-Yamada-NakanishiNiino Level 2.5 scheme (abbreviated as MYNN throughout this manuscript) [Nakanishi and Niino, 2004] and combined with the two sets of grid resolutions. Therefore, we perform a total of four simulations as shown in Table (4.1) using various permutations of grid resolution and PBL schemes. During the simulation, we stored WRF outputs at every 1-hour interval. We compare results of all simulations with observations on an hourly basis.

All the simulations are initialized at the same time and run from 00 Z UTC (5 p.m. Pacific time) on October 21st to 00 Z UTC (5 p.m. Pacific time) on October 26th 2007, allowing 12 hours for model spin-up and 4 days & 13 hours for simulations. Two sets of horizontal grid resolutions are used for model set-up in our study: 9 km, 3 km, and 1 km and 36 km, 12 km, and 4 km for the outermost, middle, and innermost domains respectively. We used 33 vertical pressure levels with the top level at 13,706 m for all WRF simulations.

In the coarser grid experiments, the mesoscale domain (d01) has a horizontal extent of 3240 km by 3240 km, with 90 grid cells in both X and Y directions, while domain 2 (d02) has 151 grids in both X and Y directions with a domain size of 1812 km by 1812 km, and domain 3 (d03) has a horizontal extent of 1084 km by 1084 km, with 271 grid cells in both X and Y directions. The time step for integration is 216 seconds for d01 in the coarser grid simulation.

Since this ensures the model stability required for the simulation, it is recommended to set the time-step in the WRF model between 3*dx to 6*dx, where dx is in km for the outermost domain and the time-step is in seconds [Skamarock et al., 2005, Hutchinson, 2007]. In the finer grid experiments, the mesoscale domain (d01) has a horizontal extent of 3213 km by 3213 km, with 357 grid cells in both X and Y directions, while domain 2 (d02) has 601 grids in both X and Y directions with a domain size of 1803 km by 1803 km, and domain 3 (d03) has a horizontal extent of 1081 km by 1081 km, with 1081 grid cells in both X and Y directions. The time step for integration is 30 seconds for d01 in the finer grid simulations. The outputs for innermost domain (d03) are stored at every hour and the parent time step ratio (outer/inner) is 3 for all simulations.

We use the rapid radiative transfer model (RRTM) (Mlawer et al. [1997]) for the longwave radiation schemes and the Dudhia scheme (Dudhia [1989]) for the shortwave radiation scheme throughout the three domains for all simulations. For surface physics, we use the Revised MM5 Scheme (Jiménez et al. [2012]) throughout the three domains for all simulations. Furthermore, we use the Unified NOAH land-surface model (Mukul Tewari et al. [2004]) as the land surface scheme throughout the three domains for all simulations. For the microphysics parameterization, we use the Purdue Lin scheme (Chen and Sun [2002]) for all simulations and in all domains. For the cumulus parameterization scheme, we choose the Grell 3D Ensemble scheme (Grell [1993]) for two outermost domains in all experiments, while for the innermost domain, we do not use cumulus parameterization in any of the experiments.

4.2.3 Data analysis and quality check

While comparing WRF outputs at specific locations with the AQS surface station dataset, a few quality control criteria are established. As a gap-filling strategy, some stations embed repeated values of the last valid observation for specific variables. We filter out the repeated

PBL	**Resolution**	**Time step (second)**	**PBL**
(scheme)	d03	d01	(reference)
MYNN	1 km	30	[Nakanishi and Niino, 2004]
MYNN	4 km	216	[Nakanishi and Niino, 2004]
YSU	1 km	30	[Hong et al., 2006]
YSU	4 km	216	[Hong et al., 2006]

Table 4.1: The table shows the list of simulations performed for this study using two PBL scheme options (YSU and MYNN2.5) at two different horizontal grid resolutions (36 km, 12 km, 4 km and 9 km, 3 km, 1 km) in the WRF model. The 'Resolution' in the table represent the horizontal grid resolution and it is shown for the inner-most domain (d03) only.

values of meteorological variables from the AQS data while calculating correlation statistics when it gets repeated for more than three continuous hours. Furthermore, we also filter out those stations that contain missing data values at one or more time instants.

The Python interpolation tool is used to extract the relevant meteorological variables from

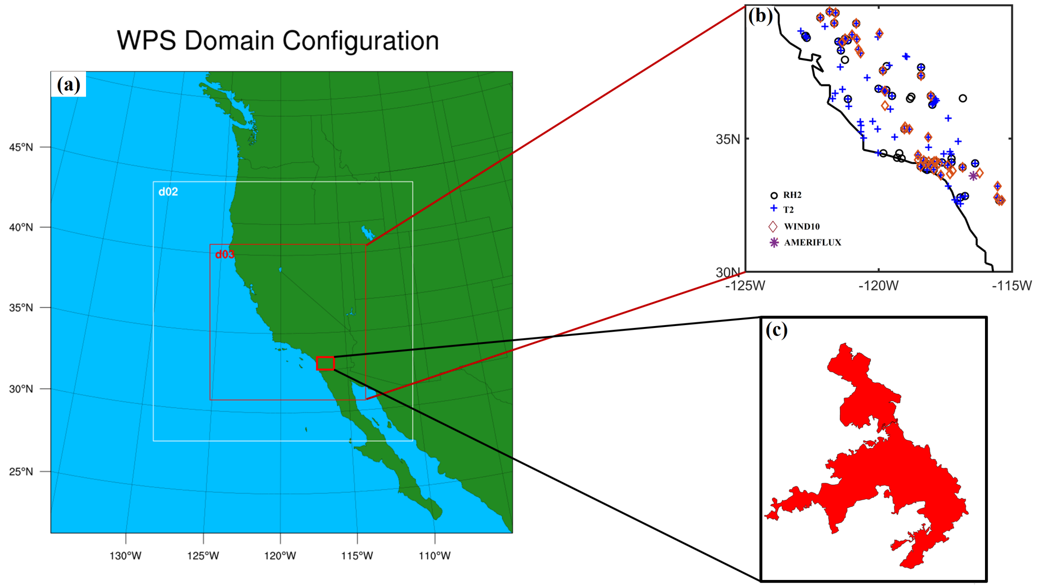

Figure 4.1: The WRF Preprocessing configuration is shown in panel (a) with three different two-way nested domains (d01, d02, and d03). All the results in this study are shown from d03. The panel (b) shows the number and location of different stations used for the model validation for temperature, relative humidity, wind speed, and heat flux. The Witch Fire area is shown in panel (c) from the San Diego County.

WRF outputs within the innermost domain of the model. After quality control, For comparing hourly temperatures at 2 m height (T2), 90 AQS stations are used. For comparing hourly relative humidity at 2 m height (Rh2), we use a total of 48 stations. Similarly, we use a total of 43 AQS stations for the purpose of comparing wind speed at 10 m height (Wspd10). The Pearson's correlation coefficient and the root mean square error (RMSE) statistics are used to evaluate these comparisons. One specific site near the Witch Fire location (site 1006, Latitude 32.842242 N and Longitude -116.768225 W) is investigated in more detail and the time series of T2, Rh2, and Vapor Pressure Deficit (VPD) are compared against WRF outputs.

4.2.4 PBL schemes

The Yonsei University scheme (YSU) [Hong et al., 2006] and the Mellor-Yamada-Nakanishi-Niino (MYNN) [Nakanishi and Niino, 2004] schemes are two of the most commonly used PBL schemes in the WRF model. Since the YSU PBL scheme expresses turbulence in terms of mean variables rather than additional prognostic variables, it is a first-order closure scheme. The YSU PBL scheme also incorporates an explicit treatment of the entrainment layer at the top of the PBL, is an improvement to the medium range forecast (MRF) PBL scheme [Hong and Pan, 1996]. The YSU scheme is also classified as a "non-local" scheme because, in addition to parameterizing the effect of turbulence caused by small eddies, it also considers transport caused by convective large eddies [Hong et al., 2006, Skamarock et al., 2008].

The MYNN scheme is based on a prognostic equation for turbulent kinetic energy (TKE) and is a 1.5-order local closure scheme [Nakanishi and Niino, 2004, 2006]. It is an improvement of the Mellor–Yamada–Janjic (MYJ) PBL scheme [Janić, 2001]. The MYNN scheme uses the results from large eddy simulations (LES) to generate expressions of stability and mixing length as contrary to MYJ, which derives these expressions from observations [Njuki et al., 2022, Cohen et al., 2015]. However, like other local closure schemes, the MYNN scheme does not account for deeper vertical mixing caused by large eddies [Cohen et al., 2015].

Surface heterogeneity and land-cover information is not adequately represented at the coarser resolution in the model. Therefore it is worth testing whether a finer grid resolution would capture the finer scale surface characteristics, which would enhance surface feedback processes and thereby affect the near surface meteorology. The choice of grid resolution, therefore should affect fire-weather simulations. Most of the operational weather prediction systems use 3 km to 5 km horizontal grids for predicting local and regional weather conditions from an hourly to weekly basis. At the coarser resolution, the WRF model is unable to resolve some of the small scale processes and effect of finer scale features in the weather prediction, such as clouds and turbulence, etc. In addition, model at such resolutions fail to capture the physical features, for example, near coastal regions, there are presence of clouds during the evening period and coarser resolution model may not represent them well. Similarly, in the regions of complex topography, models do not resolve the orography well and thus fail to capture their effect on some of the underlying processes, resulting in a poor prediction.

4.3 Results and Discussion

4.3.1 Comparing meteorological parameters against surface station observations

Aggregated analysis

The correlation for temperature (T2) (panels a, b, c, d), relative humidity (Rh2) (panels e, f, g, h), and wind speed (WSPD10) (panels i, j, k, l) for AQS surface stations in the innermost domain (d03) are shown in Figure 4.2 shows against WRF outputs at the same locations. The R-squared value, R^2, and root mean square error (RMSE) for all variables are reported in Table 4.2.

We find that there is significantly strong correlation among the surface station observations and WRF outputs. The overall prediction of temperature at 2 m for all stations is sensitive to the horizontal grid resolution regardless of the choice of PBL schemes. Therefore, simulations with 1 km grid resolution are found to have higher correlation for surface temperature compared to simulations with 4 km (Figure 4.2) resolution. For the coarser resolution simulations, the MYNN scheme yields higher correlation as opposed to the YSU PBL scheme.

For relative humidity at 2 m height above the surface, correlations observed for all surface stations are significantly lower than surface temperature and much more variability is observed in the datasets. However, no significant sensitivity to grid resolution or the choice of PBL scheme is noticed. The RMSE is slightly higher for the coarser resolution simulations for both PBL schemes.

For wind speed at 10 m height, the correlation between all surface station observations and WRF outputs for all four simulations is higher than relative humidity but lower than surface temperature. These correlations are also not as sensitive to PBL schemes but are strongly dependent on grid resolution, while finer scale simulations yielding stronger correlations.

From Figure 4.2 and Table 4.2, we can generally conclude that while surface temperature and surface wind speed are captured relatively well compared to surface relative humidity, there is also a significant spread in the data while considering all weather stations in the inner domain of WRF. Moreover, the choice of the PBL scheme does not have much impact on predicting meteorological parameters on the surface, although finer scale simulations provide improved predictions. In the next section, we investigate whether there is a spatial variability while comparing the surface stations against WRF outputs.

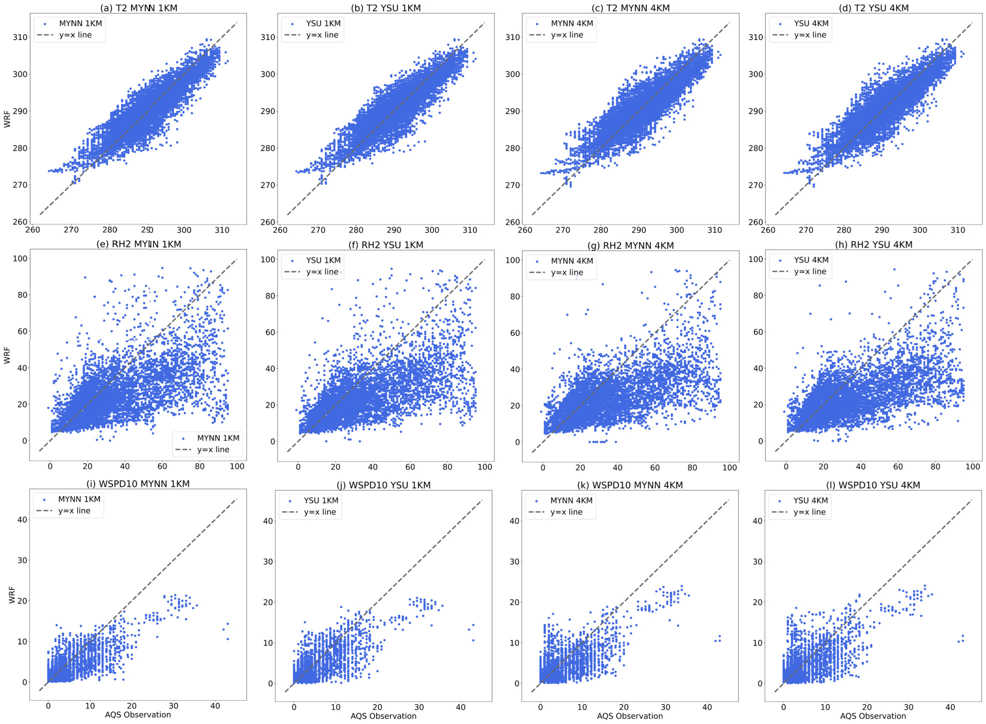

Figure 4.2: Correlation plots for T2, Rh2, and WSPD10 for all the stations within the innermost domain (d03). The results are presented from 1 km and 4 km using YSU and MYNN PBL schemes and with the observational data (AQS) in order to show (a) T2 at 1 km for MYNN;(b) T2 at 1 km for YSU;(c) T2 at 4 km for MYNN;(d) T2 at 4 km for YSU;(e) Rh2 at 1 km for MYNN;(f) Rh2 at 1 km for YSU;(g) Rh2 at 4 km for MYNN;(h) Rh2 at 4 km for YSU;(i) Wspd10 at 1 km for MYNN;(j) Wspd10 at 1 km for YSU;(k) Wspd10 at 4 km for MYNN; and (l) Wspd10 at 4 km for YSU in the respective panels.

PRM	**Site**	**MYNN 1KM**		**YSU 1KM**		**MYNN 4KM**		**YSU 4KM**	
		R^2	RMSE	R^2	RMSE	R^2	RMSE	R^2	RMSE
T2	d03	0.8	3.32	0.8	3.32	0.77	3.49	0.53	5.98
	1006	0.76	2.71	0.79	2.48	0.66	4.04	0.76	3.19
Rh2	d03	0.38	20.36	0.38	20.51	0.38	21.00	0.38	21.18
	1006	0.81	9.58	0.90	8.04	0.77	11.54	0.79	11.03
Wspd10	d03	0.57	3.21	0.57	3.12	0.49	3.34	0.48	3.35
	6001	0.53	4.12	0.64	3.57	0.44	4.53	0.36	5.53

Table 4.2: The summary table showing RMSE and R^2 values for T2, Wspd10, and Rh2 from the different simulations at site 1006, site 6001, and for all stations combined within the d03 (inner-most domain) domain in California.

Spatial variability of meteorological parameters at the surface level

The spatial variability of the correlation for the meteorological variables among the surface stations and WRF outputs during the simulation period of the Witch Fire event is depicted in Figure 4.3. We find that temperatures at 2 m is better captured over valleys than mountains 4.3. Coastal sites are associated with lower correlation for temperature as shown with the lighter color in Figure 4.3. This could be because the model grid for coarser resolution simulations are situated partially on both land and ocean. Furthermore, presence of clouds near the coastal regions could be another reason for poor model performance. It is important to note that MYNN performs relatively better than YSU at 4 km in capturing the spatial variability of temperature. A significant spatial variability is also observed for relative humidity and surface wind speed. In the next section, we focus on one specific site (1006) which is proximal to the Witch Fire location.

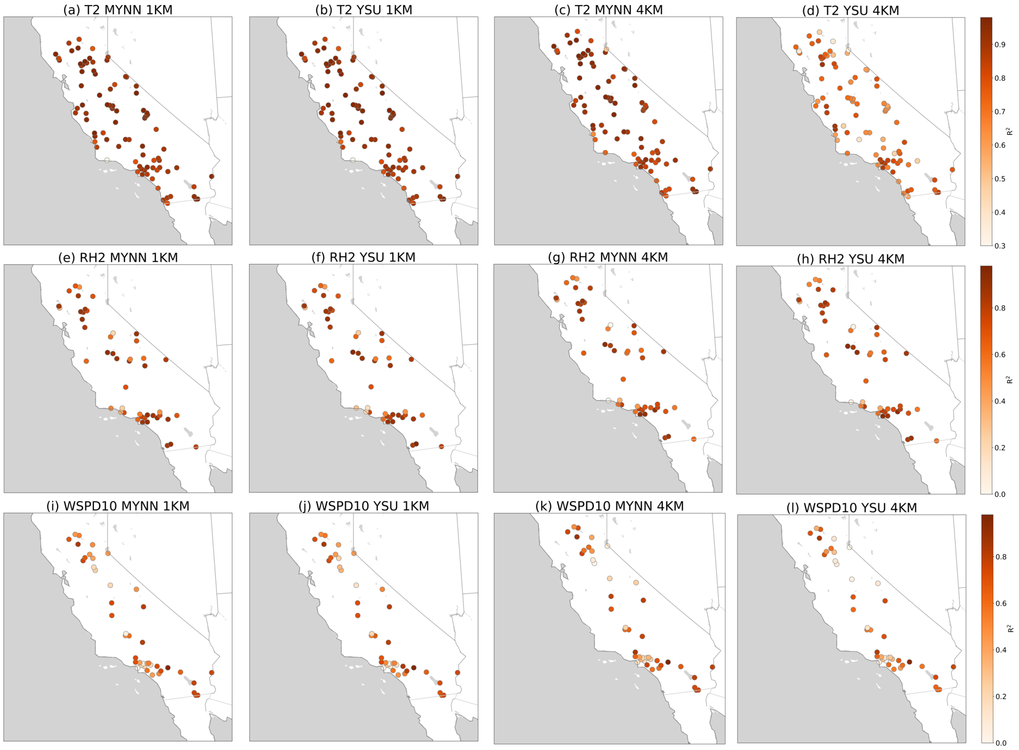

Figure 4.3: Location-wise plots for T2, Rh2, and WSPD10 for all the stations within d03. The results are computed from 1 km and 4 km using YSU and MYNN PBL schemes and with the observational data (AQS) in order to show (a) T2 at 1 km for MYNN;(b) T2 at 1 km for YSU;(c) T2 at 4 km for MYNN;(d) T2 at 4 km for YSU;(e) Rh2 at 1 km for MYNN;(f) Rh2 at 1 km for YSU;(g) Rh2 at 4 km for MYNN;(h) Rh2 at 4 km for YSU;(i) Wspd10 at 1 km for MYNN;(j) Wspd10 at 1 km for YSU;(k) Wspd10 at 4 km for MYNN; and (l) Wspd10 at 4 km for YSU in the respective panels.

4.3.2 Fire weather at a single site

Correlation with surface station observations

Table 4.2 also shows the correlations for the station 1006 [32.84 N, 116.77 W] along with the aggregated correlations for all sites as discussed before. It can be assumed that this station is influenced by the presence of the Witch Fire. It is interesting to note that while correlations for temperature are high for site 1006, the correlations are significantly improved for relative humidity and wind speed compared to the aggregated correlations, at least for the higher resolution simulations. Similar to the aggregated correlations, higher resolution simulations perform better than coarser resolution simulations for site 1006 as well. Moreover, the YSU scheme performs better compared to the MYNN scheme except for wind speed for the 4 km resolution simulations. The correlations for vapor pressure deficit are significantly high as well for all simulations. This observation is particularly interesting in the context of fire weather as VPD is a strong predictor for the hot and dry conditions that promote wildfire ignition and propagation.

Time-series of Meteorological Parameters

The mesoscale meteorological conditions and SAW gusts during the 2007 Witch Fire event intensified the fire spread and the fire intensity. To evaluate the ability WRF model in simulating the surface meteorological conditions of the fire, such as, temperature at 2 m (T2), relative humidity at 2 m (Rh2), and wind speed at 10 m (Wspd10) during the event, we compare modeled and observed time-series at the surface stations as shown in Figure 4.4. We observe that the performance of WRF model is better in capturing the temporal variation of meteorological parameters at site 1006 at 1 km resolution simulations for both MYNN and YSU PBL schemes as compared to at 4 km simulations (fire start time: October 21, 2007, at 19:35 UTC). The surface temperature and VPD is under-predicted by WRF, while the relative humidity is over-predicted at site 1006 (Figure 4.4). No clear trend of under or over prediction is observed for wind speed.

These results suggest that even without an explicit fire-weather parameterization, WRF is able to capture the meteorological conditions during a large wildfire event relatively well. In the next subsection, we investigate how well the surface sensible heat flux is captured.

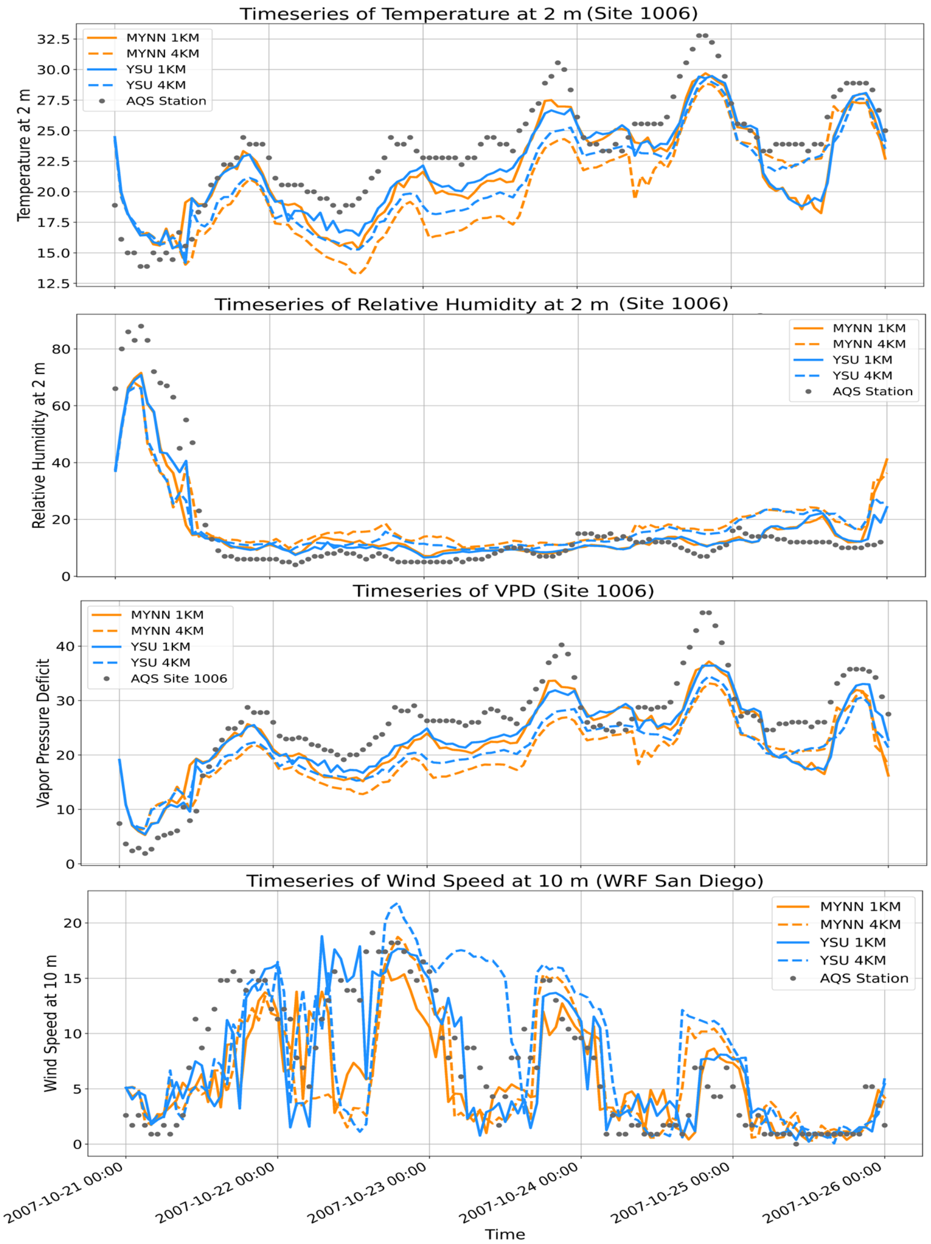

Figure 4.4: Timeseries for T2, Rh2, VPD, and Wspd10 for stations closer to the 2007 Witch Fire. The results are compared from 1 km and 4 km using YSU and MYNN PBL schemes with observations in order to show (a) T2 at site 1006;(b) Rh2 at site 1006;(c) VPD at site 1006;(d) Wspd10 at site 6001 in the respective panels.

Time-series of Fluxes

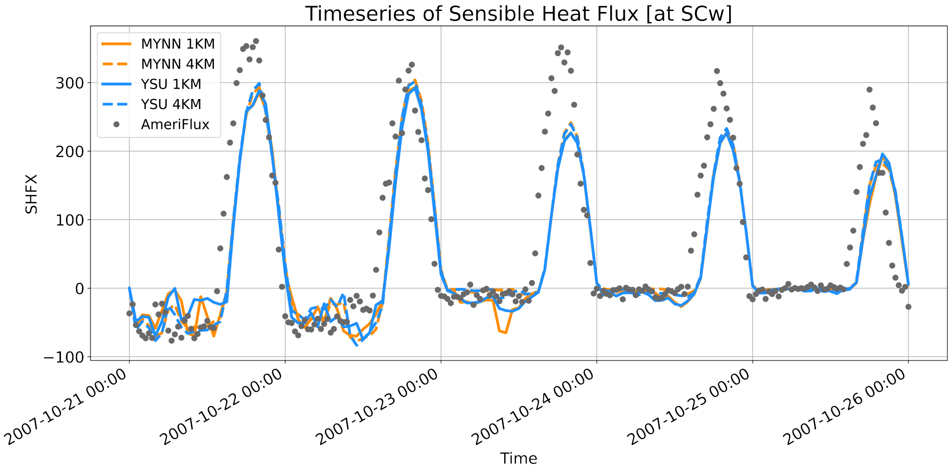

Figure 4.5: Timeseries of sensible heat flux [Wm^{-2}] at SCw site (Southern California Climate Gradient - Pinyon/Juniper Woodland) from AmeriFlux tower and model simulation as shown in Table 4.1. This site has Latitude and Longitude value of 33.6047 N, 116.4527 W and the elevation is 1,281 m.

The accurate representation of surface sensible heat flux is highly required for capturing fire-weather and fire atmosphere interaction (Thapa et al. [2022]). In this study we use the parameterized sensible heat flux from the model, represented as SHFX (the sub-grid scale heat flux is ignored). Also, we compare these modeled SHFX against the sensible heat flux reported by an AmeriFlux flux tower observatory nearest to the Witch Fire perimeter. The site has an elevation of 1,281 m with Latitude and Longitude of 33.6047 N and -116.4527 W respectively. This site is referred as US-SCw: Southern California Climate Gradient - Pinyon/Juniper Woodland in the AmeriFlux tower data repository. This is only available flux tower which had data recorded during the Witch Fire event. Although the site was not affected by the fire area/perimeter, it was close to the Witch Fire region as shown in Figure 4.1.

It is observed that even without an active fire-weather interaction module switched on, the WRF model is able to capture the heat flux reasonably well as compared to the observations (Figure 4.4). However, the sensible heat flux is underestimated by WRF during the day time.

During the intense fire period (from 18th hr of 21st October to 0 hr of 23rd October), no significant difference in the sensible heat flux can be observed. While comparing four modeled experiments, we find that the temporal variation of heat fluxes are similar. Therefore each set of the combined PBL scheme and grid resolution that we use in this study would be effective in simulating sensible heat fluxes.

Time-series of PBL Heights

Since we test two different, widely used PBL schemes at two different grid resolutions of 1 km & 4 km, we investigate the PBL heights variations over the period of this study for all four experiments over three different sites. In addition, we also focus on the PBL heights when the Witch Fire was highly intense, i.e., 23rd October at 00:00 UTC (Figure 4.3). It is interesting to note that there is no major difference in the simulated PBL heights at site 1006 with MYNN at 1 km and 4 km grid resolutions. However, the YSU PBL scheme estimates a higher PBL heights during this period (top panel in Figure 4.6). The variation in the magnitude of PBL heights are negligible for MYNN at both 4 km and 1 km during intense fire period. Furthermore, we also find that, during the period when fire was intense, from 18th hr of 21st October to 0 hr of 23rd October, variation in the PBL heights at SCw and at 6001 is much higher with the simulations at 4 km grid resolution than at 1 km (middle and bottom panel in Figure 4.6).

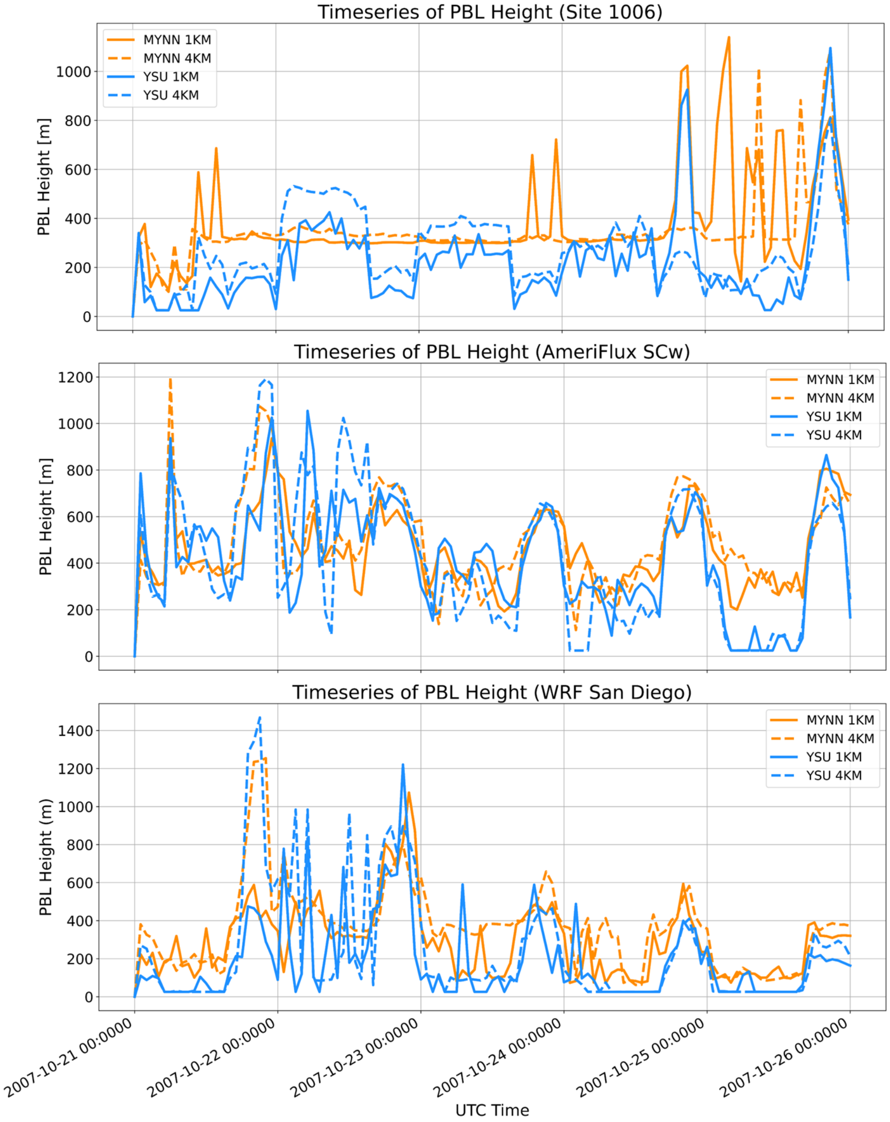

Figure 4.6: Timeseries plots for PBL heights for stations closer to the 2007 Witch Fire. The results are compared with 1 km and 4 km using YSU and MYNN PBL schemes to show (a) PBL at site 1006;(b) PBL at site called SCw (AmeriFlux);(c) PBL at site 6001 (San Diego) in the respective panels. These results are not compared with the observational data due the data unavailability at those sites.

4.3.3 Wind Conditions

Surface wind conditions

In this section, we compare the 10 m wind speed and wind direction from all simulations at 12:00 UTC on October 22, 2007, i.e., during the period when the Witch Fire was highly intense. We find that the WRF model is able to simulate the direction of easterly winds, i.e., the surface wind flow for Santa Ana winds (Figure 4.7(a, b, c, and d)). This is captured significantly well in all experiments regardless of the choice of PBL parameterization and horizontal grid resolution.

The wind speed at 10 m has a higher magnitude over the ocean as well to the south of the San Diego coast and further down in the ocean (Figure 4.7(a, b, c, and d)). The magnitude is higher for YSU at 4 km (Figure 4.7(d)) as compared to the other cases (Figure 4.7(a, b, and c)). Such higher magnitude of wind over ocean is present because of the influence of intensified upper level wind conditions as described in section 4.3.3.

Spatial variation of wind speed is analyzed in section 4.3.1 and we find that the wind speed is predicted better at 1 km resolution due to better representation of topography in the model. By comparing wind directions with wind arrows in Figure 4.7(a, b, c, and d), we observe that the arrows appear to be similar in direction and length for MYNN and PBL at 1 km and MYNN and YSU at 4 km. In addition, the model at 1 km generates higher wind speed as shown with the length of arrow over San Diego in Figure 4.7(a, b) when compared with Figure 4.7(c, d). Thus, the choice of horizontal grid has an impact on the wind direction and wind speed and the model performs reasonably well as a finer grid resolution.

Upper level or 850 MB wind conditions

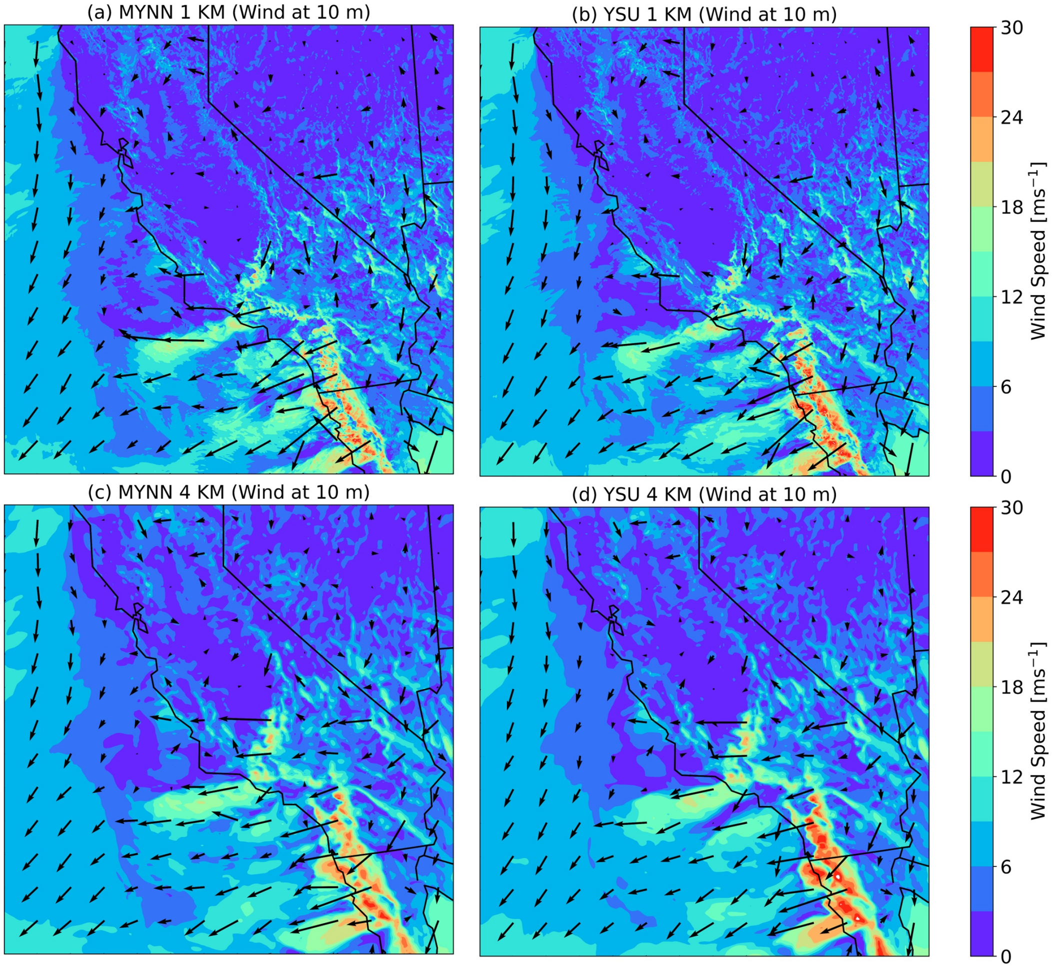

Figure 4.7: Wind speed (ms^{-1}) and wind direction at 10 m for (a) MYNN 1 km; (b) YSU 1 km; (c) MYNN 4 km; (d) YSU 4 km as shown in Table 4.1. These plots are shown at 00 Z UTC (5 p.m. Pacific time) on October 21st 2007, when the fire is intense. The panels from (a) to (d) represent the entire innermost domain (d03) as shown in Figure 4.1.

Observing the upper level wind conditions at 850 MB, (shown in Figure 4.8) we find that there is a presence of higher magnitude wind speed due to synoptic conditions. It is also evident that these synoptic wind conditions drive the surface wind which ultimately fanned the 2007 Witch Fire.

We do not find any significant difference in the results of four simulations as shown in Figure 4.8(a, b, c, and d). However, there are slight variations in the wind speed magnitude among the four set of simulations. In conclusion, it could be stated that the model is able to resolve the synoptic wind conditions that impact surface SA winds which fanned this Mega fire.

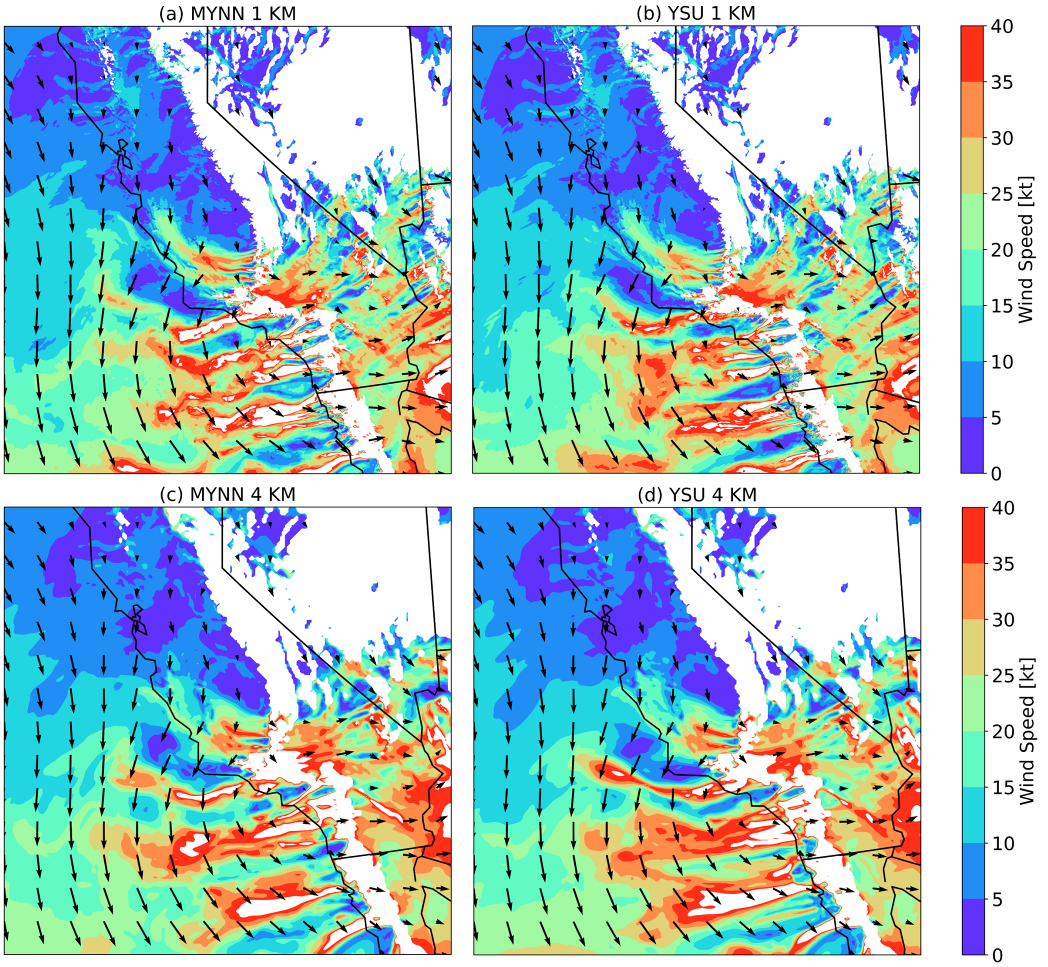

Figure 4.8: Wind speed (knot) and wind direction at 850 MB for (a) MYNN 1 km; (b) YSU 1 km; (c) MYNN 4 km; (d) YSU 4 km as shown in Table 4.1. These plots are shown at 00 Z UTC (5 p.m. Pacific time) on October 21st 2007, when the fire is intense. The panels from (a) to (d) represent the entire innermost domain (d03) as shown in Figure 4.1.

Vertical cross-section of wind speed and W component of wind

In this section, we analyze the vertical cross section of wind speed and the vertical W component of wind speed. Since from our analysis in the previous sections, it was determined that the wind speed is resolved well at the finer horizontal grid resolution, we present the vertical cross-section of wind speed from the MYNN PBL scheme only at 1 km as shown in Figure 4.9. In addition, this vertical cross section is drawn at the latitudinal value of 32.84 N which crosses the 2007 Witch Fire perimeter. The longitude varies from 120 W to 114.5 W to demonstrate the variation of wind speed across heights from land to ocean (Figure 4.9). The wind speed (Figure 4.9b) and vertical component of wind (W) (Figure 4.9a) both have a higher magnitude on the leeward side of the mountain range, which is a characteristics of the Santa Ana wind events. In addition, a strong updraft is observed on the windward side of the mountain, as well as a strong downdraft on the leeward side. This area of higher wind speed coincides with the perimeter of the Witch Fire burned area (Lat: 32.87 N to 32.88 N and Lon: 117.40 W to 115.67 W). Since the Figure 4.9 is shown at the instant when the fire was intense, we observe that the wind conditions are favorable for the intensification and a higher rate of spread for the Witch fire.

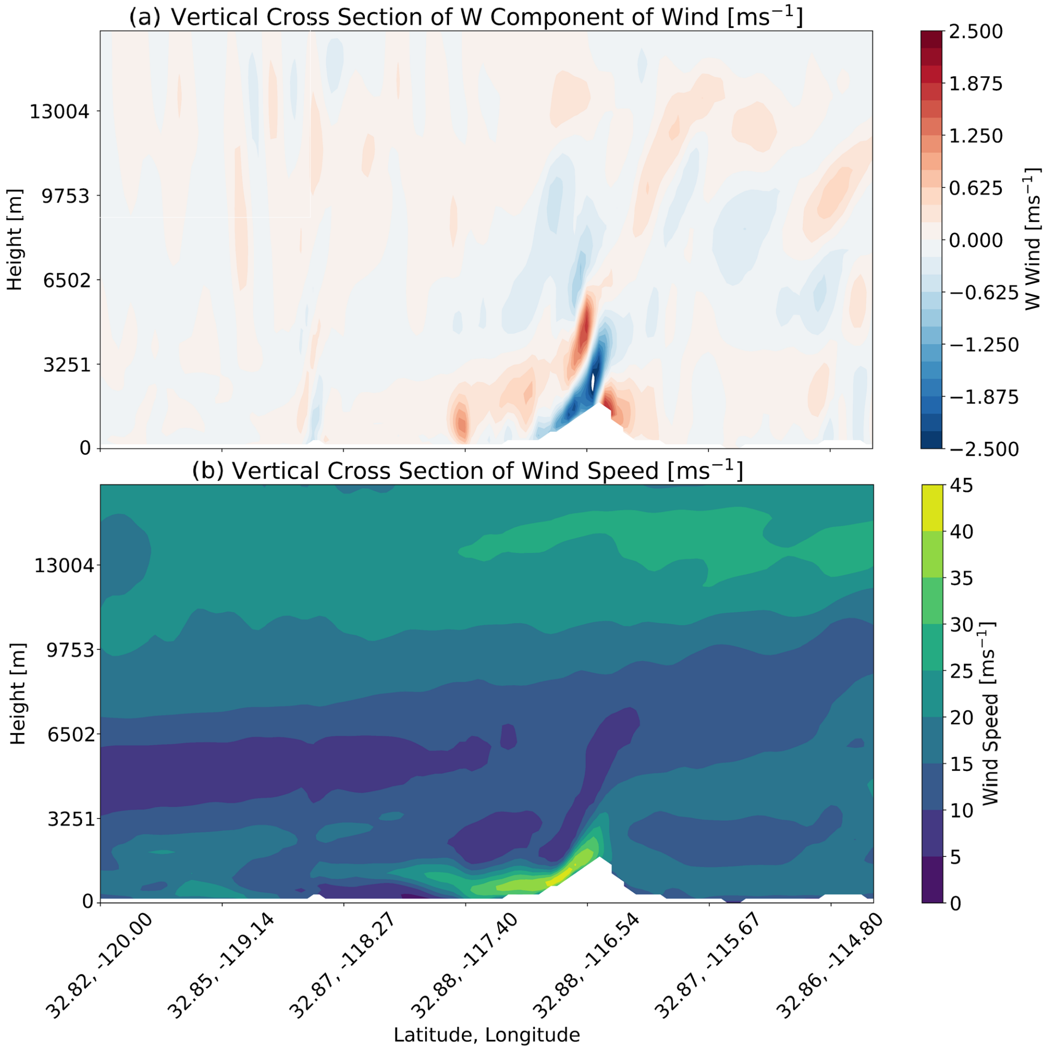

Figure 4.9: Vertical cross section of (a) W component of wind (ms^{-1}); (b) wind speed (ms^{-1}) from MYNN at 1 km at 00 Z UTC (5 p.m. Pacific time) on October 21st 2007, when the fire is intense. In addition, this vertical cross section is drawn at the latitudinal value of 32.84 N which crosses the 2007 Witch Fire perimeter and longitudes from 120 W to 114.5 W.

4.4 Conclusions

This study investigated the 2007 Witch Fire event using two different and widely used PBL schemes, YSU and MYNN. In addition, we performed a sensitivity experiment with two different horizontal resolutions at 1 km and 4 km. The goal was to test the capability of the WRF model in simulating fire-weather and related conditions with different grid sizes and PBL schemes combinations. We found that the model was able to capture fire-weather associated with the fire event with a reasonable accuracy close to the surface. On the other hand, the spatial and temporal variability of different meteorological parameters in the model was significantly dependent on the grid resolutions and the choice of PBL schemes. In summary, results from this study with 4 simulations suggested that the model's ability to predict near surface meteorological conditions was improved for finer grid resolution simulations than coarser resolution simulations. The results also indicted that wind is difficult to capture even at a finer resolution of 1 km than compared to temperature and relative humidity. Furthermore, the performance of the MYNN scheme is found to be generally better than the YSU scheme.

In general, the WRF model is not highly sensitive to the presence of the wildfire. This is because the weather model doesn't account for fire-atmosphere interaction. Another reason is that the grid resolutions is quite coarse, especially for the wind to be resolved well near complex topography.

It is evident that the WRF model coupled with an active fire-atmosphere interaction component would have higher capability of resolving wildfire events. However, such models are also computationally prohibitive and require resolutions close to 10 m to be run in a coupled large eddy simulation mode. Therefore the results of this study can be used to test the limits of the simple WRF model configuration to capture the effects of wildfire events. These results can provide the baseline over which the performance of more complex coupled

WRF-fire models can be tested.

Chapter 5

Impact of momentum perturbation on convective boundary layer turbulence

5.1 Introduction

Grid nesting for mesoscale-to-large-eddy simulation (LES) is a useful technique for a variety of atmospheric model applications, from wind energy to wildfire spread investigations [Haupt et al., 2020, 2019a,b, Mazzaro et al., 2019, Mirocha et al., 2014, Ching et al., 2014]. In LES, realistic atmospheric turbulence emerges as a result of wind shear and buoyant forcing. However, realistic turbulence can require long time scales to develop. Turbulence generation methods can accelerate the generation of turbulence in the LES domain, effectively reducing the distance it takes for turbulent motions to develop, known as fetch. A common approach is to use a periodic domain where wind through the outflow boundary is recycled through the inflow boundary, retaining memory of the flow characteristics. However, periodic simulations are limited in their ability to represent heterogeneous surfaces, or flow around obstacles. For these applications, a boundary-coupled simulation with an inflow and outflow are required.

In boundary-coupled simulations using inflow data that does not contain resolved turbulence at the time and space scales of the LES discretization (e.g. from a mesoscale simulation), the development of resolved-scale turbulence generally requires a long fetch. Therefore, a large LES domain is needed to capture the development of turbulence at fine scales, increasing computational cost [Mirocha et al., 2010, 2014, Connolly et al., 2021, Muñoz-Esparza et al., 2014, Mazzaro et al., 2017, 2019]. One way to reduce the fetch is to run a precursor LES using periodic lateral boundary conditions with the same time and space discretization as the target LES, and use the solution as inflow. However, the precursor simulation can require significant additional computational overhead, while also requiring forcing and surface conditions amenable to periodicity.

To overcome these challenges, a class of methods exist to initialize inflow boundary conditions with turbulence. For example, synthetic turbulence methods [Le et al., 1997, Pamiès et al., 2009] use digital filtering techniques of flow to infer Reynolds Stresses [Di Mare et al., 2006, Klein et al., 2003, Xie and Castro, 2008]. These techniques require some information about the turbulence, either from observations or a periodic simulation. These methods also require relatively long fetches for the generation of turbulence. Another technique is the forcing method [Spille-Kohoff and Kaltenbach, 2001, Zajaczkowski et al., 2011, Keat et al., 2004], which uses wall-normal forces to move the flow into the domain inlet and generate the necessary Reynolds shear stress. However, it also needs a *priori* information about the targeted level of turbulence. Additional simulations are needed for generating an adequate amount of turbulence from this method in order to get a value that is closer to the observation.

As a compromise to using a turbulent inflow condition, another approach is to seed the inflow characteristics with added perturbations and allow the flow to develop realistic turbulence over a reduced fetch. One such method, the cell perturbation Method (CPM) [Muñoz-Esparza et al., 2014, 2015, Muñoz-Esparza and Kosović, 2018], is a turbulence generation technique that employs random perturbations to potential temperature to induce small-scale motions near nested domain inflow boundaries. Mazzaro et al. [2019] modified the CPM approach by applying forces to the momentum in the horizontal and vertical directions rather than perturbing the potential temperature fields. Mirocha et al. [2014] applied tendencies with sinusoidal amplitudes to temperature and velocity fields near inflow boundaries. This perturbation method produced promising results with the target turbulence level by triggering turbulent motions near the nested domain inflow boundaries. Muñoz-Esparza et al. [2014, 2015], and Muñoz-Esparza and Kosović [2018] advanced this method by adding random forces instead of using sinusoidal perturbations, and also introduced perturbation cells. Perturbation cells are a span of contiguous model grid points located adjacent to the LES inflow boundaries that are perturbed with the same random value. A configuration of three cells consisting of eight grid points per cell in each of the horizontal directions is found to be optimal [Muñoz-Esparza et al., 2014]. In addition, Muñoz-Esparza and Kosović [2018] optimized the CPM for different stability conditions. Thermal perturbations are chosen to encourage the most rapid formation of realistic correlations associated with buoyancy forces generated by the patches of resolved temperature variability. Although this optimization reduces the fetch size considerably relative to simulations using no perturbations, a nontrivial fetch still remains.

To further reduce the fetch required for turbulence generation, Mazzaro et al. [2019] applied tendencies directly to the momentum components, rather than potential temperature. This study showed that simulations perturbations were applied to the vertical momentum term produced the shortest fetches overall, thereby further reducing fetch requirements and associated computational costs. However, the consequence of introducing momentum perturbations at the domain boundary on the fate and transport of turbulence in the domain is not yet well understood [Mazzaro et al., 2019]. Quantifying the TKE budget in the WRF-LES domain can shed light on this question. In this study, we examine how momentum perturbations shift the balance between the terms of the TKE budget during a diurnal cycle in the convective atmospheric boundary layer (CBL). We apply random (stochastically selected from within an amplitude range of 1,000 kgs^{-4} to 10,000 kgs^{-4}) forces in both vertical and horizontal directions and vary the vertical extent of the perturbations from 307 m (halfway between the surface and boundary layer and 1,608 m (top of the domain). TKE budget terms, including buoyant production, shear production, turbulent transport, and pressure correlation are then compared between simulations including these different perturbation configurations, periodic simulations and simulations not including perturbations.

The goals of this study are as follows: (1) to explore the impact of a simple and computationally efficient Stochastic Cell Perturbation method (SCPM) to accelerate the generation of turbulence; (2) to understand how momentum perturbations shift the balance between the terms of the TKE budget; (3) to evaluate the role of momentum perturbation amplitudes on the TKE budget; and (4) to examine the effect of height in a convective boundary layer at which momentum perturbations are applied. We use the Weather Research and Forecasting (WRF) LES model to simulate the convective boundary layer. Our results will advance the understanding of optimal strategies for performing coupled mesoscale-microscale simulations of atmospheric boundary layer processes.

This study is organized into three main sections. The methods and experimental set-up that are used to perform the SCPM using momentum perturbations (SCPM-M) are presented in section 2. Section 3 describes the results and discussion of our analysis. Conclusions are presented in section 4.

5.2 Methods

5.2.1 Model Configuration

In this study, we examine the impacts of applying SCPM-M in a convective (unstable) atmospheric boundary layer on the TKE budget. We use the WRF model version 4.1.3 [Skamarock et al., 2019] to conduct idealized LES simulations of a convective boundary layer based on measurements at the Scaled Wind Farm Technology (SWiFT) facility located in West Texas, USA. Simulations are initialized using data from 14 Z to 20 Z UTC (8 a.m. to 2 p.m. Central time) on November 8th, 2013, allowing 4 hours for model spin-up and 2 hours for perturbed simulation. The SCPM-M is applied in the LES domain from 18 Z to 20 Z UTC (12 noon to 2 p.m. Central time). In this study, WRF-LES is used with a horizontal grid resolution of 12 m and is one-way nested within an idealized mesoscale domain with a horizontal grid resolution of 240 m. The mesoscale domain (d01) has a horizontal extent of 115 km by 115 km, with 480 grid cells in both X and Y directions, while the LES domain (d02) has 961 grid cells in X direction and 481 grids in Y for a domain size of 11.5 km by 5.7 km. We use 88 vertical eta levels with the top level at 1,608 m (ztop). An input sounding is used from the SWiFT facility with a capping inversion at approximately 600 m. The time step for integration is five seconds and the outputs for the LES domain are stored at every minute. Overall we perform nine WRF-LES simulations. Seven WRF-LES simulations are performed using various permutations of perturbation height and magnitude. In addition, we also perform one simulation with no inflow perturbations (referred as No-SCPM) and another simulation with periodic boundary conditions (referred as periodic) for context. By using periodic boundary conditions, it is implicitly assumed that both the atmospheric fields and the underlying land usage have repeating periodic characteristics [Mirocha et al., 2014, Zhong et al., 2021]. These simulations are summarized in Table 5.1 and described in more detail in section 5.2.2.

We use the YSU [Hong et al., 2006] PBL scheme for the mesoscale domain. We do not use cloud microphysics, land surface, cumulus physics, or radiation physics in this study. We use the nonlinear backscatter and anisotropy (NBA) scheme [Kosović, 1997, Mirocha et al., 2010] to model subgrid scale (SGS) mixing in the LES and mesoscale domain respectively. In the LES sub-domain, Monin-Obukhov similarity theory is used to parameterize the surface layer (surface layer option 1 [Jiménez et al., 2012, Monin and Obukhov, 1954]).

Label	**Amplitude** F_{xy} (kgs^{-4})	**Amplitude** F_z (kgs^{-4})	**Ktop** (value)	**Height** (meters)
No-SCPM	–	–	–	–
Periodic	–	–	–	–
Ktop34L	1,000	1,500	34	307
Ktop54L	1,000	1,500	54	609
Ktop88L	1,000	1,500	88	1607
Ktop88M	2,000	4,000	88	1607
Ktop34H	5,000	10,000	34	307
Ktop54H	5,000	10,000	54	609
Ktop88H	5,000	10,000	88	1607

Table 5.1: The table shows a list of simulations performed in this study using different Ktop values as well as the maximum amplitude of perturbations in both horizontal and vertical direction. It also shows the periodic and No-SCPM simulations that are used to compare the results of the SCPM-M cases.

5.2.2 Experimental set-up

Periodic and No-SCPM Simulations

SCPM Simulations

In this study, we apply momentum perturbations to 8 x 8 x 1 grid point cells from the surface up to the 34th, 54th, and 88th pressure level along the inflow boundary of the LES domain (denoted as Ktop34, Ktop54, and Ktop88 respectively). The vertical extent of these perturbations is 307 m, 609 m, and 1,607 m, respectively. These extents correspond to heights halfway between the surface and the capping boundary layer, the height of the capping boundary layer, and the top of the domain. We also vary the perturbation amplitude. Simulations with low amplitude perturbations ($F_{xy} = 1000$ kgs^{-4}; $F_z = 1500$ kgs^{-4}) are denoted as Ktop34L, Ktop54L, and Ktop88L), and simulations with high amplitude perturbations ($F_{xy} = 5000$ kgs^{-4}; $F_z = 10000$ kgs^{-4}) as Ktop34H, Ktop54H, and Ktop88H (Table 5.1). For medium amplitude perturbations ($F_{xy} = 2000$ kgs^{-4}; $F_z = 3000$ kgs^{-4}), we only perform a simulation for the Ktop88 case as mentioned in Table 5.1, denoted as Ktop88M. Only this case is selected for the medium amplitude perturbations as the vertical extent (from Ktop22, 150 m to Ktop88, 1,607 m) of added perturbations is higher than the other two cases, i.e., Ktop54 (from Ktop22, 150 m to Ktop54, 609 m) and Ktop34 (from Ktop22, 150 m to Ktop88, 307 m).

5.2.3 Analysis Methods

In order to calculate mean and turbulent statistics, we use standard turbulence decomposition, where $u' = U - \overline{U}$, $v' = V - \overline{V}$, $w' = W - \overline{W}$, and $\theta' = \theta - \overline{\theta}$ where $\overline{\theta}$. Here U, V, and W are the instantaneous velocity components, θ is the potential temperature, over-bars denote time averaging, and primes denote fluctuations from the mean. The wind speed is calculated as $\sqrt{\overline{U}^2 + \overline{V}^2}$ with an averaging time of the last 30 minutes of simulation i.e., from 19:30 Z to 20 Z UTC (1:30 p.m. to 2 p.m. Central time). The heat flux is given by $\overline{w'\theta'}$ and momentum flux is given by $\overline{w'u'}$.

The turbulent kinetic energy (TKE) budget equation is given by Stull [1988]:

$$\frac{\partial \overline{e}}{\partial t} + \bar{U}_j \frac{\partial \overline{e}}{\partial x_j} = \delta_{i3} \frac{g}{\overline{\theta_v}} \overline{u_i' \theta_v'} - \overline{u_i' u_j'} \frac{\partial \bar{U}_i}{\partial x_j} - \frac{\partial \overline{u_j' e}}{\partial x_j} - \frac{1}{\overline{\rho}} \frac{\partial \overline{u_i' p'}}{\partial x_i} - \epsilon \tag{5.1}$$

where, the first and second term on the left hand side (LHS) of equation 5.1 represent local storage or tendency of TKE and the advection of TKE by mean wind, respectively. The terms on the right hand side (RHS) of equation 5.1 in order from left to right represent the buoyant production or consumption term, a mechanical or shear production term, the turbulent transport of TKE, a pressure correlation term, and the viscous dissipation of TKE, respectively (Stull [1988]). The $\overline{e}$ is the TKE, defined as:

$$\overline{e} = 0.5(\overline{u'u'} + \overline{v'v'} + \overline{w'w'}) \tag{5.2}$$

The TKE budget equation after assuming horizontal homogeneity, neglecting subsidence, and choosing a coordinate system that is in the direction of mean wind, is simplified as:

$$\frac{\partial \overline{e}}{\partial t} = +\frac{g}{\overline{\theta_v}} \overline{w' \theta_v'} - \overline{u'w'} \frac{\partial \bar{U}}{\partial z} - \frac{\partial \overline{w'e}}{\partial z} - \frac{1}{\overline{\rho}} \frac{\partial \overline{w'p'}}{\partial z} - \epsilon \tag{5.3}$$

Using these concepts and equations, we compute TKE, heat and momentum fluxes, as well as TKE budget terms associated with buoyancy, shear, transport, and pressure correlation for all simulations outlined in Table 5.1. In the next section, we present and discuss results of this analysis.

5.3 Results and Discussion

5.3.1 Turbulent kinetic energy (TKE)

Spatial variation of TKE

TKE is a measure of turbulence intensity. We calculate TKE for all simulations (Table 5.1), and compare its variation over height (z) and streamwise distance (x) (Figure 5.1). The distance from inflow boundary at which turbulent fluctuations starts to develop is called fetch [Mazzaro et al., 2017, 2019]. We observe that for simulations without momentum perturbation (No-SCPM), turbulence begins to develop 5,000 m into the domain, with a significant fetch, and realistic representation of turbulent structures only appears in the last 25% of the domain. After applying SCPM-M, the fetch is reduced significantly for all perturbed cases.

For high amplitude perturbations (Figure 5.1(b-d)), the fetch is diminished, but the maximum of TKE is present along the inflow boundary, and near the boundary layer top. For Ktop54H and Ktop88H, positive values of TKE extend above the boundary layer, an artifact related to the high perturbation height and amplitude (Figure 5.1(c) and Figure 5.1(d)). Furthermore, for Ktop34H, the TKE maximum is present near the bottom of the domain, near the surface and most importantly, the fetch has reduced significantly (Figure 5.1(b)).

In the case of lower and medium amplitude perturbations (Figure 5.1(e-h)), the TKE maxima near the boundary layer are not present. We also observe that the rate at which the TKE increases with the downwind x direction is similar for the medium and lower amplitude perturbations but not the same as the No-SCPM case (Figure 5.1a).

These spatial patterns highlight that the vertical and horizontal extent of inflow perturbations can influence the underlying turbulence evolution. Moreover, SCPM-M produces a vertical profile of TKE that spans the boundary layer more rapidly than without the perturbations. In addition, tuning the amplitude of the perturbation helps minimize the fetch to fully develop the TKE. However, if the height of perturbations approaches or exceeds the boundary layer, this leads to artifacts in the flow field above the boundary layer height.

Fetch

In boundary-coupled simulations using inflow data that does not contain resolved turbulence at the time and space scales of the LES discretization (e.g. from a mesoscale simulation), the development of resolved-scale turbulence generally requires a long fetch. We compare the variation of the TKE in the x direction (at two heights, $10\,\mathrm{m}$ and $53\,\mathrm{m}$, Figure 5.2) from the perturbed cases and the periodic simulation to investigate the extent of the fetch. The distance from the inflow boundary at which the TKE from the SCPM-M simulations becomes comparable to the TKE obtained from the periodic simulation can be used a rough estimator for the fetch.

We observe that the fetch is longest for the No-SCPM simulation (Figure 5.2). At $10\,\mathrm{m}$ height, the fetch for the No-SCPM case is around $9{,}000\,\mathrm{m}$ and at $53\,\mathrm{m}$ the fetch is around $7{,}200\,\mathrm{m}$ (Figures 5.2(a-d)). Before the fetch is fully established, the TKE increases to an unrealistically high level as indicated by the large departure from the periodic case.

However, after applying SCPM-M, the fetch is reduced significantly. At both $10\,\mathrm{m}$ and $53\,\mathrm{m}$, the TKE is fully developed around $2{,}000\,\mathrm{m}$ for all perturbed cases as shown in Figure 5.2. At the last quarter of the domain, starting at $x = 9,600\,\mathrm{m}$, the TKE for the perturbed cases are quite close to the periodic case. Therefore, we will use the last three quarters of the domain (x from $2{,}880\,\mathrm{m}$ to $11{,}520\,\mathrm{m}$) to average over turbulence statistics subsequently reported in this study. The TKE profiles averaged over the last quarter of the domain (x from $86{,}400\,\mathrm{m}$

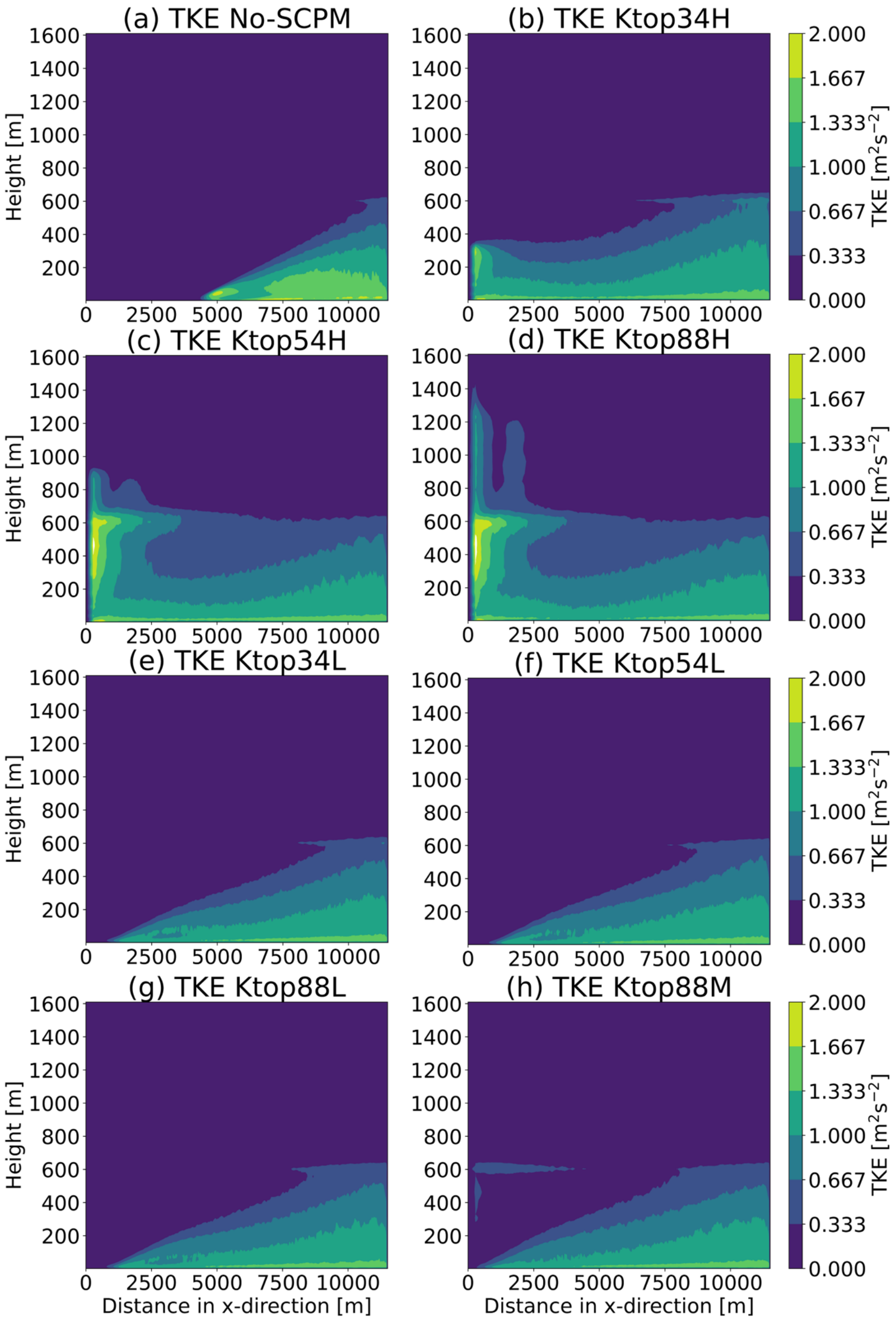

Figure 5.1: Y-averaged TKE (m^2/s^2), computed over the entire inner domain, compared between simulations with and without momentum perturbation with different perturbation amplitudes and vertical extents with panels (a) No-SCPM, (b) Ktop34H, (c) Ktop54H, (d) Ktop88H, (e) Ktop34L, (f) Ktop54L, (g) Ktop88L, and (h) Ktop88M as shown in Table 5.1.

to 11,520 m) will be reported only for reference in section 5.3.1.

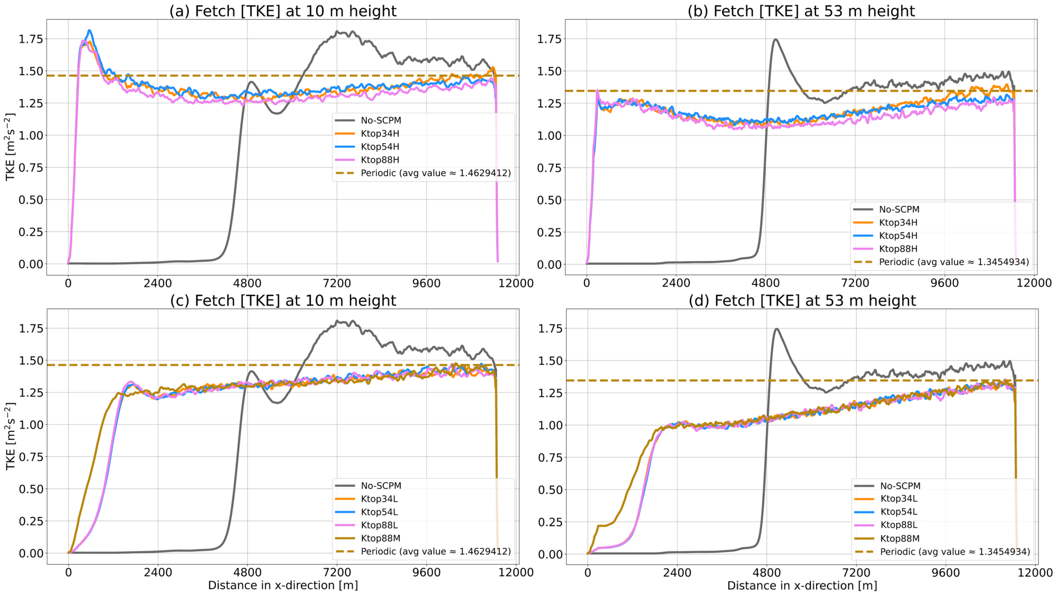

Figure 5.2: Fetch of Y-averaged TKE (m^2/s^2), computed after applying momentum perturbation with higher, medium, and lower amplitudes as shown in (Table 5.1) and show fetch at (a) 10 m height for periodic, No-SCPM, and higher amplitude SCPM-M, (b) 53 m height for periodic, No-SCPM, and higher amplitude SCPM-M, (c) 10 m height for periodic, No-SCPM, and lower and medium amplitude SCPM-M, (d) 53 m height for periodic, No-SCPM, and lower and medium amplitude SCPM-M. These plots are generated for TKE that are Y-averaged over the entire inner domain.

TKE profiles

Based on the discussion in the previous section 5.3.1, we compare the TKE profiles that are averaged over two different areas: three quarters of the domain (over all y and x from 2,880 m to 11,520 m) farthest away from the inflow (Figures 5.3 (a-b)), and last quarter of the domain (over all y and x from 86,400 m to 11,520 m) farthest from the inflow (Figures 5.3 (c-d)). We observe that applying SCPM-M produces TKE closer to the periodic case regardless of the extent of its application (Figures 5.3(a-d)).

As it is observed in Figure 5.3, the TKE is highest near the surface, and decreases with height in all SCPM-M simulations and as well as in the case of No-SCPM. Up to 200 m, the

TKE is similar for all the perturbed cases as well as the periodic case, while the TKE for the No-SCPM case is lower, when the TKE is area averaged over the last three quarters of the domain (Figures 5.3(a-b)). However, between 300 m and up to the CBL height, SCPM-M cases with higher amplitudes are closer to the periodic case; while No-SCPM shows the largest deviation from the periodic case (Figures 5.3(a-b)). When the last quarter area averaged profiles are compared (Figures 5.3(c-d)), we find that the TKE is highest for No-SCPM case below 300 m and it decreases sharply above 300 m, deviating the most from the periodic case. However, the SCPM-M cases are closer to the periodic case for all heights. In addition, we also observe that the medium and lower amplitude SCPM-M cases are almost equal in the magnitude throughout the domain (Figure 5.3(d)). From the high amplitude SCPM-M cases, the TKE for the Ktop34H is closest to the periodic case above 300 m (Figure 5.3(c)). It is important to note that the effect of momentum perturbation is not only to enhance TKE but rather to adjust TKE closer to the appropriate levels at all heights within the CBL.

5.3.2 Mean and instantaneous flow features

Instantaneous flow features

Figure 5.4 shows the instantaneous U component of velocity at two-third and half of the CBL height (211 m and 391 m, respectively) for simulations without SCPM and the SCPM applied to three different vertical extents. These velocities are shown at the last instant of the simulation period i.e., at 20 Z (i.e., 20 Z UTC) for the nested LES domain. As observed in Figures 5.1,5.2, and 5.3, and in previous studies, such as Mazzaro et al. [2017, 2019], a large fetch is required for the no-SCPM simulation. The fetch is reduced significantly whenever perturbations are applied, regardless of the extent and amplitude of the applied momentum perturbation.

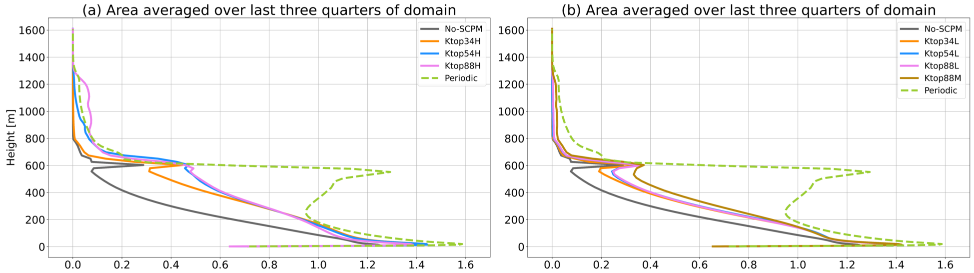
(a) Area averaged over last three quarters of domain

(b) Area averaged over last three quarters of domain

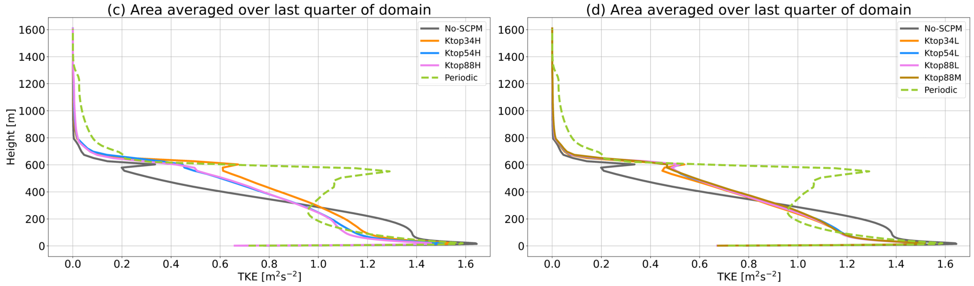
(c) Area averaged over last quarter of domain

(d) Area averaged over last quarter of domain

Figure 5.3: Area-averaged TKE (m^2/s^2) profiles, computed for the inner domain after applying momentum perturbation with higher amplitude (Table 5.1) in the right panels and lower & medium amplitudes (Table 5.1) in the left panels, respectively. Profiles (a) and (b) show TKE values that are area averaged over the last three quarters of the domain, i.e., over all y and x from 2,880 m to 11,520 m for (a) Periodic, No-SCPM, and high amplitude SCPM-M (Ktop34H, Ktop54H, and Ktop88H); (b) Periodic, No-SCPM, and low and medium amplitude SCPM-M (Ktop34L, Ktop54L, Ktop88L, and Ktop88M). While, panels (c) Periodic, No-SCPM, and high amplitude SCPM-M (Ktop34H, Ktop54H, and Ktop88H), and (d) Periodic, No-SCPM, and low and medium amplitude SCPM-M (Ktop34L, Ktop54L, Ktop88L, and Ktop88M) are the TKE profiles that are area averaged over only the last quarter of the domain, i.e., over all y and x from 86,400 m to 11,520 m.

Mean wind speed profiles

We find that the time and area averaged (over the last 30 minutes of simulation for the last three quarters of the domain) vertical profiles of the wind speed for the different simulation cases follow the expected logarithmic profile up to the CBL height of 600 m (Figure 5.5a). The extent and amplitude of inflow perturbations have little effect on the wind speed profiles. Between 100 m to 500 m, the wind speed for the No-SCPM case is higher as compared to the other perturbed cases. Between 100 m to 500 m, the lowest wind speed is observed for the Ktop88H case (purple line in Figure 5.5a), compared to the other cases. Wind speed profiles for the lower and medium SCPM-M cases are similar to each other but lower than the No-SCPM case up to about 500 m.

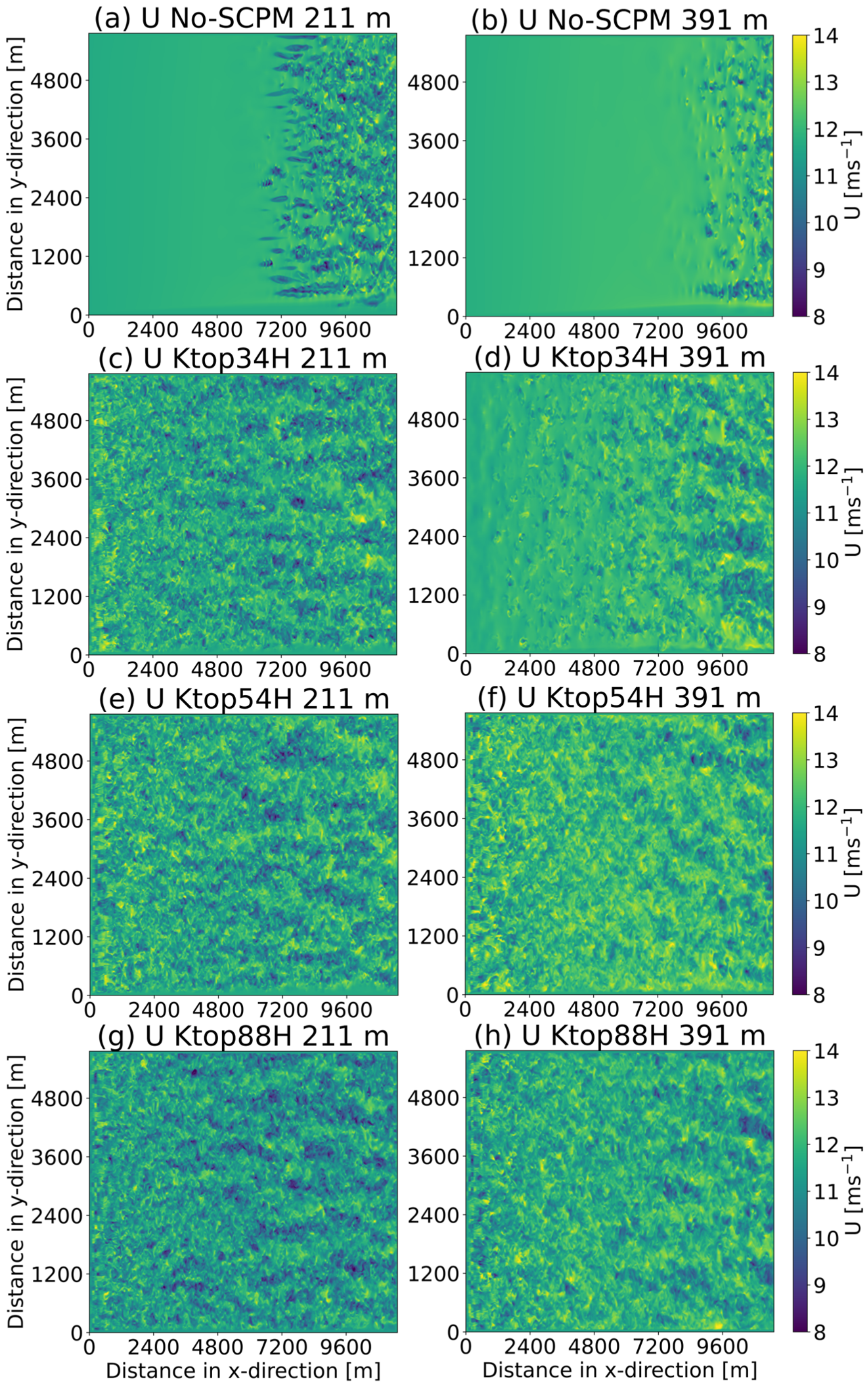

Figure 5.4: Instantaneous U component of velocities (ms^{-1}), computed at two different heights that is at half (level=27, z=211 m) and at two-third (level=37, z=391 m) of the boundary layer height for (a-b) No-SCPM, (c-d) Ktop54H (e-f) Ktop54H (g-h) Ktop88H. The color bar corresponds to the magnitude of velocity for panels (a) to (h). The domain shown is the inner LES domain used in this study.

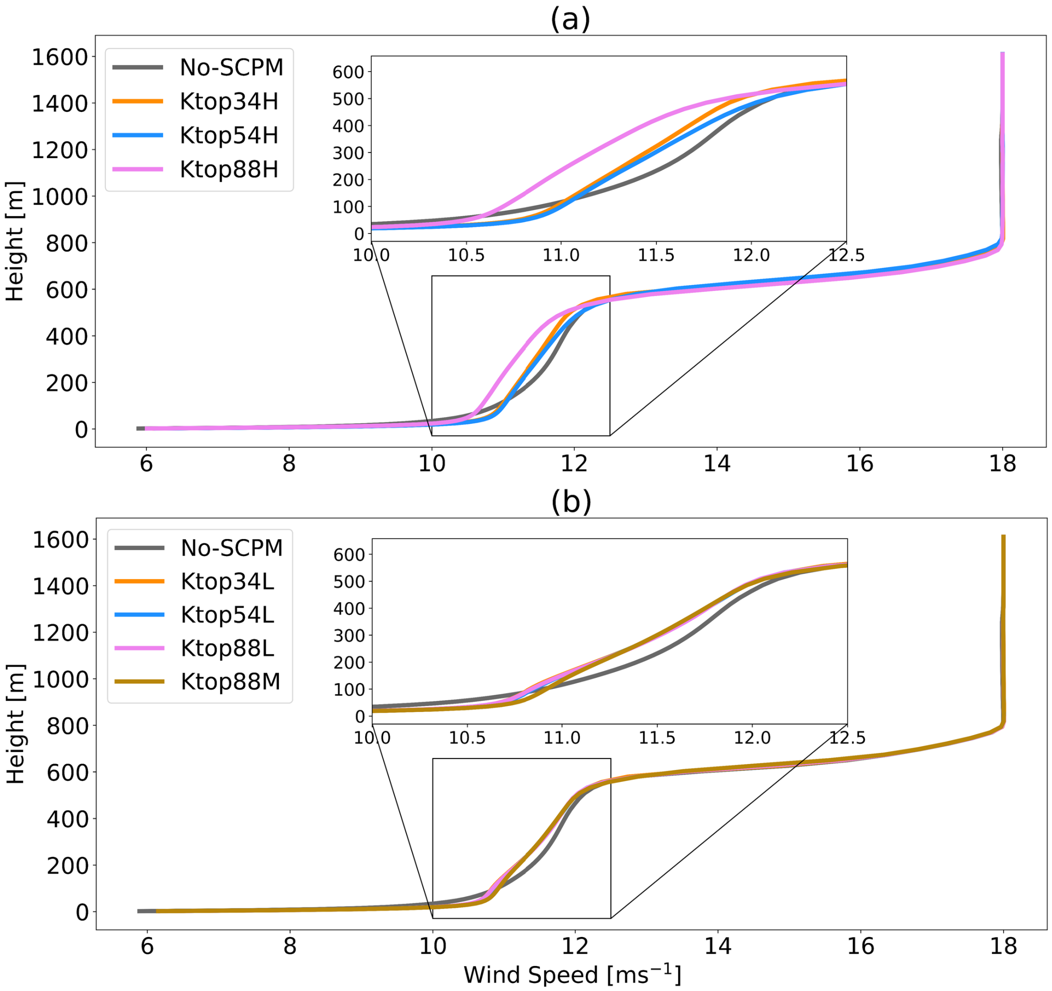

Figure 5.5: Wind speed (ms^{-1}) area averaged over three quarters of the domain (all y and x from 2,880 m to 11,520 m) for all the cases as shown in Table 5.1 for (a) higher, (b) lower and medium amplitude SCPM-M. The wind speeds are generated from the last 30 minutes of the simulation time period i.e., from 19 Z (UTC) to 20 Z (UTC) and for top of the entire simulation inner domain up to 1608 m.

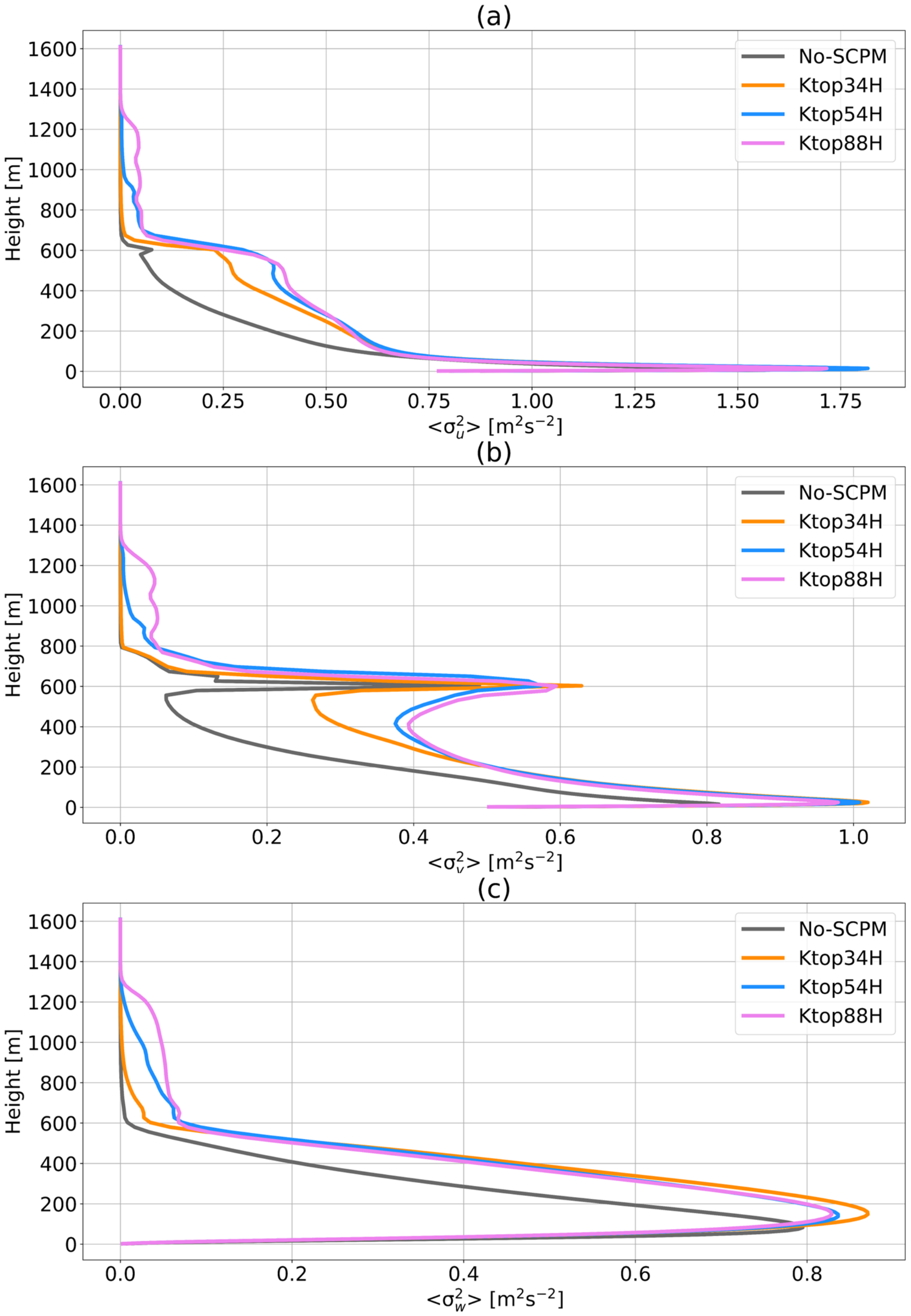

Figure 5.6: Area averaged (a) $< \sigma_u^2 >$, (b) $< \sigma_v^2 >$, and (c) $< \sigma_w^2 >$ over three quarters of the domain (all y and x from 2,880 m to 11,520 m) for No-SCPM, Ktop34H, Ktop54H, & Ktop88H. These results are shown from the last simulation period at 20 Z and for top of the entire simulation inner domain up to 1,608 m. The angular brackets denote area averaging.

Velocity variance statistics

In order to examine the contributions of the velocity variance components (σ_u^2, σ_v^2, σ_w^2) to the TKE, we area-average them over the last three quarters of the domain and compute in Figure 5.6. Similar to the TKE profiles in Figure 5.3, all three velocity variances are higher for the SCPM-M cases compared to the No-SCPM case. The σ_w^2 is higher for the Ktop34H case around 200 m. Just below the CBL height of 600 m, the σ_u^2 and σ_v^2 are higher for Ktop88H compared to the other cases.

5.3.3 Fluxes of sensible heat and momentum

Similar to the other turbulence statistics, the fluxes of sensible heat ($\overline{w'\theta'}$) and momentum ($\overline{u'w'}$) are averaged over the last three quarters of the domain and plotted in Figure 5.7. We observe that below 200 m, the fluxes of sensible heat and momentum are higher for the No-SCPM case as compared to the SCPM-M cases (Figure 5.7). This could be attributed to unrealistically high levels of TKE in the No-SCPM case in the last two quarters of the domain, as observed in Figure 5.2. Above 200 m, the sensible heat flux for the SCPM-M cases is similar to the No-SCPM case (Figure 5.7(a-b)). However, the momentum fluxes are higher for the SCPM-M cases than the No-SCPM (Figure 5.7(c-d)) case above 200 m.

Among the SCPM-M cases, the Ktop34H has a higher sensible heat flux than the other cases (Figure 5.7a). The lower and medium amplitude SCPM-M cases are similar in the sensible heat flux throughout the domain (Figure 5.7b). For the momentum flux, all high amplitude SCPM-M cases (Figure 5.7c) and all the low and medium amplitude cases (Figure 5.7d) are similar to each other.

At the top of the inversion layer, Ktop34H has the highest entrainment flux (this is where the 'potentially' warmer air is entrained into the CBL), as indicated by the strongly negative sensible heat flux at the top of the CBL for Ktop34H. Ktop88H and Ktop54H simulations produce similar entrainment fluxes of heat from above into the CBL. This is due to turbulence being artificially excited near and above the top of the CBL.

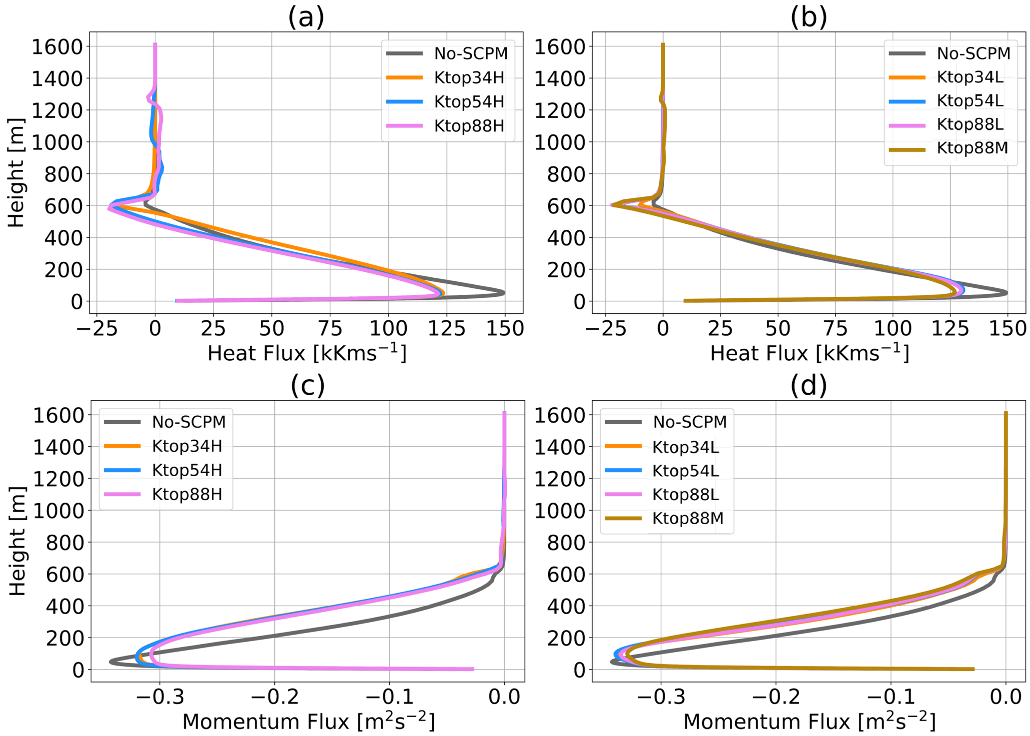

Figure 5.7: Heat flux ($\overline{w'\theta'}$) profiles after applying momentum perturbation (SCPM-M) with (a) higher amplitudes of forces, as shown in (Table 5.1), (b) lower & medium amplitudes of forces; momentum flux ($\overline{u'w'}$) with (c) higher amplitudes of forces, and (d) lower & medium amplitudes of forces. In addition, these profiles are computed in a way that the heat flux ($\overline{w'\theta'}$) and momentum flux ($\overline{u'w'}$) are area averaged over last three quarters of the inner domain i.e., over all y and x from 2,880 m to 11,520 m and are shown for top of the entire simulation inner domain up to 1608 m.

5.3.4 Turbulent kinetic energy budget

Since the sensible heat flux and momentum flux both contribute to TKE generating mechanisms, the components of the budget equation for the TKE are worth investigating for the different cases being simulated. Therefore, individual terms of the TKE budget are discussed in this section. Figure 5.8 shows the y-averaged components of the TKE budget for the No-SCPM (left column) and the Ktop34H case (right column). The y-averaged TKE budget terms for other SCPM-M cases are plotted in the supplementary material (Figure D.5). The three quarter domain averaged profiles of the TKE budget terms for all the SCPM -M cases as well as the No-SCPM case are plotted in Figure 5.9.

The Ktop34H is chosen to be shown in Figure 5.8 among the SCPM-M cases for the combination of satisfying two criteria. The additional entrainment at the capping inversion level is very low for the Ktop34H case compared to the other cases. Moreover, the reduction in fetch is significant. The other high amplitude cases, while reducing the fetch, generate additional entrainment at the CBL height, while the low amplitude and medium amplitude cases are less efficient in the fetch reduction.

Buoyancy Term

The y-averaged buoyancy term $(g/\overline{\theta})\overline{w'\theta'}$ for the No-SCPM and Ktop34H cases are plotted in Figure 5.8(a and b).

We observe that for the No-SCPM case, the buoyancy term starts developing from the center of the x axis (Figure 5.8a). However, the fetch for the buoyancy term is reduced significantly for the perturbed cases (Figure 5.8(b) and Figure D.5). For Ktop54H and Ktop88H, the fetch is reduced appreciably, however, additional entrainment can be observed near the CBL height (Figure D.5(a-b)). It can be generally observed that lower amplitude perturbations reduce the fetch and do not create additional entrainment. Another important point to note is that the application of momentum perturbation (SCPM-M) is sufficient to modify the buoyancy term, without requiring perturbing the temperature field, as demonstrated by Mazzaro et al. [2019]. This could be explained by the fact that the force-perturbation method generates additional w' fluctuations in the turbulent field, which excites the vertical sensible heat flux $\overline{w'\theta'}$ as well.

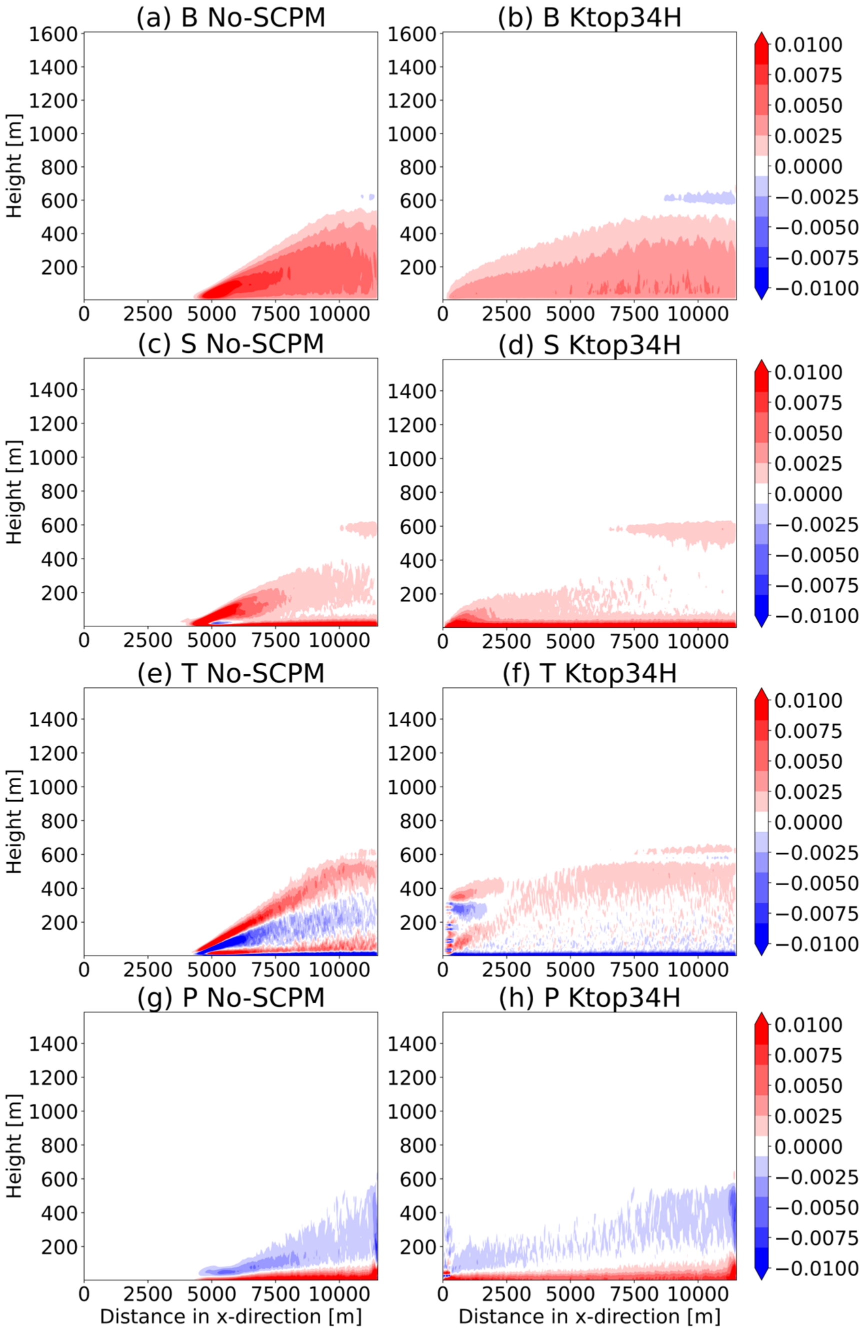

Figure 5.8: Y-averaged TKE budget terms after applying momentum perturbation following (Table 5.1), for the buoyancy term with (a) No-SCPM, (b) Ktop34H, for the shear production term with (c) No-SCPM (d) Ktop34H, for the turbulent transport with (e) No-SCPM (f) Ktop34H, and for the pressure correlation term with (g) No-SCPM, (h) Ktop34H. The color bar corresponds to the magnitude of TKE budget terms for panels (a) to (h). These plots are generated for TKE budget terms that are Y-averaged over the entire inner domain.

As observed in Figure 5.9(a-b), the vertical profile of the buoyancy term follows the same trend of the sensible heat flux profiles as shown in Figure 5.7(a-b).

Shear Term

The momentum flux $\overline{u'w'}$ is negative as momentum is absorbed towards the ground, and therefore the term $-\overline{u'w'}(\partial U/\partial z)$ is positive and a source of TKE. Without applying momentum perturbation, we find that WRF-LES is unable to generate shear production (Figure 5.8(c)) from the very beginning of the lateral boundary and thus results in a long fetch before turbulence develops, as observed in the plan-view plots of velocities (Figure 5.4 and Figure D.1). Since applying SCPM-M reduces the fetch in velocities as demonstrated previously, in a similar fashion, the fetch in shear production is reduced as well, as it is a combination of both quantities ($-\overline{u'w'}(\partial U/\partial z)$).

We find that SCPM-M with higher amplitudes reduces the fetch in shear production significantly, as shown in Figure 5.8(d). However, in Ktop54H and Ktop88H, strong shear production is observed in the beginning of the LES domain near the lateral boundary (Figure D.6(a-b)). This can be attributed to the application of SCPM-M near and above the CBL, which produces superfluous turbulent motions and ultimately contributes to strong shear production above the CBL. Furthermore, we also observe an expected smaller maximum shear production near the CBL due to the contribution of a strong wind shear ($\partial U/\partial z$) to it near the entrainment zone in all the cases when we applied SCPM-M with varying amplitudes of forces (Figure 5.8(d) and Figure D.6). In other SCPM-M cases with lower and medium amplitudes (Figure D.6(c-f)), the fetch is reduced to a great extent without the generation of spurious motions near the lateral boundary at the beginning of the innermost domain.

Applying momentum perturbation within the LES domain contributes to maximum shear production near the surface in all the cases, as shown in Figure 5.9(c-d) (all other cases are shown in Figure D.9(c-d) for context). When compared to the No-SCPM case, the amount of maximum shear production with SCPM-M is higher below the height of 200 m. There is a small but sharp jump in the shear term near the entrainment zone, regardless of the amplitudes of SCPM-M. Shear production reaches zero just above the CBL in all the SCPM-M cases. They diminishes completely at 650 m above the surface.

Turbulent Transport Term

The turbulent transport term in the TKE budget integrates over the domain height to null in a planar homogeneous case without subsidence, indicating that TKE is transferred among horizontal planes [Stull, 1988]. The $\overline{w'e}$ is the major contributor to the turbulent transport term in the TKE budget equation. In this section, we compute the y- averaged turbulent transport term for different SCPM-M cases.

We observe that, without momentum perturbation, $\overline{w'e}$ redistributes the TKE and generates positive and negative turbulent transport up to the CBL height after 4,800 m along the x-axis (Figure 5.8(e)). After applying SCPM-M, redistribution of the TKE starts at the beginning of the innermost domain, as shown in Figure 5.8(f) (Figure D.7(a-f) shows all the other cases for the sake of completion). Therefore, the fetch in the generation of the turbulent transport term is reduced significantly with SCPM-M.

However, the SCPM-M cases with higher amplitude produce more entrainment near the inflow boundary as compared to the lower amplitude SCPM-M cases (Figure 5.8f) and Figure D.7(a-f). Among the higher amplitude SCPM-M cases, Ktop34H produces lower entrainment (Figure 5.8f and Figure D.7(a-b)). The entrainment is not produced for the lower amplitude SCPM-M cases (Figure D.7(c-e)).

We also compute the profiles of the turbulent transport terms that are area averaged over the last three quarters of the domain (all y and x from 2,880 m to 11,520 m) for the simulations in this section (Figure 5.9(e-f)). We find that without the SCPM-M, the turbulent transport term increases up to 25 m and then continuously decreases up to 140 m, and then increases again up to the bottom of the CBL. Finally it ($\overline{w'e}$) sharply decreases to null at the CBL top (Figure 5.9(e-f)).

In the case of SCPM-M with higher amplitudes, the changes are more abrupt within the CBL and it approaches zero slightly above and below the CBL height (Figure 5.9e). Also, at higher amplitudes, their profiles are not exactly the same but are slightly different throughout the boundary layer up to the CBL top (Figure 5.9e). However, at the lower and medium amplitude SCPM-M cases, the turbulent transport terms are almost similar to the No-SCPM case above 200 m (Figure 5.9f). Similar to the higher amplitude SCPM-M cases, $\overline{w'e}$ reaches zero slightly above and below the CBL height (Figure 5.9f) for the lower and medium amplitude SCPM-M cases.

Pressure Correlation Term

The pressure correlation term plays the role to redistribute TKE within the boundary layer. However, in some cases, it also transfers energy out of the boundary layer through gravity waves (Stull [1988]). Applying SCPM-M significantly reduces the fetch in the redistribution of TKE through the pressure correlation term, and the area averaged profiles become smoother, as shown in Figure 5.9(g) and Figure D.8(a-f). The redistribution of TKE starts from the beginning of the domain with higher and medium amplitude perturbations, while it starts after $x = 100\,m$ for the lower amplitude SCPM-M cases (Figure 5.8h and Figure D.8(a-f)). In the case of Ktop54H and Ktop88H, we observe some spurious motions in the beginning of the domain (at the inflow boundary), as shown in Figure D.8(a-b).

We observe that applying momentum perturbation results in higher magnitude of pressure correlation terms as compared to the No-SCPM case (Figure 5.9(g-h)). The magnitudes of these terms are slightly higher in the case of SCPM-M with higher amplitudes as compared to the SCPM-M cases with lower amplitudes (Figure 5.9(g-h)). The differences among higher and lower amplitude SCPM-M cases are not significant below 100 m as there are very low magnitudes of pressure fluctuations in the surface layer (i.e., the lowest 10% of the boundary layer).

Temporal evolution of TKE

In this subsection, we investigate the evolution of the TKE with time to examine how long the effect of the momentum perturbation lasts after the perturbations are turned off. The SCPM-M simulations are performed for two hours, starting from 18 Z (UTC) to 20 Z (UTC). The application of external forces creates inertia, which is present for the next half an hour from the time when the momentum perturbation is stopped. As shown in Figure 5.10, although the magnitude of TKE that is generated due to inertia is low, it still remains finite from 20 Z to 20:30 Z in the two cases, i.e., Ktop54H and Ktop88H (5.10(a and c)) (Ktop34H is not shown here but similar results are expected). Comparing the results after 20:30 Z, Figure (5.10(a and c)) and Figure (5.10(b and d)), it is clear that the TKE dissipates and the effect of inertia is no longer present after 20:30 Z (UTC). We add a subsection on the effects of the spatial averaging domain on fluxes and TKE budget terms in the supplementary materials section (see subsection S4.1).

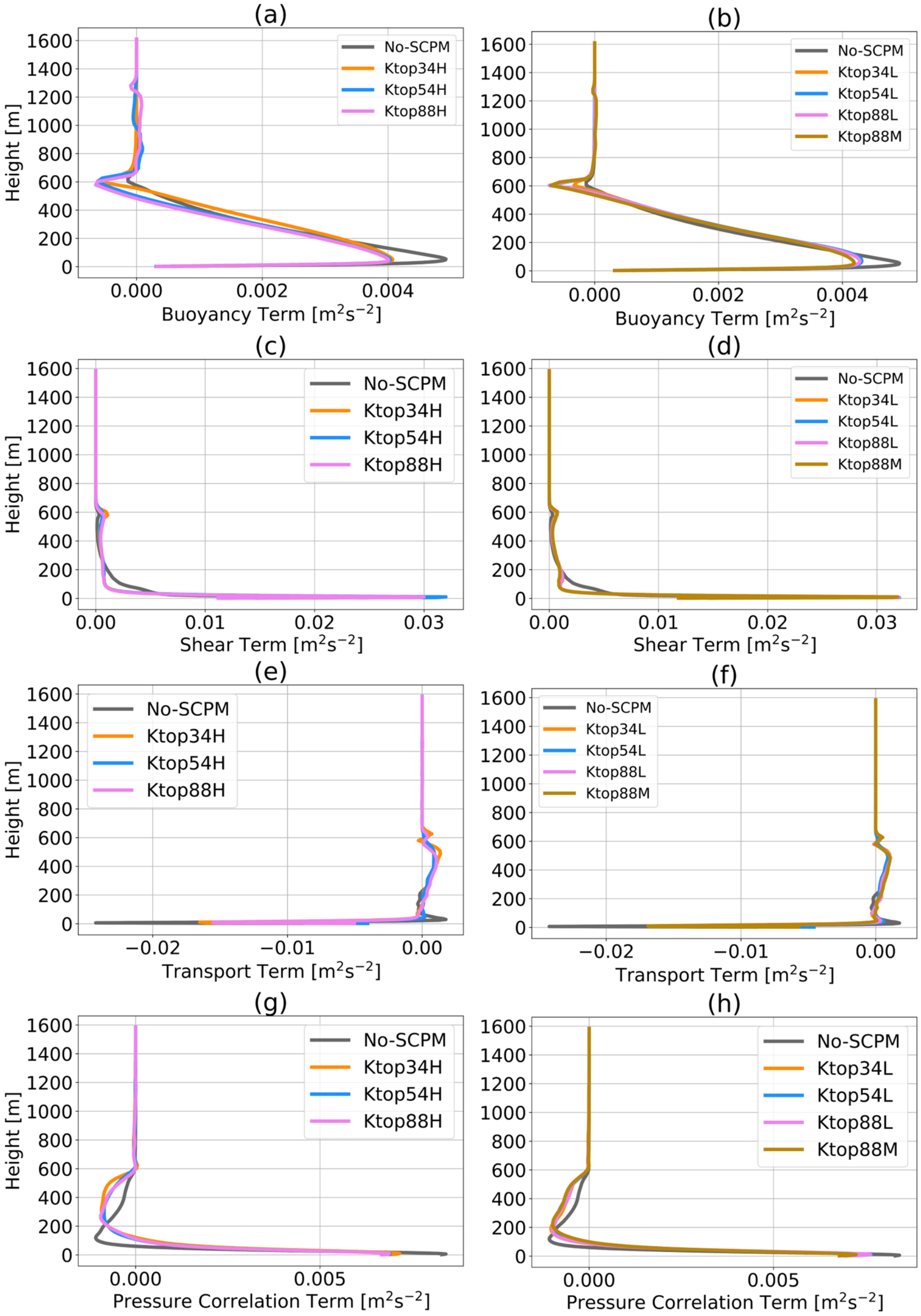

Figure 5.9: Area averaged TKE budget terms over the last three quarters of the domain, i.e., over all y and x from 2,880 m to 11,520 m after applying momentum perturbation for the buoyancy term with (a) higher amplitudes, (b) lower and medium amplitudes; for the shear production term with (c) higher amplitudes (d) lower and medium amplitudes; for the turbulent transport with (e) higher amplitudes (f) lower and medium amplitudes; and for the pressure correlation term with (g) higher amplitudes, (h) lower and medium amplitudes. These plots from are shown for top of the simulation inner domain (up to 1,608 m).

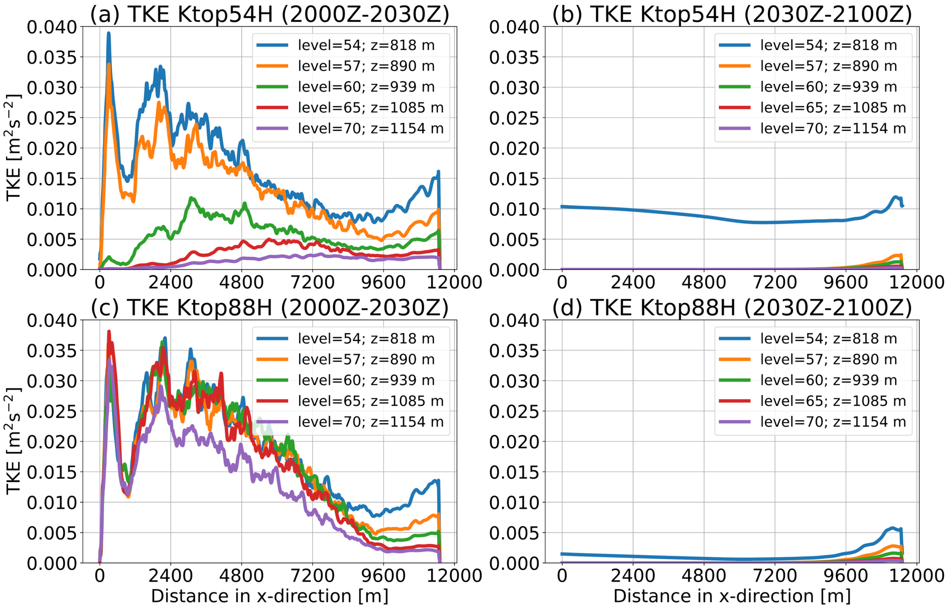

Figure 5.10: Y and time averaged TKE (m^2/s^2) profiles, computed at different heights in the atmosphere during an unstable case when momentum perturbation was turned off from (a) 20 Z to 20:30 Z (UTC) for Ktop54H, (b) 20:30 Z to 21:00 Z (UTC) for Ktop54H, (c) 20 Z to 20:30 Z (UTC) for Ktop88H, and (d) 20:30 Z to 21:00 Z (UTC) for Ktop88H in the different panels of the figure. These profiles are generated for buoyancy terms that are area averaged over the entire simulation inner domain.

5.4 Conclusions

In this work, we have studied the impact of momentum perturbations to generate turbulence in boundary-coupled LES simulations on the turbulent kinetic energy (TKE) budget terms in an unstable boundary layer. While LES models used with periodic boundary conditions are capable of representing realistic turbulence, turbulence representation is challenging in models that couple the mesoscale and microscale models, or when conducting LES simulations with non-periodic conditions, such as in the presence of topography. Additional turbulence generation techniques are needed in these instances. Several such techniques have been developed, each with their own advantages and disadvantages. Here, we implemented a recently developed stochastic cell perturbation technique in WRF-LES simulations to study the impact of turbulence generation on the TKE budget. We used a LES domain at 12 m horizontal resolution that is nested within a mesoscale domain and applied forces in the horizontal and vertical directions at the inflow boundaries of the boundary-coupled LES domain. We performed a set of experiments with varying amplitudes of forces at different heights with respect to the CBL.

We observed that applying SCPM-M accelerated turbulence generation. As a result, the fetch, or the distance needed to fully generate turbulence from the lateral boundary, was reduced. Reduction in the fetch in coupled mesoscale-microscale atmospheric simulations would mean lower computational cost in numerical experiments as a smaller domain needs to be resolved. We also observed that higher amplitude forces produced more perturbation in the velocities near the lateral boundary, while medium and lower amplitude forces produced slightly lower turbulence as compared to the case with higher amplitude SCPM-M.

The forced perturbations produced larger variances in the velocities as compared to the No-SCPM up to the inversion layer. This has also contributed to the higher heat and momentum fluxes when compared to the No-SCPM case. The magnitude of the turbulent kinetic energy

(TKE) produced is always higher for SCPM-M cases than the No-SCPM case throughout the boundary layer. Furthermore, the amount of TKE is higher above the boundary layer as well for the cases where SCPM-M was applied above the boundary layer.

The forced perturbation also affected the buoyancy production in such way that for the lower one-third of the boundary layer, SCPM-M has produced slightly higher buoyancy than the No-SCPM case. While in the middle one-third of the boundary layer, almost same amount of buoyancy is produced for SCPM-M cases as well as No-SCPM. In addition, in the top one-third of the boundary layer, SCPM-M produces higher buoyancy than the No-SCPM case.

Shear production for SCPM-M cases were higher than the No-SCPM case near the surface up to 35 m and then decreased and became equal at 200 m. Near the inversion layer, the shear production term due to SCPM-M again increased due to entrainment induced motions. The implementation of forced perturbation also impacted TKE redistribution through turbulent transport and pressure correlation terms.

Applying forces above the CBL generates additional turbulent structures at the top of the boundary layer, near the inversion layer. However, this is not the case when SCPM-M was applied near or within the CBL. Therefore, to avoid extra entrainment above the boundary layer and obtain computational efficiency, SCPM-M should be applied below the boundary layer or between boundary layer and the surface layer. Among the cases studied in this study, it can be be concluded that applying momentum perturbation up to half of the boundary layer height (the Ktop34H case) is optimal as this case is characterized by significant fetch reduction and minimum generation of additional turbulent motions at the inversion layer.

The application of momentum perturbations to generate turbulence in boundary-coupled LES simulations could benefit a number of disciplines/applications, including wind energy generation, wildfire modeling, cloud top boundary layer research (applicable to off-shore wind) and dispersion problems. Accurate turbulence representation is also important for UAV research and weather forecasting.

Chapter 6

The Role of Fire-induced Turbulence on Ember Transport

6.1 Introduction

Firebrands (also known as embers) play an important role in accelerating the rate of fire spread in both wildland fires as well as fires in the wildland urban interface. Embers are usually generated from burning pieces of bark, twigs and leaves during a wildland fire event. They have the ability to ignite spot fires further away from the main fire front. They can burn houses and damage properties located in WUI, an area where human-made structures are present nearby or within a forest. Thus, a greater risk of damage is associated with them to the communities living in the nearby WUI region. The process by which firebrands ignite surface fuels after landing is known as spotting and the new fire is called a spot fire. Firebrand ignited spot fires can be divided into three phases: (a) generation or launching; (b) transport; and (c) landing. All of these phases are crucial to understand them well and then parameterize accordingly to improve their predictability [Koo et al., 2012, Frediani et al., 2021, 2022]. In this work, we focus on investigating how much distance firebrands could travel from the main fire front and where could they land.

In a wildfire event, there are several processes occurring at different scales that connect fuel, weather, and topography in all three stages, i.e., pre-fire, during fire, and post-fire. Some of these processes are not well parameterized in fire behavior models, adding uncertainty to the prediction of fire intensity, total burned area, and size of a wildfire. In addition, it becomes even more difficult if the wildfire occurs on complex terrain and the models usually result in higher bias and poorer prediction [Lu et al., 2012, Linn et al., 2002, Nakata et al., 2022]. One such component is spotting fire behavior [Frediani et al., 2021], which is either missing or poorly captured in the existing fire behavior models. One major factor for poor spotting fire behavior is the lack of actual observational data on firebrands as spotting is a fairly complex process. The physical shape, size, and decomposition of firebrands is also very difficult to assume in the model without any observation. Some of the existing models assume firebrands shape to be cylindrical (WRF-Fire) [Frediani et al., 2021] or disk-shaped (FIRETEC) [Koo et al., 2012]. Another limitation is that we do not have infomation on what kind of forest or tree would produce which kind of shape and size of the firebrands after burning. However, in some of the models, such as in FIRETEC, firebrands are assumed to have the AA size and decompose as BB. On the other hand, in WRF-Fire, the assumption is that they have XX size and decompose as XX. [What about other models - WFDS & others].

Some of the previous studies and field experiments quantified the fire-induced turbulence during a low intensity wildland fire [Heilman et al., 2015, 2017, Banerjee et al., 2020, Clements et al., 2007], the role of fire-induced turbulence in spotting behavior during a high intensity wildfire is not yet clear. The wind gustiness and turbulence induced by wildland fires play a vital role in the firebrand transport. The high intensity fires can cause more risk to firefighters due to intense spotting, which also changes the predictability of fire behavior and makes suppression and containment attempts more difficult.

The new advances in the mesoscale fire-atmosphere coupled model (WRF-Fire) with a firebrand module provides improved predictability of fire perimeter, fire spotting likelihood, and fire spread [Frediani et al., 2021, 2022] by parameterizing the effects of fire-atmosphere interaction. This provides an opportunity to address the research gap by testing the capability of WRF-Fire model in capturing fire-induced turbulence during an intense wind driven fire, such as the 2021 Marshall Fire. Moreover, building upon this experiment, we further investigate the role of fire-induced turbulence in firebrand transport and spotting using the WRF-Fire model.

We have the following goals in this work: (1) to quantify difference in the turbulence statistics with and without fire ignition(2) to find out how much distance embers are traveling on a statistical basis during an intense wind driven fire; and (3) to evaluate the role of fire-induced turbulence on ember transport. We use the Weather Research and Forecasting (WRF) Fire model to simulate the 2021 Marshall Fire in this study. Our results will advance the understanding of fire behavior at the fire-atmosphere interface, resolving the role of turbulence in ember transport during a strong wind-driven fire.

6.2 Data and Methodology

6.2.1 Data

We use the High Resolution Rapid Refresh (HRRR) data [Benjamin et al., 2016], available at 3 km horizontal grid resolution over a 1-hr period from the National Oceanic & Atmospheric Administration (NOAA) (https://rapidrefresh.noaa.gov/hrrr/) to perform the simulations of this study.

The fuel data is provided by the Anderson 13 class fuel model [Anderson, 1981]. In addition, the topography data is used in this study from the 3-arc second Shuttle Radar Topography Mission terrain data.

In this study, we run the model for 5 hours, i.e., 18 Z UTC (11 a.m. Mountain time) on December 30th to 23 Z UTC (4 p.m. Mountain time) on December 30th 2021. Therefore, we use the HRRR data for the same period at 1-hourly intervals for a total of two simulations as shown in Table 6.1.

6.2.2 Methodology

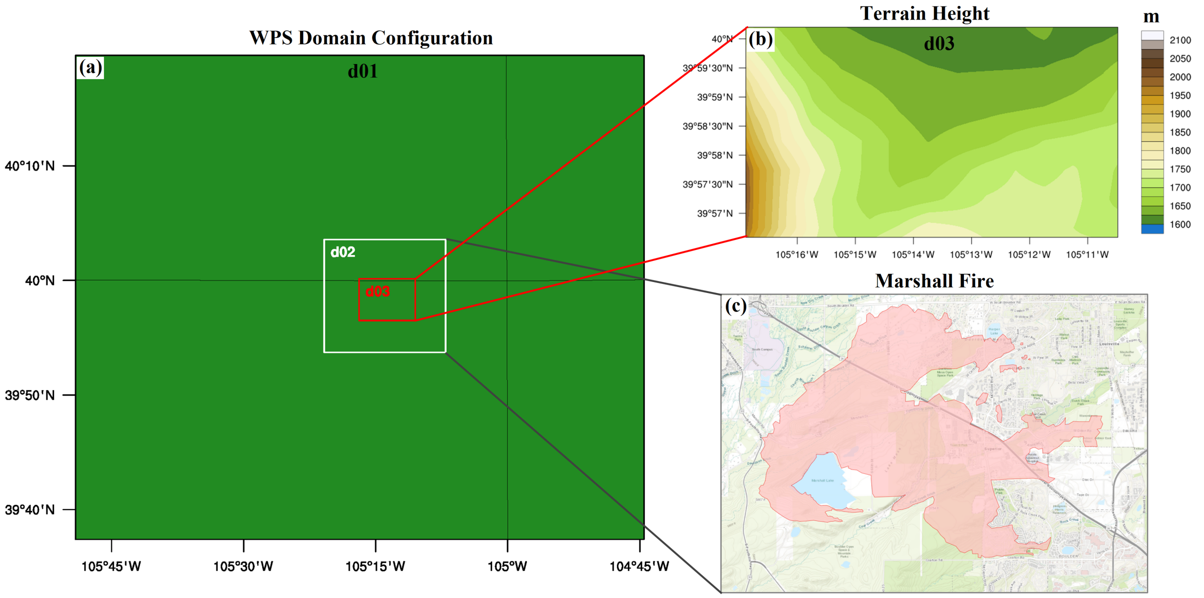

Figure 6.1: The WRF-Fire Preprocessing configuration is shown in panel a with three different two-way nested domains, d01, d02, and d03 with horizontal grid resolution of 480 m, 120 m, and 30 m respectively. Terrain height in meters for domain 3 (d03) and Marshall Fire perimeter (pink color) from domain 2 (d02) are shown in panels b and c respectively. All the results in this study are shown from d03 only.

Model configuration and initialization

In this study, we use the WRF-Fire model version 4.4 [Skamarock et al., 2019, Coen et al., 2013, Clark et al., 2004] with three two-way nested domains to simulate the 2021 Marshall Fire. The WRF-Fire model is a coupled fire-atmosphere model, where the components of a fire model, Coupled Atmosphere-Wildland Fire Environment (CAWFE) model [Coen et al., 2013, Clark et al., 2004] is coupled with a community mesoscale numerical weather prediction (NWP) model, called weather research and forecasting (WRF) model [Skamarock et al., 2019].

During the model simulation, the fire rate of spread is governed by the Rothermel [1972] model, which is controlled by topography, fuel properties, and wind conditions. For a WRF-Fire simulation, a fire grid is also required in addition to the meteorological grid that is specified in a standard WRF simulation. The fire grid is four times more refined than the meteorological grid ($x = y = 30\,m$) in order to compute small-scale changes in fuel characteristics and fire spread. A recently developed, an accurate level-set method, parameterized by Muñoz-Esparza et al. [2018] is used to track the changes in the fire area/perimeter.

We perform two sets of simulations (Table 6.1) to evaluate the turbulence characteristics in both scenarios, when the fire ignition is active and when it is not active in the model. The horizontal grid resolutions are 480 m, 120 m, and 40 m for the outermost, middle, and innermost domains respectively for both set of experiments. We used 44 vertical pressure levels for the WRF-Fire simulations. The initial and boundary condition for the model were provided from HRRR which has a horizontal grid resolution of 3 km and is available 1-hourly.

All the simulations are initialized at the same time and run from 18 Z UTC (11 a.m. Mountain time) on December 30th to 23 Z UTC (4 p.m. Mountain time) on December 30th 2021, allowing 1 hour for model spin-up and 4 hours for the simulations. Only one set of horizontal grid resolution is used for the model set-up in our study: 480 m, 120 m, and 30 m for the outermost (d01), middle (d02), and innermost domain (d03) respectively. We use 44 vertical pressure levels with the top level at 13,706.5 m for all WRF-Fire simulations.

In both the experiments (fire & no-fire), the mesoscale domain (d01) has a horizontal extent of 92.64 km by 78.72 km, with 193 grid cells in X and 164 grid cells Y directions, while domain 2 (d02) has 165 grids X and 153 grids Y directions with a domain size of 19.8 km by 18.36 km, and domain 3 (d03) has a horizontal extent of 9.15 km by 6.75 km, with 305 grid cells in X and 225 grid cells Y directions. The time step for integration is 1 second for d01 in the coarser grid simulation. The outputs for innermost domain (d03) are stored at every second and the parent time step ratio is 4 for all simulations.

We choose the Yonsei University (abbreviated as YSU throughout this manuscript) [Hong et al., 2006] PBL scheme for d01 and d02, while the d03 domain is turbulence-resolving. We use the rapid radiative transfer model (RRTM) [Mlawer et al., 1997] for the longwave radiation schemes and the Dudhia scheme [Dudhia, 1989] for the shortwave radiation scheme throughout the three domains for both simulations. For the surface physics, we use the Revised MM5 Scheme [Jiménez et al., 2012] throughout the three domains for all simulations. Furthermore, we use the Unified NOAH land-surface model [Mukul Tewari et al., 2004] as the land surface scheme throughout the three domains for both simulations. For the microphysics parameterization, we use the WRF Single–moment 6–class scheme (WSM6) [Hong and Lim, 2006] for all simulations and in all domains. We do not use cumulus parameterizations in any of the domains during these experiments.

6.3 Results and Discussions

Firebrands are released at several locations along the fire front, from grid points with a high fire rate of spread and denser fuel loads [Frediani et al., 2021]. Multiple heights are used to

WRF-FIRE experiment	**Fire module** d03	**Simulation Start** time in UTC	**Simulation End** time in UTC
Fire	active	18:00	23:00
No-Fire	not active	18:00	23:00

Table 6.1: The table shows the list of simulations performed for this study with fire an active fire module and without an active fire module, at the horizontal grid resolution of 480 m, 120 m, 30 m in the WRF-Fire model. The results in this manuscript is presented from the model outputs at 30 m horizontal grid resolution, i.e., from the inner-most domain (d03) only.

discharge firebrands, which are then carried by the atmosphere and consumed by combustion [Frediani et al., 2021, 2022, Juliano et al., 2022].

6.3.1 Fire Area

To evaluate the capability of the WRF-Fire model, we compute the fire area at 21:30:00 UTC (3:30:00 p.m. local time), i.e., after 3 hrs of the fire ignition/start time (18:30:00 UTC or 11:30:00 a.m. local time). Since the fire ignition point lies inside d03, we use it for computing the simulated fire area after the fire ignition period. We observe that WRF-Fire is able to capture the fire perimeter during the 2021 Marshall Fire, as shown Figure 6.2a at

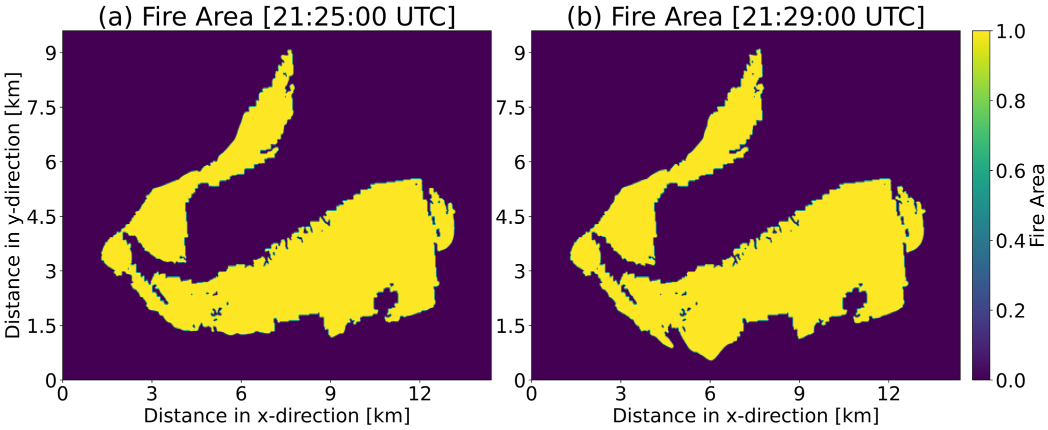

Figure 6.2: The fire area from the d03: (a) fire area at 21:25:00 UTC;(b) fire area at 21:29:00 UTC. The limits of color bar is same for all these plots from a to b.

30th December 21:25:00 UTC (3:25:00 p.m. local time) and Figure 6.2b at 30th December 21:29:00 UTC (3:29:00 p.m. local time).

However, the simulated fire perimeter as shown in Figure 6.2(a-b) does not reflect the impact of firebrand transport as the the spotting parameterization has not been used in this experiment so far.

6.3.2 W component of velocity

In this study, we plan to launch embers at a height of 10 m above ground level (AGL) and from those locations where the W component of velocity is positive. We choose only those

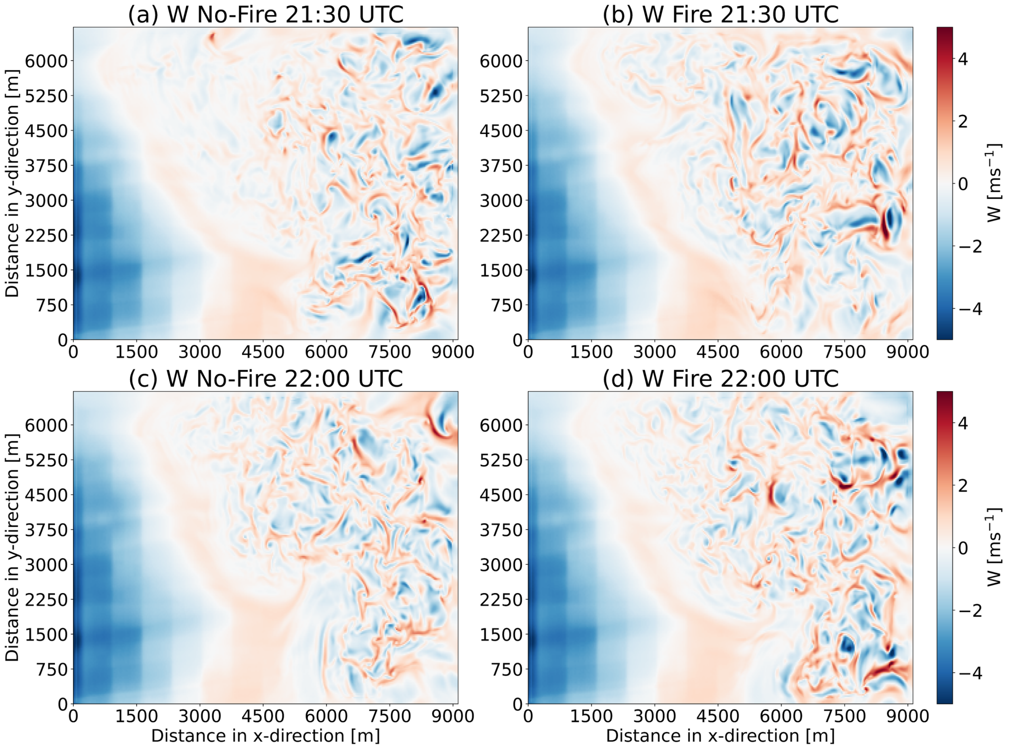

Figure 6.3: The W component of velocity is computed at at two time instants at level=2, z=1741 m (AGL) from d03 in such a way that the panels from a to d in this figure show: (a) W with no fire at 21:30 UTC;(b) W with fire at 21:30 UTC;(c) W with no fire at 22:00 UTC;(d) W with fire at 22:00 UTC. The limits of color bar is same for all these plots from a to d.

locations with a positive W for launching embers as this would ensure a positive ejection velocity and the embers would not fall off at the instants when they are launched.

We observe that an active fire in the model creates a higher magnitude of W (instantaneous) than when the fire is not active as shown in Figure 6.3(a-d). The result for the instantaneous W, spatial plot is directly shown from from the d03.

6.4 Conclusion and Future Work

This study uses the WRF-Fire model to evaluate the impact of active fire ignition during fire spread on turbulence statistics and related meteorological conditions. We use two sets of simulations with similar model set-up, initial condition, and design, with the only difference being an active fire ignition in one and not in the other.

With an active fire, WRF-Fire is able to capture the evolution of the fire perimeter. The simulation yields stronger vertical components of instantaneous velocities with the fire module activated compared to one without an active fire. The mean and variations of the vertical velocity component will provide the initial conditions for ember transport.

Based on the preliminary results of this study, we will continue to compare the components of turbulence statistics, and use TKE to quantify turbulence during a high intensity fire, driven by heavy wind. In addition to that, we will also explore the impact of the resulting turbulence on the distance that embers travel when the fire is active/inactive in the model.

Chapter 7

Conclusion

This dissertation has developed a framework for the mapping and modeling of fires in the wildland-urban interface (WUI) using remote sensing data and regional models with land-atmosphere-fire interaction capability.

Chapter 1 has provided the general idea about the wildland-urban interface (WUI) and different factors that inform wildland fire behavior, such as, fuel, weather, and topography.

In **chapter 2**, I examine and revisit the existing definitions of WUI for California. In this chapter, I have reported the occurrences of wildfires with respect to the WUI and quantified how much of the WUI is on complex topography in California (CA), which intensifies fire behavior and complicates fire suppression. I have additionally analyzed the relative importance of WUI related parameters such as housing density, vegetation density, and distance to wildfires, as well as topographic factors such as slope, elevation, aspect, and surface roughness, on the occurrence of large and small wildfires and the burned area of large wildfires near the WUI. I found that a very small percentage of wildfire ignition points and large wildfire burned areas ($>$ 400 hectares or 1,000 acres) were located in the WUI areas. A small percentage of large wildfires encountered in WUI (3%) and the WUI area accounted for only 4% of the area burned, which increased to 5% and 56% respectively outside WUI (5 km buffer from WUI). Similarly, 66% of fires ignited outside WUI, whereas only 3.6% ignited within WUI. Results from this study have implications for fuel management and infrastructure hardening, as well as for fire suppression and community response.

The **chapter 3** proposes a novel WUI definition of WUI using vector-based edge intersection. Herein, I mapped a finer-scale, novel vector-based WUI for California (CA) based on the intersection of boundaries of wildland vegetation and building footprints. The direct intersection is referred to as a direct WUI, whereas the intersection at 100-m buffer radius is known as an indirect WUI. The direct WUI was found to have a higher total segment length compared to the indirect WUI and found to be less fragmented as well. More fires were ignited closer to direct WUI than indirect WUI due to their proximity to communities. However, the overlap of past fire perimeters with the indirect WUI was found to be greater than that with the direct WUI, which shows that more areas were burned in the indirect WUI. This new approach may help land managers and policymakers in land-use planning, reducing threats to fire-prone communities.

The intensity and frequency of wildfires in California (CA) have increased in recent years, causing significant damage to human health and property. In October 2007 a number of small fire events, collectively referred to as the Witch Creek Fire or Witch Fire, started in southern CA and intensified under strong Santa Ana winds. The Witch Fire remains one of top ten largest wildfires in modern California history. In **chapter 4**, I evaluated the performance of the Weather Research and Forecasting (WRF) model to simulate a 2007 wildfire event (Witch Creek Fire) in terms of meteorological parameters at different geographical locations. As a test of current mesoscale modeling capabilities, I use the WRF model to simulate the 2007 wildfire event in terms of meteorological parameters and smoke propagation. The main objectives of the present study was to investigate the impact of choice of horizontal grid resolution and PBL schemes, in capturing meteorological conditions during a Mega fire. I evaluated the predictive capability of the WRF model with respect to key meteorological and fire-weather forecast parameters such as wind, moisture and temperature. Three two-way nested domain sets with horizontal resolutions of 36 km, 12 km and 4 km and 9 km, 3 km, and 1 km were used along with the North American Regional Reanalysis (NARR) data (Mesinger et al. [2006]) at 12 km resolution to provide initial and boundary conditions for the simulation. Results were validated using the Wyoming radiosonde, surface weather station datasets, as well as Ameriflux datasets for the innermost domain of the model. I found that the model can capture fire-weather associated with the fire event close to the surface. The spatial and temporal variability of different meteorological parameters in the model, on the other hand, was highly dependent on grid resolutions and PBL scheme selection. In summary, the results of this study with four simulations indicated that finer grid resolution simulations improved the model's ability to predict near surface meteorological conditions more than coarser resolution simulations. The results also showed that wind is more difficult to capture than temperature and relative humidity, even at a finer resolution of 1,km. Furthermore, the MYNN scheme is found to perform better than the YSU scheme in general.

The **chapter 5** validates the impact of a simple and computationally efficient Stochastic Cell Perturbation method using momentum perturbation (SCPM-M) to accelerate the generation of turbulence in boundary-coupled large-eddy simulation (LES) simulations using the Weather Research and Forecasting (WRF) model. Mesoscale-to-microscale coupling is an important tool to conduct turbulence-resolving multiscale simulations of realistic atmospheric flows, which are crucial for applications ranging from wind energy to wildfire spread studies. Different techniques are used to facilitate the development of realistic turbulence in the LES domain while minimizing computational cost. In chapter 5, I simulate a convective boundary layer (CBL) in order to characterize the production and dissipation of turbulent kinetic energy (TKE) and the variation of the TKE budget terms. The WRF-LES domain is one-way nested within an idealized mesoscale domain. I quantify TKE budget terms associated with shear production, buoyant production, dissipation, and transport of TKE throughout the simulation domain. Furthermore, I evaluate the impact of the magnitude and the vertical extent of momentum perturbations on TKE budget terms by applying momentum perturbations of three magnitudes below, up to, and above the CBL. Application of momentum perturbation results in the reduction of fetch in turbulence generation to a great extent. It also produces an adequate amount of turbulence when applied at the half of the CBL (Ktop34H); while when applied above the CBL, it generates additional structures at the top of the CBL, near the inversion layer. In addition, applying SCPM-M over varying heights with different amplitudes of forces produces different patterns of TKE budgets and their contribution to the TKE. The findings of this study provide a better understanding of how different budget terms contribute to TKE in a boundary-coupled LES simulation.

In **chapter 6**, I have performed simulations using a newly developed fire-spotting parameterization in the coupled atmosphere-fire, WRF-Fire model. Based on the initial simulations, I have found that in case of an active fire in the model, it resulted in stronger vertical components of instantaneous velocity as compared to the case without an active fire. This can lead to larger distance travelled by embers during a wildfire event near WUI areas, resulting more damages to the communities living in the WUI even when the fires do not ignite in it. In the future, I will analyze the role of turbulence generated by Santa Ana winds during a wildfire event. Furthermore, I would evaluate the distance embers can statistically travel during a wildfire fueled by strong gusts over complex terrain. Results from this study would help in validating and mapping WUI, fuel management, land-use planning, better evaluation plans, etc.

Overall, this dissertation can provide us with a deeper understanding of some of the important issues that have wide-ranging practical implications for forest managers, meteorologists, policymakers, communities, and researchers. Consideration of the factors like buffer distance, topography, etc. are crucial for a more adequate definition of WUI. It would help in planning fuel treatment and home hardening projects as well as in resource allocation for wildfire preparedness in WUIs. In terms of short term benefits, this study would enhance the early warning and better prediction of fire-weather and ember travel distance which would further help in evacuation plans. In terms of long term advantages, the high-resolution WUI map would help in land-use planning, fuel management with a better storage and utilization of data in a simpler format. The application of SCPM-M to generate adequate turbulence could benefit a number of disciplines and applications, including wind energy generation, wildfire modeling, weather forecasting, cloud top boundary layer research (applicable to off-shore wind) and dispersion problems. Results of this study will help foresters, land managers, fire risk-prone communities, and government at all levels in developing techniques, models, policies & adapting to live with wildfires in a changing climate. This dissertation would provide the future research directions, such as, developing a dynamic WUI map for the globe, improving the fire-behavior models, quantifying the role of small and large scale eddies in the ember transport, and the modeling short and long distance ember for a complex environment.

Bibliography

H. E. Anderson. *Aids to determining fuel models for estimating fire behavior*, volume 122. US Department of Agriculture, Forest Service, Intermountain Forest and Range . . . , 1981.

P. Andrews, M. Finney, and M. Fischetti. Predicting wildfires. *Scientific American*, 297(2): 46–55, 2007.

T. Banerjee, W. Heilman, S. Goodrick, J. K. Hiers, and R. Linn. Effects of canopy midstory management and fuel moisture on wildfire behavior. *Scientific reports*, 10(1):1–14, 2020.

J. G. Bartlett, D. Mageean, and R. O'Connor. Residential expansion as a continental threat to us coastal ecosystems. *Population and Environment*, 21(5):429–468, 2000.

S. G. Benjamin, S. S. Weygandt, J. M. Brown, M. Hu, C. R. Alexander, T. G. Smirnova, J. B. Olson, E. P. James, D. C. Dowell, G. A. Grell, et al. A north american hourly assimilation and model forecast cycle: The rapid refresh. *Monthly Weather Review*, 144 (4):1669–1694, 2016.

A. Bento-Gonçalves and A. Vieira. Wildfires in the wildland-urban interface: Key concepts and evaluation methodologies. *Science of the total environment*, 707:135592, 2020.

W. J. Bond and R. Keane. Fires, ecological effects of. *Reference Module in Life Sciences. doi: 10.1016/B978-0-12-809633-8.02098-7.*, 2017.

D. M. Bowman, J. K. Balch, P. Artaxo, W. J. Bond, J. M. Carlson, M. A. Cochrane, C. M. D'Antonio, R. S. DeFries, J. C. Doyle, S. P. Harrison, et al. Fire in the earth system. *science*, 324(5926):481–484, 2009.

D. M. Bowman, J. Balch, P. Artaxo, W. J. Bond, M. A. Cochrane, C. M. D'antonio, R. DeFries, F. H. Johnston, J. E. Keeley, M. A. Krawchuk, et al. The human dimension of fire regimes on earth. *Journal of biogeography*, 38(12):2223–2236, 2011.

D. M. Bowman, C. A. Kolden, J. T. Abatzoglou, F. H. Johnston, G. R. van der Werf, and M. Flannigan. Vegetation fires in the anthropocene. *Nature Reviews Earth & Environment*, 1(10):500–515, 2020.

G. A. Bradley. *Land use and forest resources in a changing environment: the urban/forest interface*. Number 49. University of Washington Press, 1984.

M. J. Brewer and C. B. Clements. The 2018 camp fire: Meteorological analysis using in situ observations and numerical simulations. *Atmosphere*, 11(1):47, 2019.

G. H. Bryan and J. M. Fritsch. A benchmark simulation for moist nonhydrostatic numerical models. *Monthly Weather Review*, 130(12):2917–2928, 2002.

M. Burke, A. Driscoll, S. Heft-Neal, J. Xue, J. Burney, and M. Wara. The changing risk and burden of wildfire in the united states. *Proceedings of the National Academy of Sciences*, 118(2):e2011048118, 2021.

D. T. Butry, M. Gumpertz, and M. G. Genton. The production of large and small wildfires. In *The Economics of Forest Disturbances*, pages 79–106. Springer, 2008.

M. D. Caggiano, T. J. Hawbaker, B. M. Gannon, and C. M. Hoffman. Building loss in wui disasters: evaluating the core components of the wildland–urban interface definition. *Fire*, 3(4):73, 2020.

S. H. Cannon and J. DeGraff. The increasing wildfire and post-fire debris-flow threat in western usa, and implications for consequences of climate change. In *Landslides–disaster risk reduction*, pages 177–190. Springer, 2009.

S.-H. Chen and W.-Y. Sun. A one-dimensional time dependent cloud model. *Journal of the Meteorological Society of Japan. Ser. II*, 80(1):99–118, 2002.

J. Ching, R. Rotunno, M. LeMone, A. Martilli, B. Kosovic, P. Jimenez, and J. Dudhia. Convectively induced secondary circulations in fine-grid mesoscale numerical weather prediction models. *Monthly Weather Review*, 142(9):3284–3302, 2014.

T. L. Clark, J. Coen, and D. Latham. Description of a coupled atmosphere–fire model. *International Journal of Wildland Fire*, 13(1):49–63, 2004.

H. Clarke, J. P. Evans, and A. J. Pitman. Fire weather simulation skill by the weather research and forecasting (wrf) model over south-east australia from 1985 to 2009. *International Journal of Wildland Fire*, 22(6):739–756, 2013.

C. B. Clements, S. Zhong, S. Goodrick, J. Li, B. E. Potter, X. Bian, W. E. Heilman, J. J. Charney, R. Perna, M. Jang, et al. Observing the dynamics of wildland grass fires: Fireflux—a field validation experiment. *Bulletin of the American Meteorological Society*, 88(9):1369–1382, 2007.

J. Coen. Some requirements for simulating wildland fire behavior using insight from coupled weather—wildland fire models. *Fire*, 1(1):6, 2018.

J. L. Coen, M. Cameron, J. Michalakes, E. G. Patton, P. J. Riggan, and K. M. Yedinak. Wrf-fire: coupled weather–wildland fire modeling with the weather research and forecasting model. *Journal of Applied Meteorology and Climatology*, 52(1):16–38, 2013.

A. E. Cohen, S. M. Cavallo, M. C. Coniglio, and H. E. Brooks. A review of planetary boundary layer parameterization schemes and their sensitivity in simulating southeastern us cold season severe weather environments. *Weather and forecasting*, 30(3):591–612, 2015.

J. D. Cohen. Preventing disaster: home ignitability in the wildland-urban interface. *Journal of forestry*, 98(3):15–21, 2000.

S. N. Collins, R. S. James, P. Ray, K. Chen, A. Lassman, and J. Brownlee. Grids in numerical weather and climate models. *Climate change and regional/local responses*, 256, 2013.

A. Connolly, L. van Veen, J. Neher, B. J. Geurts, J. Mirocha, and F. K. Chow. Efficacy of the cell perturbation method in large-eddy simulations of boundary layer flow over complex terrain. *Atmosphere*, 12(1):55, 2021.

M. G. Cruz and M. E. Alexander. Uncertainty associated with model predictions of surface and crown fire rates of spread. *Environmental Modelling & Software*, 47:16–28, 2013.

J. B. Davis et al. The wildland-urban interface: paradise or battleground? *Journal of forestry*, 88(1):26–31, 1990.

F. Di Giuseppe, F. Pappenberger, F. Wetterhall, B. Krzeminski, A. Camia, G. Libertá, and J. San Miguel. The potential predictability of fire danger provided by numerical weather prediction. *Journal of Applied Meteorology and Climatology*, 55(11):2469–2491, 2016.

L. Di Mare, M. Klein, W. Jones, and J. Janicka. Synthetic turbulence inflow conditions for large-eddy simulation. *Physics of Fluids*, 18(2):025107, 2006.

J. Dudhia. Numerical study of convection observed during the winter monsoon experiment using a mesoscale two-dimensional model. *Journal of Atmospheric Sciences*, 46(20):3077–3107, 1989.

J. Eidenshink, B. Schwind, K. Brewer, Z.-L. Zhu, B. Quayle, and S. Howard. A project for monitoring trends in burn severity. *Fire ecology*, 3(1):3–21, 2007.

A. C. Fernandez-Pello. Wildland fire spot ignition by sparks and firebrands. *Fire Safety Journal*, 91:2–10, 2017.

R. G. Fovell and Y. Cao. The santa ana winds of southern california: winds, gusts, and the 2007 witch fire. *Wind Struct*, 24(6):529–564, 2017.

R. G. Fovell, M. J. Brewer, and R. J. Garmong. The december 2021 marshall fire: Predictability and gust forecasts from operational models. *Atmosphere*, 13(5):765, 2022.

M. Frediani, T. W. Juliano, A. DeCastro, B. Kosovic, and J. Knievel. A fire-spotting parameterization coupled with the wrf-fire model. *Earth and Space Science Open Archive ESSOAr*, 2021.

M. Frediani, T. W. Juliano, J. C. Knievel, S. A. Tessendorf, and B. Kosovic. The role of fire spotting in fire-weather prediction. *Earth and Space Science Open Archive ESSOAr*, 2022.

G. Giunta, R. Salerno, A. Ceppi, G. Ercolani, and M. Mancini. Effects of model horizontal grid resolution on short-and medium-term daily temperature forecasts for energy consumption application in european cities. *Advances in Meteorology*, 2019, 2019.

D. Glickman and B. Babbitt. Urban wildland interface communities within the vicinity of federal lands that are at high risk from wildfire. *Federal Register*, 66(3):751–777, 2001.

T. S. Glickman. *Glossary of meteorology.* American Meteorological Society, 2000.

P. B. Gove. New international dictionary. *Springfield, MA: Merriam-Webster Inc*, 1986.

R. Graham, M. Finney, C. McHugh, J. Cohen, D. Calkin, R. Stratton, L. Bradshaw, and N. Nikolov. Fourmile canyon fire findings. *Gen. Tech. Rep. RMRS-GTR-289. Fort Collins, CO: US Department of Agriculture, Forest Service, Rocky Mountain Research Station. 110 p.*, 289, 2012.

G. A. Grell. Prognostic evaluation of assumptions used by cumulus parameterizations. *Monthly weather review*, 121(3):764–787, 1993.

R. G. Haight, D. T. Cleland, R. B. Hammer, V. C. Radeloff, and T. S. Rupp. Assessing fire risk in the wildland-urban interface. *Journal of Forestry*, 102(7):41–48, 2004.

B. B. Hanberry. Reclassifying the wildland–urban interface using fire occurrences for the united states. *Land*, 9(7):225, 2020.

S. Haupt, L. K. Berg, A. Decastro, D. J. Gagne, P. Jimenez, T. Juliano, B. Kosovic, J. D. Mirocha, E. Quon, J. Sauer, et al. Report of the atmosphere to electrons mesoscale-to-microscale coupling project (fy2019). Technical report, Pacific Northwest National Lab.(PNNL), Richland, WA (United States . . . , 2019a.

S. E. Haupt, B. Kosovic, W. Shaw, L. K. Berg, M. Churchfield, J. Cline, C. Draxl, B. Ennis, E. Koo, R. Kotamarthi, et al. On bridging a modeling scale gap: Mesoscale to microscale coupling for wind energy. *Bulletin of the American Meteorological Society*, 100(12):2533–2550, 2019b.

S. E. Haupt, R. Arthur, A. Decastro, D. J. Gagne, A. Jonko, B. Kosovic, T. Mccandless, R. K. Rai, L. K. Berg, S. Dettling, et al. Fy 2020 report of the atmosphere to electrons land-based mesoscale-to-microscale coupling project. Technical report, Pacific Northwest National Lab.(PNNL), Richland, WA (United States), 2020.

W. E. Heilman, C. B. Clements, D. Seto, X. Bian, K. L. Clark, N. S. Skowronski, and J. L. Hom. Observations of fire-induced turbulence regimes during low-intensity wildland fires in forested environments: implications for smoke dispersion. *Atmospheric Science Letters*, 16(4):453–460, 2015.

W. E. Heilman, X. Bian, K. L. Clark, N. S. Skowronski, J. L. Hom, and M. R. Gallagher. Atmospheric turbulence observations in the vicinity of surface fires in forested environments. *Journal of Applied Meteorology and Climatology*, 56(12):3133–3150, 2017.

M. P. Heris, N. L. Foks, K. J. Bagstad, A. Troy, and Z. H. Ancona. A rasterized building footprint dataset for the united states. *Scientific data*, 7(1):1–10, 2020.

C. Homer, J. Dewitz, S. Jin, G. Xian, C. Costello, P. Danielson, L. Gass, M. Funk, J. Wickham, S. Stehman, et al. Conterminous united states land cover change patterns 2001–2016 from the 2016 national land cover database. *ISPRS Journal of Photogrammetry and Remote Sensing*, 162:184–199, 2020.

S.-Y. Hong and J.-O. J. Lim. The wrf single-moment 6-class microphysics scheme (wsm6). *Asia-Pacific Journal of Atmospheric Sciences*, 42(2):129–151, 2006.

S.-Y. Hong and H.-L. Pan. Nonlocal boundary layer vertical diffusion in a medium-range forecast model. *Monthly weather review*, 124(10):2322–2339, 1996.

S.-Y. Hong, Y. Noh, and J. Dudhia. A new vertical diffusion package with an explicit treatment of entrainment processes. *Monthly weather review*, 134(9):2318–2341, 2006.

T. A. Hutchinson. An adaptive time-step for increased model efficiency. In *Extended Abstracts, Eighth WRF Users' Workshop*, page 4, 2007.

Z. I. Janić. Nonsingular implementation of the mellor-yamada level 2.5 scheme in the ncep meso model. *NCEP Office Note*, 2001.

J. S. Jenness. Calculating landscape surface area from digital elevation models. *Wildlife Society Bulletin*, 32(3):829–839, 2004.

P. A. Jiménez, J. Dudhia, J. F. González-Rouco, J. Navarro, J. P. Montávez, and E. García-Bustamante. A revised scheme for the wrf surface layer formulation. *Monthly weather review*, 140(3):898–918, 2012.

P. A. Jiménez, D. Muñoz-Esparza, and B. Kosović. A high resolution coupled fire–atmosphere forecasting system to minimize the impacts of wildland fires: Applications to the chimney tops ii wildland event. *Atmosphere*, 9(5):197, 2018.

S. Jin, C. Homer, L. Yang, P. Danielson, J. Dewitz, C. Li, Z. Zhu, G. Xian, and D. Howard. Overall methodology design for the united states national land cover database 2016 products. *Remote Sensing*, 11(24):2971, 2019.

Y. Jin, M. L. Goulden, N. Faivre, S. Veraverbeke, F. Sun, A. Hall, M. S. Hand, S. Hook, and J. T. Randerson. Identification of two distinct fire regimes in southern california: implications for economic impact and future change. *Environmental Research Letters*, 10 (9):094005, 2015.

K. M. Johnson, A. Nucci, and L. Long. Population trends in metropolitan and nonmetropolitan america: Selective deconcentration and the rural rebound. *Population Research and Policy Review*, 24(5):527–542, 2005.

L. M. Johnston and M. D. Flannigan. Mapping canadian wildland fire interface areas. *International journal of wildland fire*, 27(1):1–14, 2017.

W. M. Jolly, M. A. Cochrane, P. H. Freeborn, Z. A. Holden, T. J. Brown, G. J. Williamson, and D. M. Bowman. Climate-induced variations in global wildfire danger from 1979 to 2013. *Nature communications*, 6(1):1–11, 2015.

T. W. Juliano, N. Lareau, M. Frediani, K. Shamsaei, M. Eghdami, K. A. Kosiba, J. Wurman, A. DeCastro, B. Kosović, and H. Ebrahimian. Toward a better understanding of wildfire behavior in the wildland-urban interface: A case study of the 2021 marshall fire. *Earth and Space Science Open Archive ESSOAr*, 2022.

A. Keat, U. Piomelli, E. Ballaras, and H. Kaltenbach. A priori and a posteriori tests of inflow conditions for large-eddy simulations. *Phys. Fluids*, 16:4696–4712, 2004.

J. E. Keeley and A. D. Syphard. Twenty-first century california, usa, wildfires: fuel-dominated vs. wind-dominated fires. *Fire Ecology*, 15(1):1–15, 2019.

M. Klein, A. Sadiki, and J. Janicka. A digital filter based generation of inflow data for spatially developing direct numerical or large eddy simulations. *Journal of computational Physics*, 186(2):652–665, 2003.

E. Koo, P. J. Pagni, D. R. Weise, and J. P. Woycheese. Firebrands and spotting ignition in large-scale fires. *International Journal of Wildland Fire*, 19(7):818–843, 2010.

E. Koo, R. R. Linn, P. J. Pagni, and C. B. Edminster. Modelling firebrand transport in wildfires using higrad/firetec. *International journal of wildland fire*, 21(4):396–417, 2012.

B. Kosović. Subgrid-scale modelling for the large-eddy simulation of high-reynolds-number boundary layers. *Journal of Fluid Mechanics*, 336:151–182, 1997.

H. A. Kramer, M. H. Mockrin, P. M. Alexandre, S. I. Stewart, and V. C. Radeloff. Where wildfires destroy buildings in the us relative to the wildland–urban interface and national fire outreach programs. *International journal of wildland fire*, 27(5):329–341, 2018.

H. A. Kramer, M. H. Mockrin, P. M. Alexandre, and V. C. Radeloff. High wildfire damage in interface communities in california. *International journal of wildland fire*, 28(9):641–650, 2019.

M. Kumar, S. Li, P. Nguyen, and T. Banerjee. Revisiting the existing definitions of wildland-urban interface for california. *Earth and Space Science Open Archive*, 2020.

K. Lagouvardos, V. Kotroni, T. M. Giannaros, and S. Dafis. Meteorological conditions conducive to the rapid spread of the deadly wildfire in eastern attica, greece. *Bulletin of the American Meteorological Society*, 100(11):2137–2145, 2019.

H. Le, P. Moin, and J. Kim. Direct numerical simulation of turbulent flow over a backward-facing step. *Journal of fluid mechanics*, 330:349–374, 1997.

S. Li and T. Banerjee. Spatial and temporal pattern of wildfires in california from 2000 to 2019. *Scientific reports*, 11(1):1–17, 2021.

T. Lindley, D. A. Speheger, M. A. Day, G. P. Murdoch, B. R. Smith, N. J. Nauslar, and D. C. Daily. Megafires on the southern great plains. *Journal of Operational Meteorology*, 7(12), 2019.

R. Linn, J. Reisner, J. J. Colman, and J. Winterkamp. Studying wildfire behavior using firetec. *International journal of wildland fire*, 11(4):233–246, 2002.

R. Linn, J. Winterkamp, C. Edminster, J. J. Colman, and W. S. Smith. Coupled influences of topography and wind on wildland fire behaviour. *International Journal of Wildland Fire*, 16(2):183–195, 2007.

J. Liu, G. C. Daily, P. R. Ehrlich, and G. W. Luck. Effects of household dynamics on resource consumption and biodiversity. *Nature*, 421(6922):530–533, 2003.

W. Lu, S. Zhong, J. Charney, X. Bian, and S. Liu. Wrf simulation over complex terrain during a southern california wildfire event. *Journal of Geophysical Research: Atmospheres*, 117 (D5), 2012.

D. V. Mallia, A. K. Kochanski, K. E. Kelly, R. Whitaker, W. Xing, L. E. Mitchell, A. Jacques, A. Farguell, J. Mandel, P.-E. Gaillardon, et al. Evaluating wildfire smoke transport within a coupled fire-atmosphere model using a high-density observation network for an episodic smoke event along utah's wasatch front. *Journal of Geophysical Research: Atmospheres*, 125(20):e2020JD032712, 2020.

S. Martinuzzi, S. I. Stewart, D. P. Helmers, M. H. Mockrin, R. B. Hammer, and V. C. Radeloff. The 2010 wildland-urban interface of the conterminous united states. *Research Map NRS-8. Newtown Square, PA: US Department of Agriculture, Forest Service, Northern Research Station. 124 p.[includes pull-out map].*, 8:1–124, 2015.

N. Masoudvaziri, F. S. Bardales, O. K. Keskin, A. Sarreshtehdari, K. Sun, and N. Elhami-Khorasani. Streamlined wildland-urban interface fire tracing (swuift): Modeling wildfire spread in communities. *Environmental Modelling & Software*, 143:105097, 2021.

A. B. Massada, V. C. Radeloff, S. I. Stewart, and T. J. Hawbaker. Wildfire risk in the wildland–urban interface: a simulation study in northwestern wisconsin. *Forest Ecology and Management*, 258(9):1990–1999, 2009.

L. Mazzaro, E. Koo, D. Muñoz-Esparza, J. Lundquist, and R. Linn. Random force perturbations: A new extension of the cell perturbation method for turbulence generation in multiscale atmospheric boundary layer simulations. *Journal of Advances in Modeling Earth Systems*, 11(7):2311–2329, 2019.

L. J. Mazzaro, D. Muñoz-Esparza, J. K. Lundquist, and R. R. Linn. Nested mesoscale-to-les modeling of the atmospheric boundary layer in the presence of under-resolved convective structures. *Journal of Advances in Modeling Earth Systems*, 9(4):1795–1810, 2017.

F. Mesinger, G. DiMego, E. Kalnay, K. Mitchell, P. C. Shafran, W. Ebisuzaki, D. Jović, J. Woollen, E. Rogers, E. H. Berbery, et al. North american regional reanalysis. *Bulletin of the American Meteorological Society*, 87(3):343–360, 2006.

N. Mietkiewicz, J. K. Balch, T. Schoennagel, S. Leyk, L. A. St. Denis, and B. A. Bradley. In the line of fire: consequences of human-ignited wildfires to homes in the us (1992–2015). *Fire*, 3(3):50, 2020.

A. Miranda, J. Carrasco, M. González, C. Pais, A. Lara, A. Altamirano, A. Weintraub, and A. D. Syphard. Evidence-based mapping of the wildland-urban interface to better identify human communities threatened by wildfires. *Environmental Research Letters*, 15 (9):094069, 2020.

J. Mirocha, J. Lundquist, and B. Kosović. Implementation of a nonlinear subfilter turbulence stress model for large-eddy simulation in the advanced research wrf model. *Monthly Weather Review*, 138(11):4212–4228, 2010.

J. Mirocha, B. Kosović, and G. Kirkil. Resolved turbulence characteristics in large-eddy simulations nested within mesoscale simulations using the weather research and forecasting model. *Monthly Weather Review*, 142(2):806–831, 2014.

E. J. Mlawer, S. J. Taubman, P. D. Brown, M. J. Iacono, and S. A. Clough. Radiative transfer for inhomogeneous atmospheres: Rrtm, a validated correlated-k model for the longwave. *Journal of Geophysical Research: Atmospheres*, 102(D14):16663–16682, 1997.

N. Mölders. Suitability of the weather research and forecasting (wrf) model to predict the june 2005 fire weather for interior alaska. *Weather and Forecasting*, 23(5):953–973, 2008.

A. S. Monin and A. M. Obukhov. Basic laws of turbulent mixing in the surface layer of the atmosphere. *Contrib. Geophys. Inst. Acad. Sci. USSR*, 151(163):e187, 1954.

N. Mukul Tewari, M. Tewari, F. Chen, W. Wang, J. Dudhia, M. LeMone, K. Mitchell, M. Ek, G. Gayno, J. Wegiel, et al. Implementation and verification of the unified noah land surface model in the wrf model (formerly paper number 17.5). In *Proceedings of the 20th Conference on Weather Analysis and Forecasting/16th Conference on Numerical Weather Prediction, Seattle, WA, USA*, volume 14, 2004.

D. Muñoz-Esparza and B. Kosović. Generation of inflow turbulence in large-eddy simulations of nonneutral atmospheric boundary layers with the cell perturbation method. *Monthly Weather Review*, 146(6):1889–1909, 2018.

D. Muñoz-Esparza, B. Kosović, J. Mirocha, and J. van Beeck. Bridging the transition from mesoscale to microscale turbulence in numerical weather prediction models. *Boundary-layer meteorology*, 153(3):409–440, 2014.

D. Muñoz-Esparza, B. Kosović, J. Van Beeck, and J. Mirocha. A stochastic perturbation method to generate inflow turbulence in large-eddy simulation models: Application to neutrally stratified atmospheric boundary layers. *Physics of Fluids*, 27(3):035102, 2015.

D. Muñoz-Esparza, B. Kosović, P. A. Jiménez, and J. L. Coen. An accurate fire-spread algorithm in the weather research and forecasting model using the level-set method. *Journal of Advances in Modeling Earth Systems*, 10(4):908–926, 2018.

M. Nakanishi and H. Niino. An improved mellor–yamada level-3 model with condensation physics: Its design and verification. *Boundary-layer meteorology*, 112(1):1–31, 2004.

M. Nakanishi and H. Niino. An improved mellor–yamada level-3 model: Its numerical stability and application to a regional prediction of advection fog. *Boundary-Layer Meteorology*, 119(2):397–407, 2006.

M. Nakata, I. Sano, S. Mukai, and A. Kokhanovsky. Characterization of wildfire smoke over complex terrain using satellite observations, ground-based observations, and meteorological models. *Remote Sensing*, 14(10):2344, 2022.

D. G. Neary. Recent megafires provide a tipping point for desertification of conifer ecosystems. In *Conifers-Recent Advances*. IntechOpen, 2022.

S. M. Njuki, C. M. Mannaerts, and Z. Su. Influence of planetary boundary layer (pbl) parameterizations in the weather research and forecasting (wrf) model on the retrieval of surface meteorological variables over the kenyan highlands. *Atmosphere*, 13(2):169, 2022.

M. Pamiès, P.-E. Weiss, E. Garnier, S. Deck, and P. Sagaut. Generation of synthetic turbulent inflow data for large eddy simulation of spatially evolving wall-bounded flows. *Physics of fluids*, 21(4):045103, 2009.

J. Pereira, P. M. Alexandre, M. L. Campagnolo, A. Bar-Massada, V. C. Radeloff, and P. C. Silva. Defining and mapping the wildland-urban interface in portugal. *Parte: http://hdl. handle. net/10316.2/44517*, 2018.

R. V. Platt. The wildland–urban interface: evaluating the definition effect. *Journal of Forestry*, 108(1):9–15, 2010.

V. C. Radeloff, R. B. Hammer, P. R. Voss, A. E. Hagen, D. R. Field, and D. J. Mladenoff. Human demographic trends and landscape level forest management in the northwest wisconsin pine barrens. *Forest Science*, 47(2):229–241, 2001.

V. C. Radeloff, R. B. Hammer, and S. I. Stewart. Rural and suburban sprawl in the us midwest from 1940 to 2000 and its relation to forest fragmentation. *Conservation biology*, 19(3):793–805, 2005a.

V. C. Radeloff, R. B. Hammer, S. I. Stewart, J. S. Fried, S. S. Holcomb, and J. F. McKeefry. The wildland–urban interface in the united states. *Ecological applications*, 15(3):799–805, 2005b.

V. C. Radeloff, D. P. Helmers, H. A. Kramer, M. H. Mockrin, P. M. Alexandre, A. Bar-Massada, V. Butsic, T. J. Hawbaker, S. Martinuzzi, A. D. Syphard, et al. Rapid growth of the us wildland-urban interface raises wildfire risk. *Proceedings of the National Academy of Sciences*, 115(13):3314–3319, 2018.

M. Raphael. The santa ana winds of california. *Earth Interactions*, 7(8):1–13, 2003.

R. C. Rothermel. *A mathematical model for predicting fire spread in wildland fuels*, volume 115. Intermountain Forest & Range Experiment Station, Forest Service, US ..., 1972.

J. H. Scott, M. P. Thompson, and J. W. Gilbertson-Day. Examining alternative fuel management strategies and the relative contribution of national forest system land to wildfire risk to adjacent homes–a pilot assessment on the sierra national forest, california, usa. *Forest Ecology and Management*, 362:29–37, 2016.

K. C. Short. Spatial wildfire occurrence data for the united states, 1992-2015 [fpa_fod_20170508]. fort collins, co: Forest service research data archive, 2017.

W. C. Skamarock, J. B. Klemp, J. Dudhia, D. O. Gill, D. M. Barker, W. Wang, and J. G. Powers. A description of the advanced research wrf version 2. Technical report, National Center For Atmospheric Research Boulder Co Mesoscale and Microscale . . . , 2005.

W. C. Skamarock, J. B. Klemp, J. Dudhia, D. O. Gill, D. M. Barker, W. Wang, and J. G. Powers. A description of the advanced research wrf version 3. ncar technical note-475+ str. *National Center for Atmospheric Research: Boulder, CO, USA*, 2008.

W. C. Skamarock, J. B. Klemp, J. Dudhia, D. O. Gill, Z. Liu, J. Berner, W. Wang, J. G. Powers, M. G. Duda, D. M. Barker, et al. A description of the advanced research wrf model version 4. *National Center for Atmospheric Research: Boulder, CO, USA*, 145:145, 2019.

A. Spille-Kohoff and H.-J. Kaltenbach. Generation of turbulent inflow data with a prescribed shear-stress profile. Technical report, TECHNISCHE UNIV BERLIN (GERMANY) HERMANN-FOTTINGER INST FUR STROMUNGSMECHANIK, 2001.

S. L. Stephens and L. W. Ruth. Federal forest-fire policy in the united states. *Ecological applications*, 15(2):532–542, 2005.

S. L. Stephens, B. M. Collins, E. Biber, and P. Z. Fulé. Us federal fire and forest policy: emphasizing resilience in dry forests. *Ecosphere*, 7(11):e01584, 2016.

S. I. Stewart, V. C. Radeloff, and R. B. Hammer. Characteristics and location of the wildland-urban interface in the united states. In *2 nd International Wildland wildfire Ecology and wildfire Management Congress. Orlando, Florida*, 2003.

S. I. Stewart, V. C. Radeloff, R. B. Hammer, and T. J. Hawbaker. Defining the wildland–urban interface. *Journal of Forestry*, 105(4):201–207, 2007.

S. I. Stewart, B. Wilmer, R. B. Hammer, G. H. Aplet, T. J. Hawbaker, C. Miller, and V. C. Radeloff. Wildland-urban interface maps vary with purpose and context. *Journal of Forestry*, 107(2):78–83, 2009.

R. B. Stull. *An introduction to boundary layer meteorology*, volume 13. Springer Science & Business Media, 1988.

A. L. Sullivan. Wildland surface fire spread modelling, 1990–2007. 1: Physical and quasi-physical models. *International Journal of Wildland Fire*, 18(4):349–368, 2009.

A. D. Syphard, H. Rustigian-Romsos, M. Mann, E. Conlisk, M. A. Moritz, and D. Ackerly. The relative influence of climate and housing development on current and projected future fire patterns and structure loss across three california landscapes. *Global Environmental Change*, 56:41–55, 2019.

W. Teie. Fire in the west: The wildland/urban interface problem—a report to the council of western state foresters, 1999.

L. H. Thapa, X. Ye, J. W. Hair, M. A. Fenn, T. Shingler, S. Kondragunta, C. Ichoku, R. Dominguez, L. Ellison, A. J. Soja, et al. Heat flux assumptions contribute to overestimation of wildfire smoke injection into the free troposphere. *Communications Earth & Environment*, 3(1):1–11, 2022.

K. Varga, C. Jones, A. Trugman, L. M. Carvalho, N. McLoughlin, D. Seto, C. Thompson, and K. Daum. Megafires in a warming world: What wildfire risk factors led to california's largest recorded wildfire. *Fire*, 5(1):16, 2022.

H. J. Vaux. *Forestry's hotseat: The urban/forest interface.* National Emergency Training Center, 1982.

B. Wang, A. C. Spessa, P. Feng, X. Hou, C. Yue, J.-J. Luo, P. Ciais, C. Waters, A. Cowie, R. H. Nolan, et al. Extreme fire weather is the major driver of severe bushfires in southeast australia. *Science Bulletin*, 67(6):655–664, 2022.

N. P. Wedi. Increasing horizontal resolution in numerical weather prediction and climate simulations: illusion or panacea? *Philosophical Transactions of the Royal Society A: Mathematical, Physical and Engineering Sciences*, 372(2018):20130289, 2014.

A. L. Westerling, D. R. Cayan, T. J. Brown, B. L. Hall, and L. G. Riddle. Climate, santa ana winds and autumn wildfires in southern california. *Eos, Transactions American Geophysical Union*, 85(31):289–296, 2004.

B. Wilmer and G. Aplet. Targeting the community fire planning zone: Mapping matters. *The Wilderness Sociey: Washington, DC, USA*, 2005.

Z.-T. Xie and I. P. Castro. Efficient generation of inflow conditions for large eddy simulation of street-scale flows. *Flow, turbulence and combustion*, 81(3):449–470, 2008.

F. J. Zajaczkowski, S. E. Haupt, and K. J. Schmehl. A preliminary study of assimilating numerical weather prediction data into computational fluid dynamics models for wind prediction. *Journal of Wind Engineering and Industrial Aerodynamics*, 99(4):320–329, 2011.

J. Zhong, X. Cai, and Z.-T. Xie. Implementation of a synthetic inflow turbulence generator in idealised wrf v3. 6.1 large eddy simulations under neutral atmospheric conditions. *Geoscientific Model Development*, 14(1):323–336, 2021.

Appendix A

Examining the existing definitions of wildland-urban interface for California

Site type	BR	WBA	OA	POWB	POAW
WUI-A	0	19,517.675	796.500	4.08	2.95
	1	32,373.264	1,851.402	5.72	6.85
	2	45,477.682	2,998.147	6.59	11.09
	3	60,238.204	4,319.187	7.17	15.98
	4	76,904.458	5,858.389	7.62	21.68
	5	95,529.777	7,580.403	7.94	28.05
WUI-B	0	19,517.675	153.604	0.79	1.60
	1	32,373.264	555.739	1.72	5.80
	2	45,477.682	934.399	2.06	9.75
	3	60,238.204	71,380.736	2.29	14.41
	4	76,904.458	1,874.200	2.44	19.56
	5	95,529.777	2,447.613	2.56	25.55

Table A.1: Percentage overlap of wildfire burned area and WUI-A and WUI-B with varying buffer distances from wildfire perimeter. Here, BR - buffer radius in km; WBA - Wildfire Buffer Area (km^2); OA - Overlapping Area (km^2); POWB - Percentage of Overlap in Wildfire Buffers (%); POAW - Percentage of Overlapped area in WUI (%)

Site type	BR	WBA	OA	IPWB	POWBA	POWB
WUI-A	0	27,025.683	796.500	3.65(12/329)	4.08	2.95
	1	80,066.343	3,372.233	21.88(72/329)	17.28	4.21
	2	122,611.267	5,732.952	37.99(125/329)	29.37	4.68
	3	159,640.146	7,757.174	48.33(159/329)	39.74	4.86
	4	192,297.277	9,467.068	57.14(188/329)	48.50	4.92
	5	221,335.796	10,984.716	65.96(217/329)	56.28	4.96
WUI-B	0	9,606.273	153.604	1.21(4/329)	0.79	1.60
	1	54,204.707	1,706.335	8.81(29/329)	8.74	3.15
	2	87,920.876	3,316.826	22.19(73/329)	16.99	3.77
	3	117,422.931	4,727.220	31.61(104/329)	24.22	4.03
	4	143,964.111	5,925.639	40.12(132/329)	30.36	4.12
	5	168,252.547	7,017.430	45.59(150/329)	35.95	4.17

Table A.2: The overlap of wildfire burned area (19,517.675 km^2) and wildfire ignition points with different buffer distances from WUI-A and WUI-B. Here, BR - Buffer Radius (km); WBA - WUI Buffer Area (km^2); OA - Overlapping Area (km^2); IPWB - Ignition Points within WUI Buffers (%); POWBA - Percentage of Overlap in Wildfire Burned Areas (%); POWB - Percentage of Overlap in WUI Buffers (%)

Elevation(m)	**1**	**2**	**3**	**4**	**5**	**6**	**7**	**8**	**9**
	0-100	100-200	200-300	300-400	400-500	500-600	600-700	700-800	800-4410
WUI-A	18.50	15.70	10.40	7.70	9.20	6.30	5.40	5.40	21.40
WUI-B	20.17	18.37	12.36	8.74	10.04	5.84	4.28	4.61	15.59

Table A.3: Percentage overlap of WUI on different elevation ranges (classes) over California (CA) at 30 m resolution.

Rugosity	**1.0**	**1.0 - 1.1**	**1.1 - 1.3**	**1.3 - 1.5**	**1.5 - 2.0**	**>2.0**
WUI-A (%)	0.40	92.71	6.73	0.16	0.01	0.00
WUI-B (%)	0.20	97.16	2.60	0.027	0.00	0.00

Table A.4: Overlap of WUI and rugosity for CA.

Slope (degree)	**0-30**	**30-60**	**60-86**
WUI-A (%)	92.72	2.27	0.00
WUI-B (%)	99.4	0.60	0.00

Table A.5: Overlap of WUI and slope for CA.

Aspect (direction)	**0-90**	**90-180**	**180-270**	**270-360**
WUI-A (%)	23.82	23.61	29.17	23.40
WUI-B (%)	23.40	30.00	23.40	23.20

Table A.6: Overlap of WUI and aspect for CA.

Site type	BR	WBA	IPWB	PIPWB
WUI-A	0	27025.683	20656	32.42
	1	80066.343	38341	60.17
	2	122611.267	44535	69.89
	3	159640.146	48737	76.48
	4	192297.277	51885	81.42
	5	221335.796	54235	85.11
WUI-B	0	9606.273	11792	18.51
	1	54204.707	32474	50.96
	2	87920.876	39912	62.63
	3	117422.931	44559	69.93
	4	143964.111	48211	75.66
	5	168252.547	50785	79.70

Table A.7: The overlap of small wildfire ignition points with different buffer distances surrounding WUI-A and WUI-B. Here, BR - Buffer Radius (km); WBA - WUI Buffer Area (km^2); IPWB - Ignition Points within WUI Buffers; PIPWB - Percentage of Ignition Points within WUI Buffers (%)

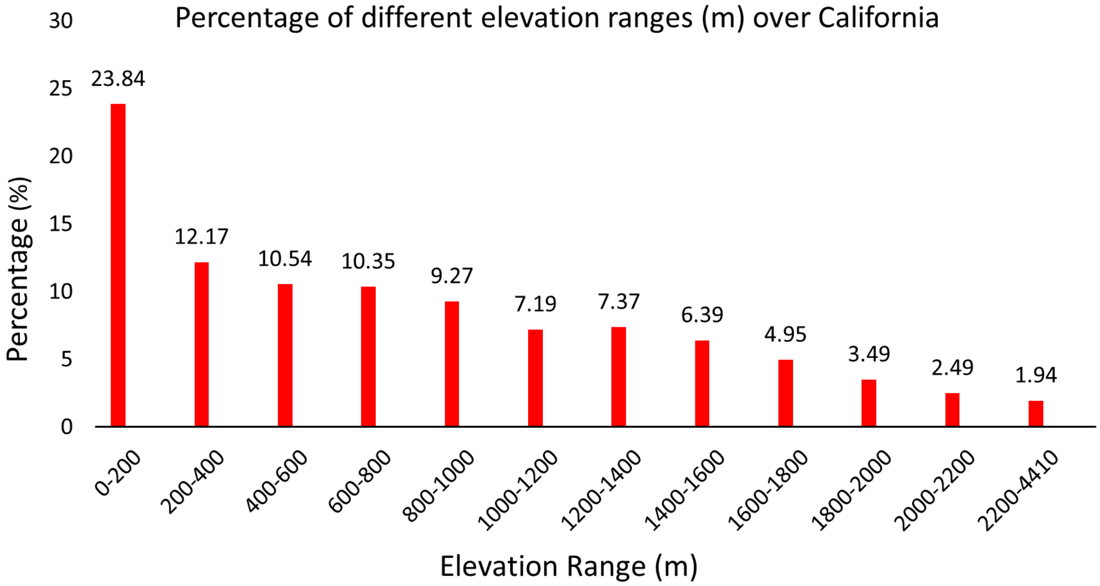

Figure A.1: Percentage of different elevation (30 m) ranges over California. It shows the percentage of different elevation ranges over CA are maximum in 0-200 m followed by 200-400 m. More than half of the regions in CA are on complex topography having elevation values greater than 600 m and only 46.36 % of landforms lie within 600 m of elevation.

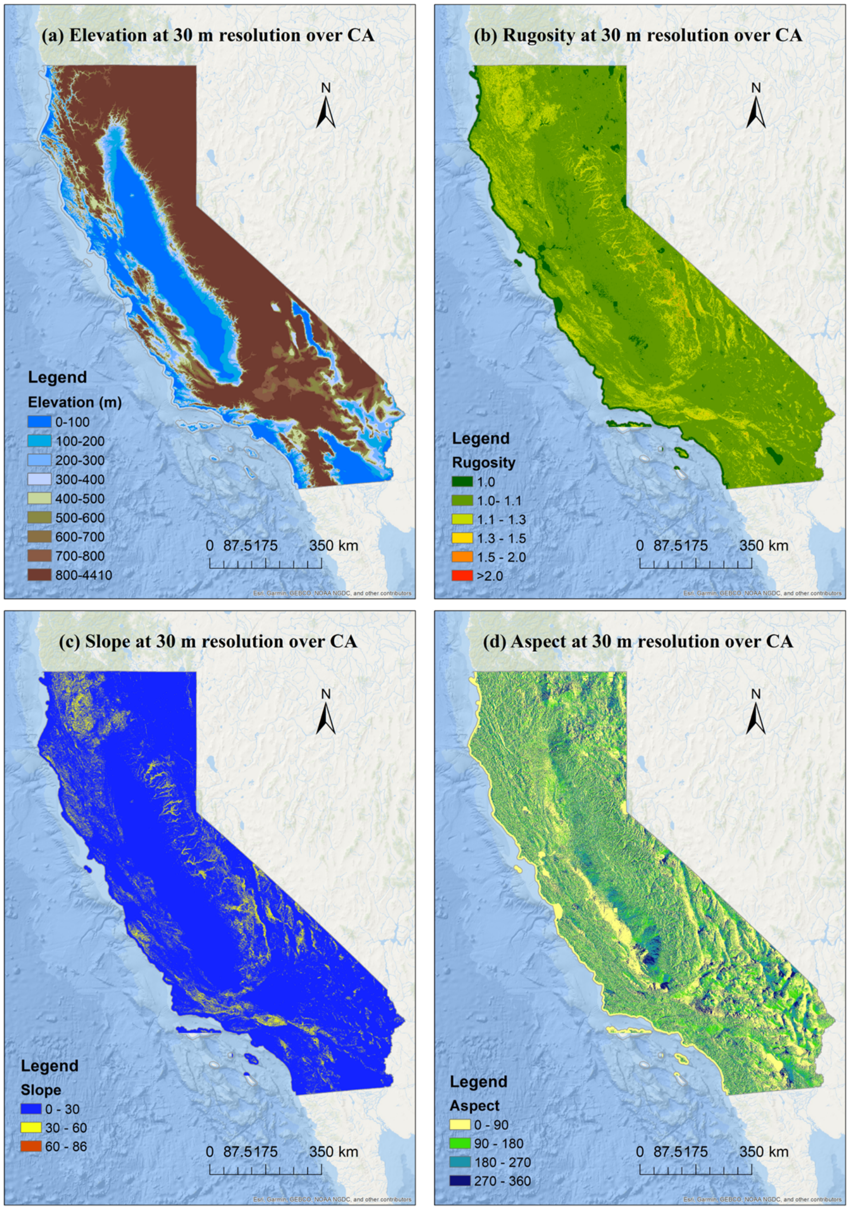

Figure A.2: The figure on the top left panel (a) shows spatial variation of topography with different elevation ranges. The legend shows different ranges of elevation for the entire landform over CA and the magnitude of these values lie between 0 m to 4410 m, and also represented with different classes from 1 to 9 as can be referred to Table A.4, top left panel (b) shows the spatial distribution of rugosity (surface roughness) over California at 30 m resolution. Legend shows the values of rugosity from 1 to more than 2. Spatial distribution of slope has been shown in the bottom left panel (c) and was calculated using 4-cell method over California at 30 m resolution. Here, legend represents the value of slope in degrees. The Figure 2.8d on the bottom right panel (d) shows the spatial distribution of the aspect calculated using 4-cell method over California at 30 m resolution. Legend shows the values of aspect lying in the four quadrants.

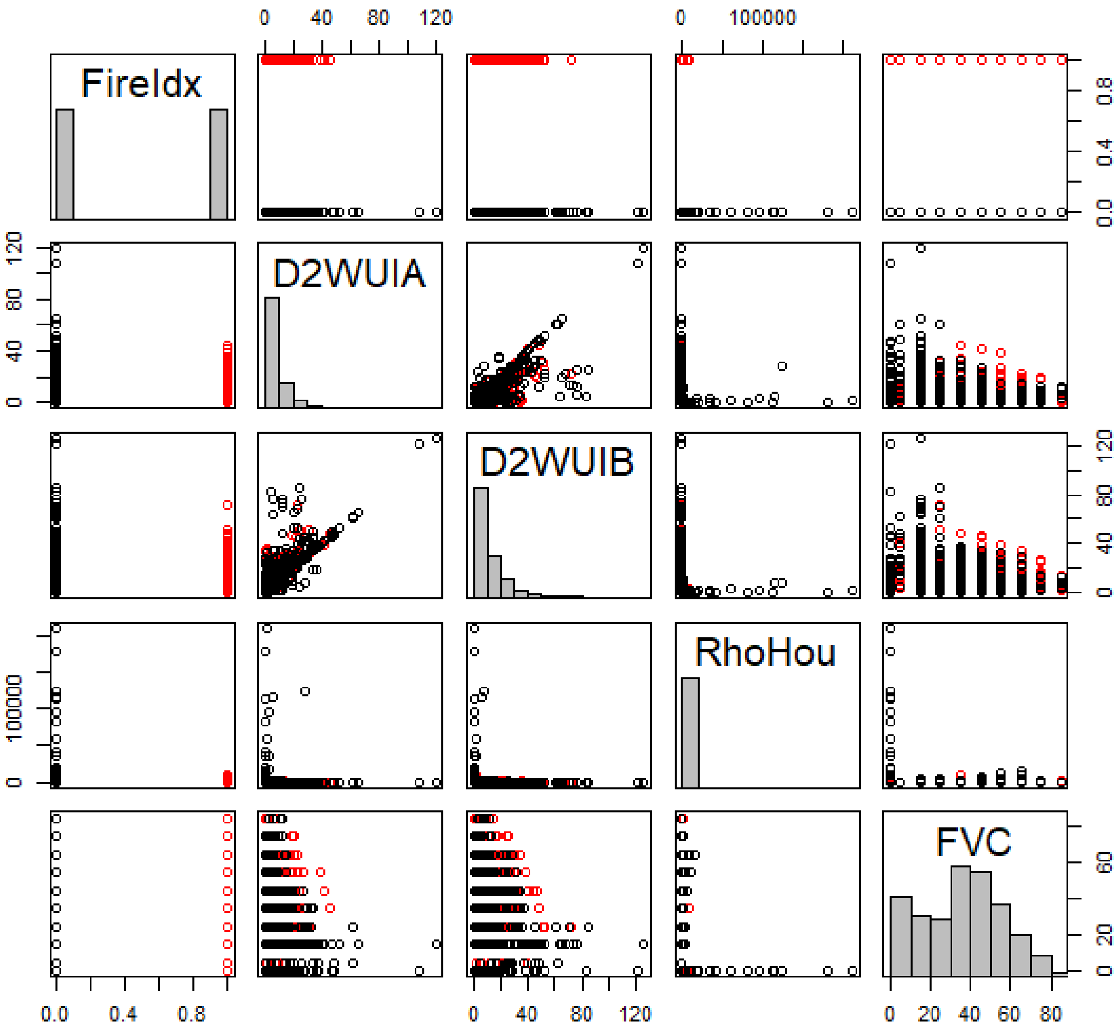

Figure A.3: Pairs plot of current parameters in WUI definition: large wildfires: Fire Index (FireIdx) represents the presence/absence of large wildfires; distance to WUI-A (D2WUIA) and distance to WUI-B (D2WUIB) represent the distance from fire and random points to WUI areas; housing density (RhoHou) represents the number of houses per km^2 in each Census blocks; fuel vegetation cover (FVC) represents the percentage cover of vegetation. The red points represent large wildfire centroid points and clack points represent the random non-fire points.

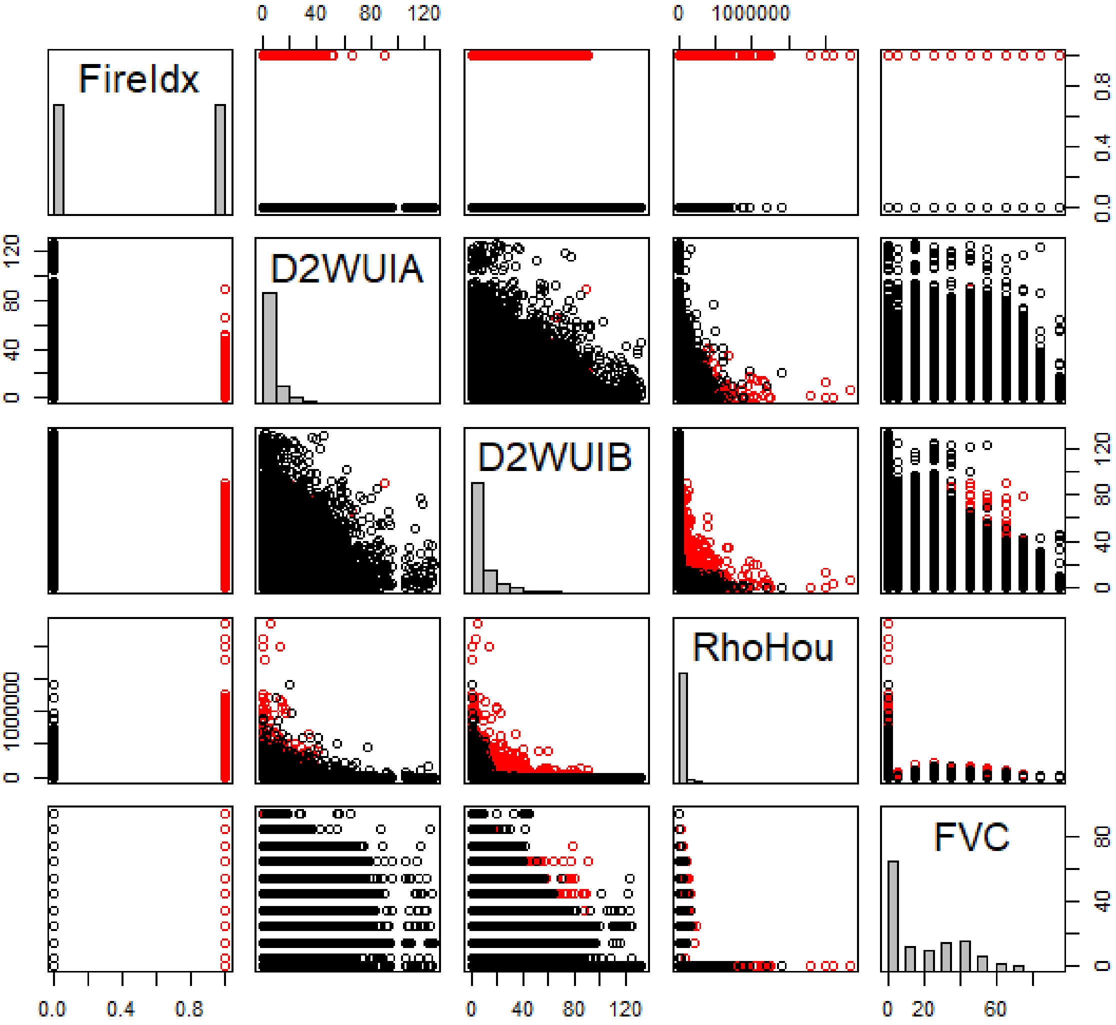

Figure A.4: Pairs plot of current parameters in WUI definition: small wildfires: Fire Index (FireIdx) represents the presence/absence of large wildfires; distance to WUI-A (D2WUIA) and distance to WUI-B (D2WUIB) represent the distance from fire and random points to WUI areas; housing density (RhoHou) represents the number of houses per km^2 in each Census blocks; fuel vegetation cover (FVC) represents the percentage cover of vegetation. The red points represent large wildfire centroid points and clack points represent the random non-fire points.

Appendix B

Mapping the wildland-urban interface in California using a vector-based edge approach

B.1 Additional information on fire occurrence and vegetation data used in this study

We observe that fire occurrence is highest in the northern part of the state and in southern California (Figure 3.2, left panel). Notably, in southern California, the counties of San Diego (SDG) and Kern (KER) each had more than 27 fires from 2010 to 2020. While in the northern part of California, Siskiyou (SIS) County had more than 24 fires during the same period. Strong wind events, more specifically Diablo winds in northern California and Santa Ana winds in southern California, are the main drivers for the larger and more devastating wildfires. Furthermore, human ignition is one of the most significant factors in the last few decades for a majority of the deadliest fires. A few counties had no or very few wildfire events during 2010-2020. This map clearly shows that the majority of southern California is covered by shrubland vegetation, whereas the dominant land cover type in the north is evergreen forest and shrubland. Furthermore, the variability in land cover type is greater in the northern counties of California than in the southern regions. Overall, shrubland is the most common type of vegetation in California. Shrublands are defined as ecosystems with a minimum of 30 % shrub or sub-shrub cover and tree densities of up to 10 trees per hectare (USDA). They are one of the regions where wildfire season lasts the longest [Jolly et al., 2015]. Although characterized by a low fuel density, those available fuels are very dry and therefore, fire spreads fast in shrublands [Bond and Keane, 2017]. The white color bar in the right panel of Figure 3.2 also reflects water and other land cover types that are not classified as wildland vegetation while mapping vector-based WUI.

B.2 Additional information on statistical analysis

In this approach the null hypothesis is that the dataset is sampled from the chosen distribution and a p-value larger than the significance level 0.05 indicates that the null hypothesis cannot be rejected in favor of the alternate hypothesis. Apart from p-value, there are other parameters that can be used to check whether or not the results of a statistical analysis are adequate. For example, the location and scale of a distribution also tells us about the data structure. The scale parameter describes how spread out the data values are, while the location parameter describes how large the data values are. However, some of the distributions like ‘weibull’ and ‘gamma’ do not have these parameters (see Table B.2 and Table B.3 in supplementary materials). Therefore, we must check for the ‘shape’ parameter, which is an outcome of these distributions. The shape parameter describes how the data is spread. In general, a larger scale results in a more spread-out distribution. In this study, we used a suitable number of datasets (492 fires between 2010 and 2020) to perform the statistical analysis in both direct and indirect WUI (see Table B.2 and Table B.3 in supplementary materials). Therefore, the conclusion of our results based on *p*-value is adequate and acceptable. As we can see in the bottom panel of Figure 3.7, lognormal with three parameters is also the best fit curve in the case of indirect WUI.

Distance	**No.(2010-2020)**		**Percentage(%)**	
-	Indirect	Direct	Direct	Direct
0-1	75	157	15.2	31.9
1-2	103	161	20.9	32.7
2-3	79	72	16.1	14.6
3-4	50	52	10.2	10.6
4-5	46	19	9.4	3.9
>5	139	31	28.3	6.3

Table B.1: Statistical summary table showing distance of fire ignition points with respect to direct and indirect WUI in California.

Descriptive Statistics and curve fitting summary table for direct WUI									
	Count	Mean	StDev	Median	Min	Max	Skew	Kurt	
	492	1.982	1.759	1.545	0.00540	13.46	2.346	9.249	
Distribution	**Loc**	**Shap**	**Sca**	**Thres**	**LogLike**	**AD**	***p*-Val**	**LRT**	**AIC**
Gamma		1.381	1.435		-814.2	0.529	0.212		1632.4
Gamma-3P		1.387	1.430		-814.2	0.515	0.225	0.893	1634.4
Weibull		1.198	2.110	-0.00139	-815.9	0.846	0.031		1635.8
Weibull-3P		1.191	2.102		-815.7	0.859	0.029	0.542	1637.4
LogNormal-3P	0.583		0.713	0.00367	-818.5	0.535	0.170	0.000	1643.1
LogLogistic-3P	0.512		0.451	-0.311	-825.1	1.125	<0.005	0.000	1656.1
Exponential-2P			1.977	-0.187	-827.2	7.201	<0.001	0.101	1658.4
Exponential			1.982		-828.6	7.140	<0.001		1659.1
LogLogistic	0.366		0.551		-833.3	2.674	<0.005		1670.6
LogNormal	0.280		1.033		-852.1	5.978	0.000		1708.3
Largest-EV	1.279		1.099		-853.1	3.964	<0.01		1710.3
Logistic	1.735		0.860		-923.8	10.64	<0.005		1851.5
Normal	1.982		1.757		-975.5	19.23	0.000		1955.1
Smallest-EV	3.012		2.926		-1193.4	57.42	<0.01		2390.7

Table B.2: Statistical analysis using 14 different curve fittings to choose the best fit curve for the distribution of the distance between wildfire ignition points and direct WUI line segments (fires from 2010-2020). Here, Loc-location; Shap-shape; Sca-scale; Thres-threshold; LogLike-log likelihood; EV-extreme value; 3P-three parameter.

Descriptive Statistics and curve fitting summary table for indirect WUI									
	Count	Mean	StDev	Median	Min	Max	Skew	Kurt	
	492	4.251	4.546	2.792	0.00729	36.66	2.818	11.21	
Distribution	**Loc**	**Shap**	**Sca**	**Thres**	**LogLike**	**AD**	**p-Val**	**LRT**	**AIC**
Gamma		1.210	3.512		-1198.6	2.449	<0.005		2401.3
Gamma-3P		1.201	3.535	0.00444	-1198.5	2.413	<0.005	0.626	2403.1
Weibull		1.069	4.373		-1202.0	3.024	<0.01		2408.1
LogNormal-3P	1.107		0.892	-0.215	-1186.8	0.155	0.956	0.000	2379.5
LogLogistic-3P	1.050		0.550	-0.0677	-1191.1	0.544	0.120	0.087	2388.2
Exponential-2P			4.243	0.00729	-1203.1	4.176	<0.001	0.194	2410.2
Exponential			4.251		-1204.0	4.082	<0.001		2409.9
LogLogistic	1.050		0.550	-0.0677	-1191.1	0.544	0.120	0.087	2388.2
LogNormal	0.980		1.043		-1201.2	1.281	0.002		2406.5
Largest-EV	2.571		2.464		-1271.1	10.76	<0.01		2546.1
Logistic	3.478		2.035		-1362.9	18.61	<0.005		2729.8
Normal	4.251		4.542		-1442.7	34.09	0.000		2889.3
Smallest-EV	6.979		7.798		-1674.6	71.63	<0.01		3353.3

Table B.3: Statistical analysis using 14 different curve fittings to choose the best fit curve for the distribution of the distance between wildfire ignition points and indirect WUI line segments (fires from 2010-2020). The Weibull - Three Parameter distribution did not converge on a solution and therefore not included in this table. Here, Loc-location; Shap-shape; Sca-scale; Thres-threshold; LogLike-log likelihood; EV-extreme value; 3P-three parameter.

Figure B.1: Zoomed in image of Figure 2, highlight the empty areas near indirect WUI where there is neither vegetation nor building.

Appendix C

Evaluating the performance of the WRF model in simulating winds and surface meteorology during a Southern California wildfire event

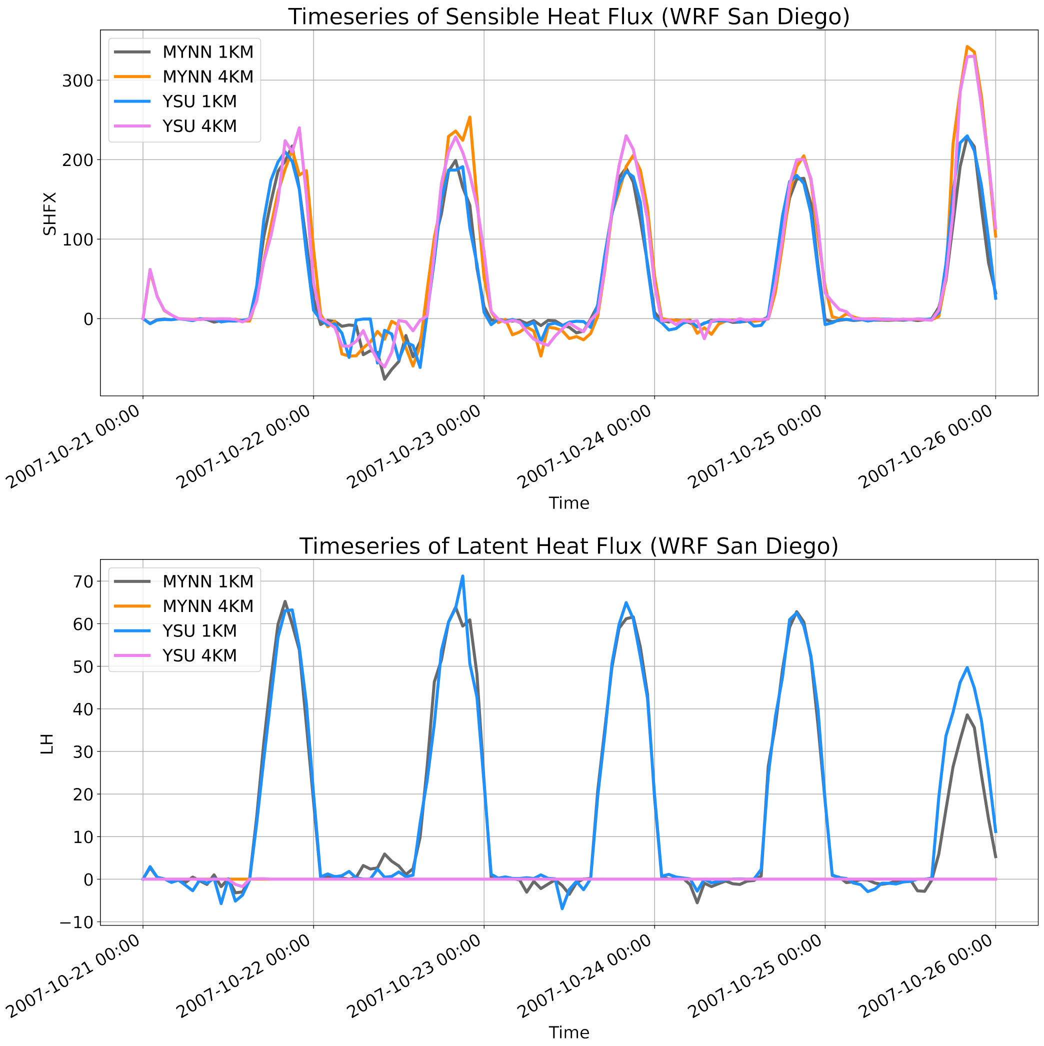

Figure C.1: Timeseries of sensible and latent heat flux $[Wm^{-2}]$ at site 6001 (also abbreviated as San Diego in this chapter) are shown in the top and bottom panels respectively.

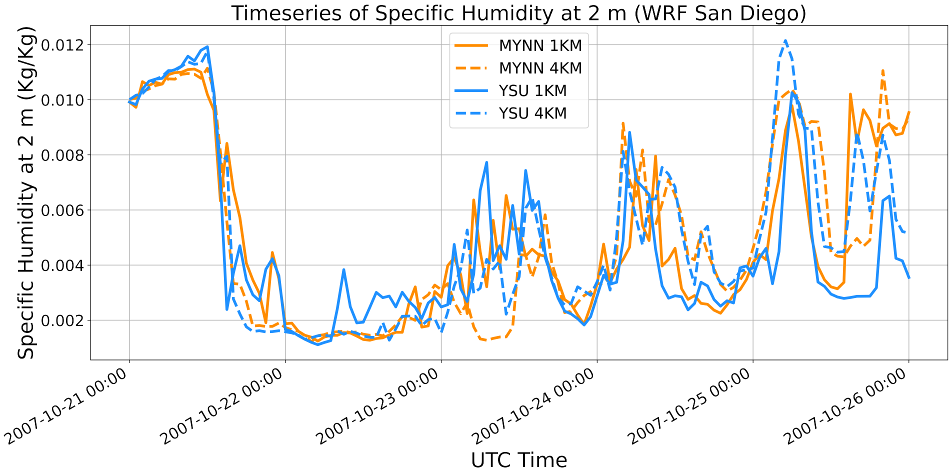

Figure C.2: Same as Figure C.1 for specific humidity at 2 m.

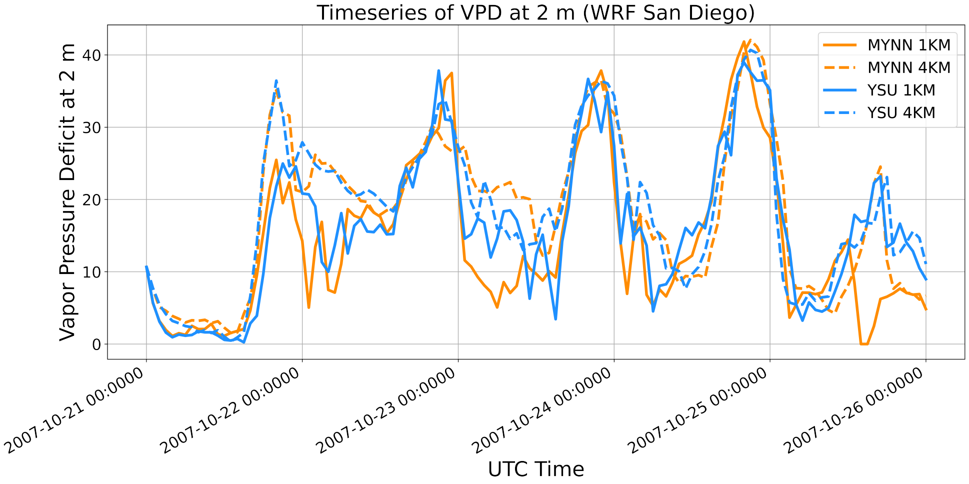

Figure C.3: Same as Figure C.1 for vapor pressure deficit (VPD) at 2 m.

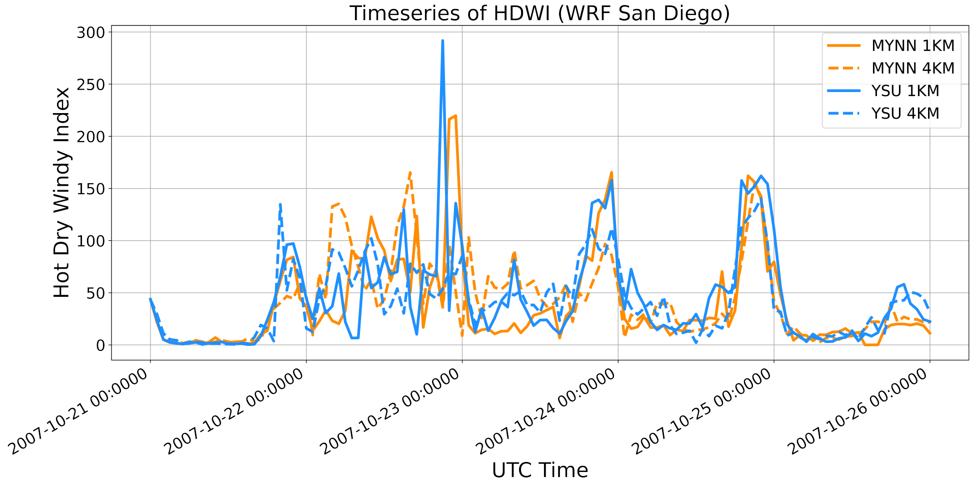

Figure C.4: Same as Figure C.1 for hot dry windy index (HDWI)

Appendix D

Impact of momentum perturbation on convective boundary layer turbulence

D.1 Effects of the spatial averaging domain

D.1.1 Effects of the spatial averaging domain

Heat flux ($\overline{w'\theta'}$) profiles are not similar in all the cases when we apply SCPM-M with higher amplitudes of forces. As it is shown in Figure 5.7(a and b), the Ktop34H starts diverging from other SCPM-M cases at 75 m and continued to do so all the way to the inversion layer. Also, the Ktop34H produces highest entrainment (around 27 $\mathrm{kKms^{-1}}$) at the capping inversion (600 m) as compared to Ktop54H, Ktop88H, and No-SCPM.

Heat fluxes ($\overline{w'\theta'}$) are same up to the inversion layer (600 m) for all the simulations with lower and medium amplitude SCPM-M cases (Figure 5.7(c)). At the inversion layer, entrainment is highest (around 25 $\mathrm{kKms^{-1}}$) for the Ktop88H and the same holds true for the Ktop54. In the case of Ktop34H, when we apply SCPM-M at the half of the boundary layer (303 m), entrainment is higher (around 20 $\mathrm{kKms^{-1}}$) than the Ktop54H and Ktop88H, but lower than the No-SCPM. However, heat fluxes ($\overline{w'\theta'}$) from the surface up to 200 m are almost equal in all the SCPM-M cases when we apply it with lower amplitude for Ktop34L, Ktop54L, and Ktop88L. Therefore, when comparing the top and bottom panels, we can see that while applying SCPM-M with higher forcing amplitudes below the boundary layer, Ktop34H produces highest heat flux ($\overline{w'\theta'}$) and is suitable for several applications.

Similar to the heat flux ($\overline{w'\theta'}$) profiles, we compute the momentum flux ($\overline{u'w'}$) profiles as shown in Figure 5.7 for the different simulations. The momentum flux ($\overline{u'w'}$), a flow property, is lost to the ground in the boundary layer and therefore, is negative in the boundary layer in all cases Stull [1988] of the simulations. Consequently, when it is multiplied by a negative sign, results in a positive contribution to the variance and TKE. The top left panel shows that when we apply momentum perturbation near (Ktop54H) or below (Ktop34H) the boundary layer, it produces a higher momentum flux ($\overline{u'w'}$) as compared to the case where SCPM-M is applied above (Ktop88H) the boundary layer. Therefore, the turbulent motions are generated and significantly well resolved when SCPM-M is applied within the boundary layer. However, in the case of No-SCPM, we observe highest momentum flux ($\overline{u'w'}$) within 200 m. This was due to the way we performed area averaging in these profiles. More specifically, this is a result of the fact that No-SCPM is unable to capture turbulence generation at the beginning of the inflow boundary and create a fetch, while generating extra turbulence afterwards (above x values of around 6,000 m). Since we are taking the area average over that specific values over the x axis (6,000 m to the end of the domain), it is expected that we would observe a large momentum flux ($\overline{u'w'}$).

On comparing top and bottom panels while we implement SCPM-M with higher and lower amplitudes, we observe that at the lower and medium amplitudes, SCPM-M produces similar profiles of momentum flux ($\overline{u'w'}$) in the convective boundary layer (5.7(d)). At the higher amplitudes, the SCPM-M generates slightly different momentum fluxes ($\overline{u'w'}$) especially in the lower atmosphere, closer to the surface (i.e., up to 200 m). We also find that the Ktop34H loses the maximum momentum flux (negative) as compared to the Ktop54H and Ktop88H. Therefore, we can observe that applying SCPM-M with higher amplitude below the boundary layer produces turbulence structures that could sufficiently represent the flow characteristics in the lower atmosphere.

We find that the No-SCPM generates extra TKE in the lower atmosphere up to 200 m (5.3 (a and b)) as it produces additional variances and turbulence structures through momentum fluxes ($\overline{u'w'}$) as discussed previously. Furthermore, it starts decreasing above 200 m and its value is decreased by 60% from 200 m to 400 m. It reaches close to zero at 800 m. In addition, it crosses all the SCPM-M cases at 200 m and decreases at the highest rate as compared to all of the other cases (D.4(c and d)).

We find that TKE is different in Ktop34H, Ktop54H, and Ktop88H up to 350 m. In addition, we observe that the Ktop34H produces highest TKE while the Ktop88H produces lowest TKE and Ktop54H generates the TKE that is somewhere between Ktop34H and Ktop88H (D.4(c)). The value of TKE for Ktop34H decreases at a lower rate as compared with the No-SCPM case and it decreases by 60% from 200 m to 600 m where the inversion layer was. Its value decreases at a faster rate above 600 m and it decreases to close to zero at the different heights in the chosen cases of SCPM-M. For instance, it decreases to zero at around 900 m for Ktop34H, while reaches zero at 1,100 m and 1,300 m for Ktop54H and Ktop88H respectively (D.4(c)). On the other hand, in case of SCPM-M with lower amplitudes, a practically equivalent TKE is generated up to 150 m (D.4(b)). Also, from 200 m to 600 m (i.e., within the boundary layer), Ktop34L, Ktop54L, Ktop88L, and Ktop88M dominate the TKE generation (D.4(d)). Furthermore, while observing the TKE profiles above the inversion layer (600 m), we find that the TKE decreases sharply just after 600 m and its value reaches zero at 800 m for all the cases (D.4(d)).

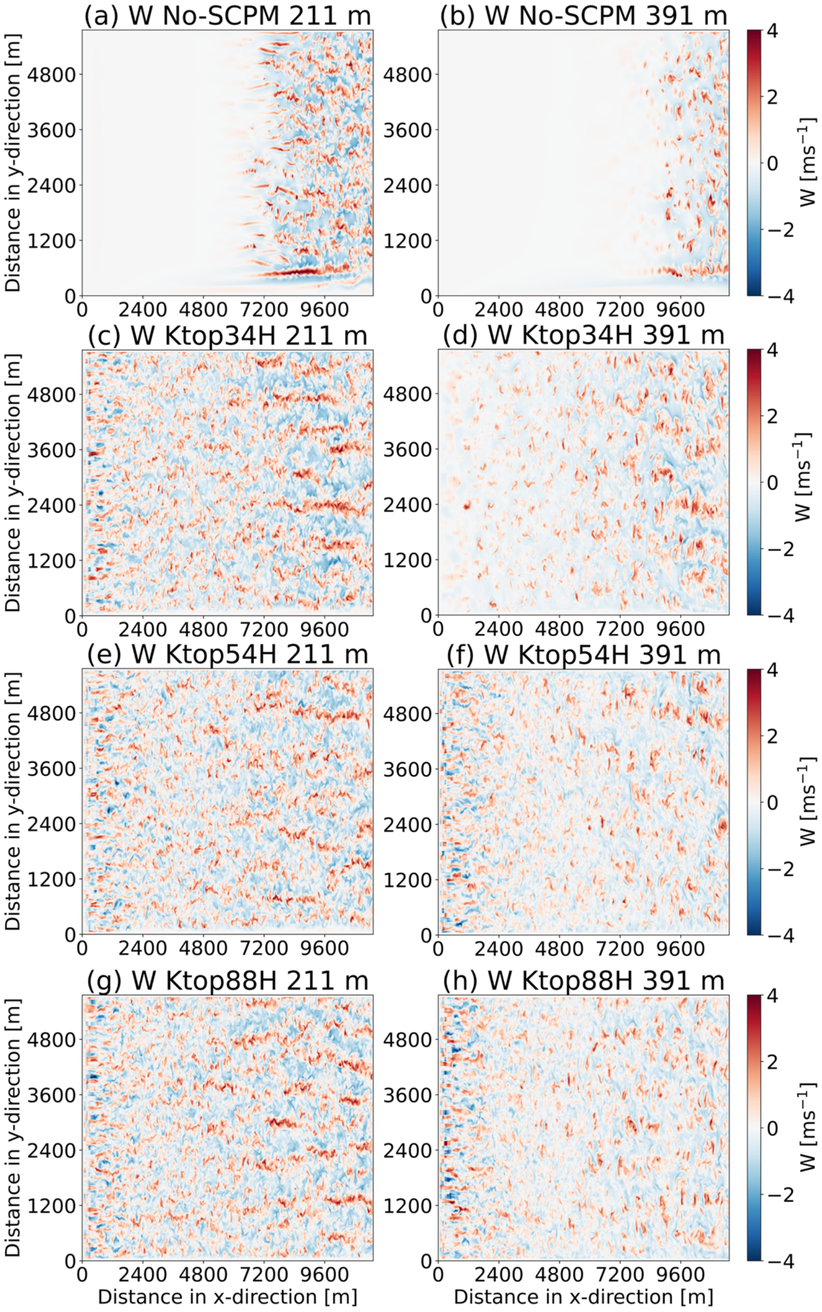

Figure D.1: W component of velocities (ms^{-1}) at two different heights that is at half (level=27, z=211 m) and at two-third (level=37, z=391 m) of the boundary layer height for (a-b) No-SCPM, (c-d) Ktop54H (e-f) Ktop54H (g-h) Ktop88H. Color bar corresponds to the velocity for panels (a) to (h). The domain shown is the inner LES domain used in this study.

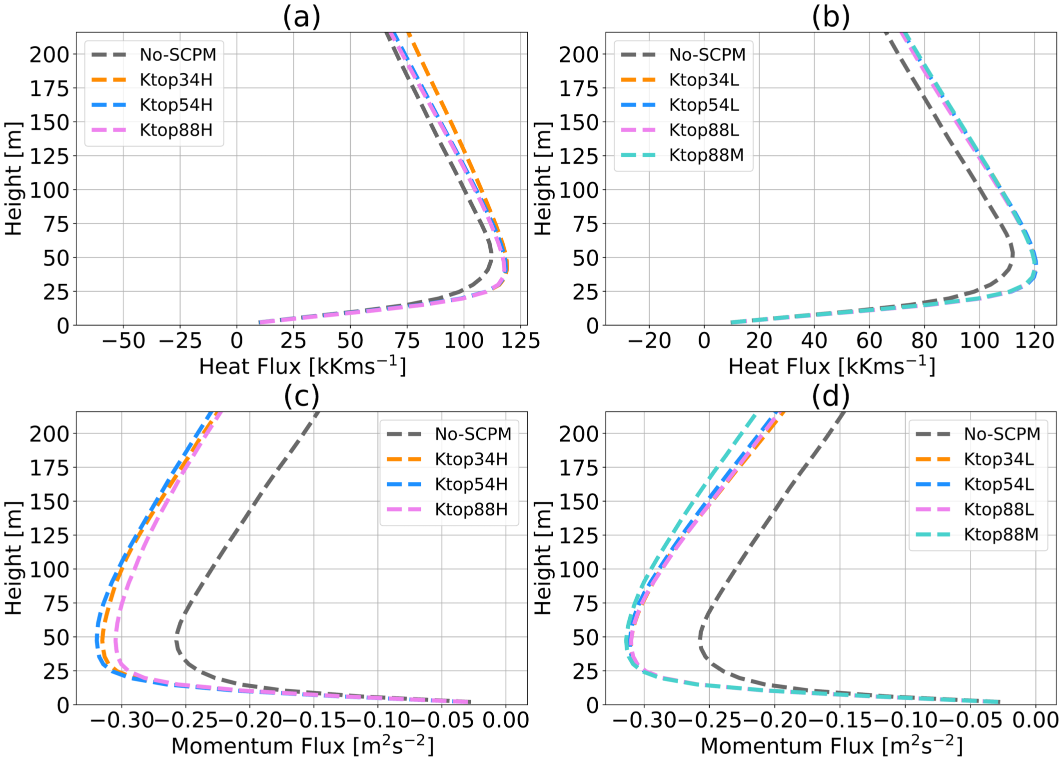

Figure D.2: Heat flux ($\overline{w'\theta'}$) profiles after applying momentum perturbation (SCPM-M) with higher amplitudes of forces (Table 5.1) in the top panels and with lower & medium amplitudes of forces in the bottom panels respectively. Right panels show heat flux ($\overline{w'\theta'}$) profiles up to top of the simulation domain, while left panels represent the same for only up to 216 m. In addition, these profiles are produced in a way that the heat flux ($\overline{w'\theta'}$) are area averaged over entire inner LES domain.

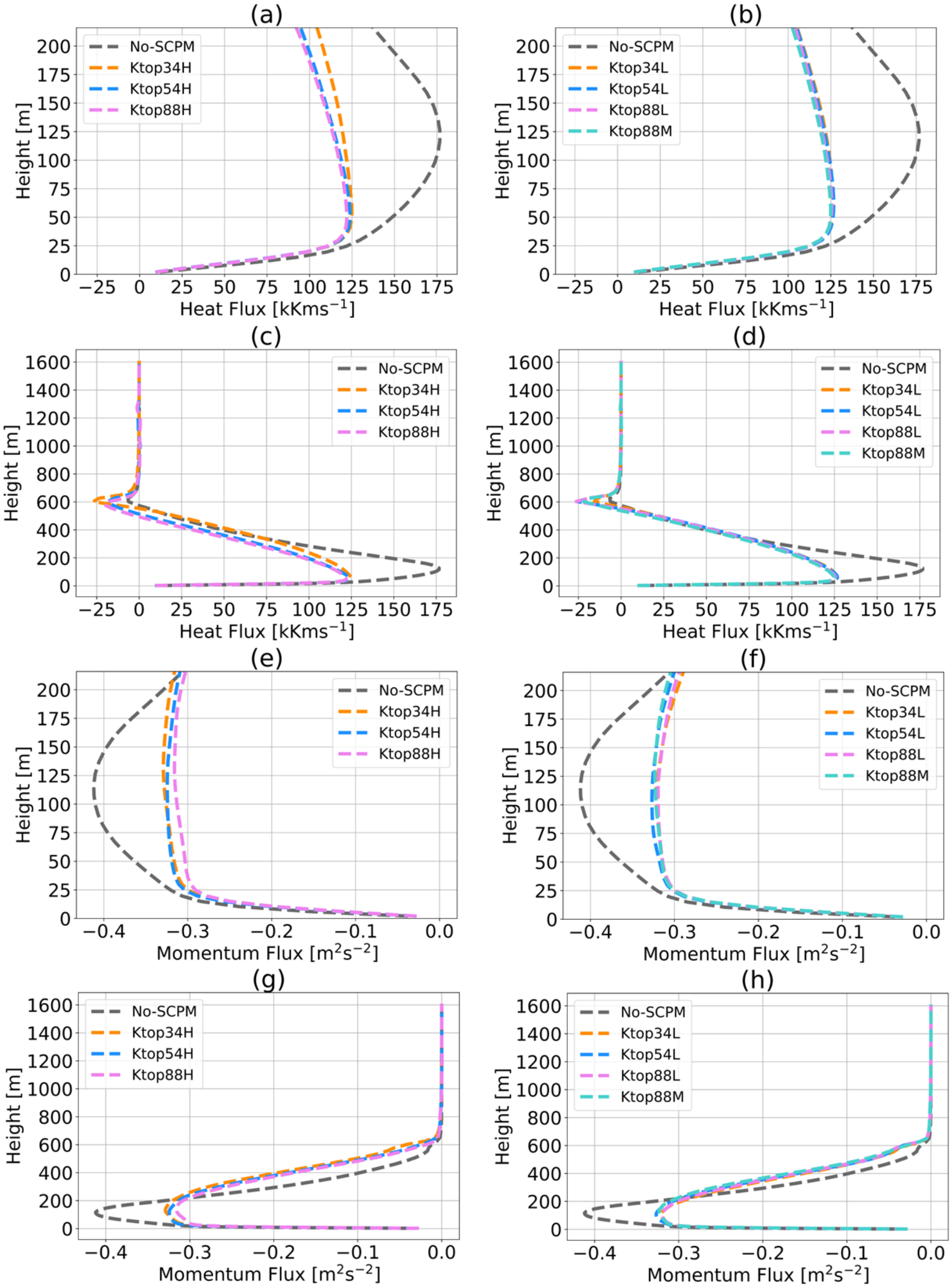

Figure D.3: Heat flux ($\overline{w'\theta'}$) profiles after applying momentum perturbation (SCPM-M) with higher amplitudes of forces (Table 5.1) in the top panels and with lower & medium amplitudes of forces in the bottom panels respectively. Right panels show heat flux ($\overline{w'\theta'}$) profiles up to top of the simulation domain, while left s represent the same for only up to 216 m. In addition, these profiles are produced in a way that the heat flux ($\overline{w'\theta'}$) are area averaged over entire inner LES domain.

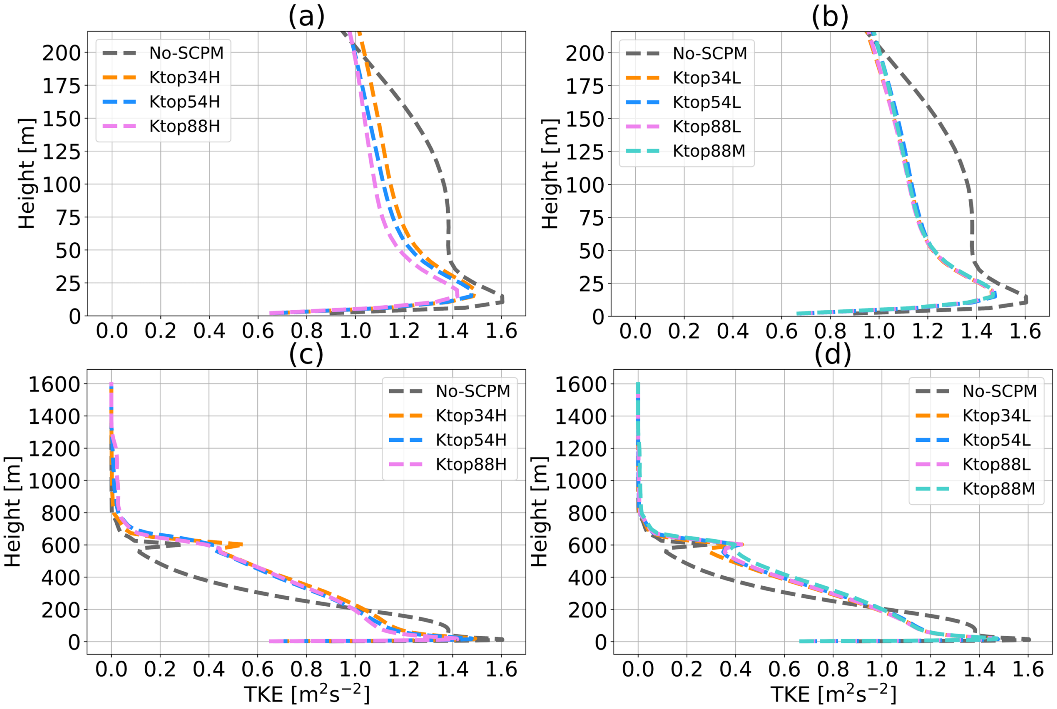

Figure D.4: Turbulence kinetic energy (TKE) profile after applying momentum perturbation with higher amplitude (Table 5.1) in the right panels and lower & medium amplitudes in the left panels respectively. These profiles are generated for TKE that are area averaged over last three quarters of the domain, i.e., all y and x from 2,880 m to 11,520 m with (a) high amplitude SCPM-M up to 216 m, (b) low and medium amplitude SCPM-M up to 216 m, (c) high amplitude SCPM-M up to the top of the inner domain, and (d) low and medium amplitude SCPM-M up to the top the inner domain.

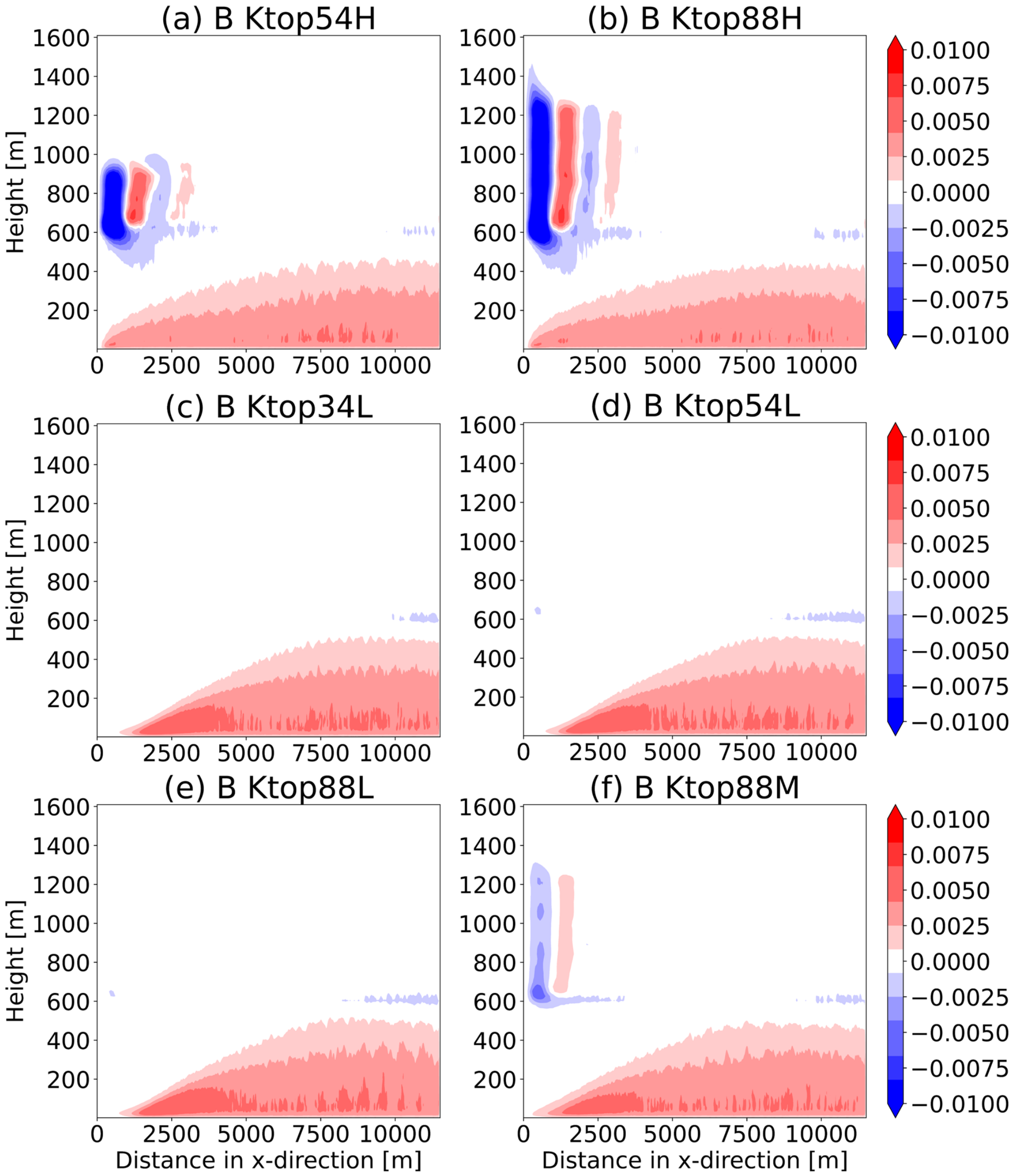

Figure D.5: Y averaged buoyancy term after applying momentum perturbation with higher amplitudes (Table 5.1) with (a) Ktop54H, (b) Ktop88H, (c) Ktop34L, (d) Ktop54L, (e) Ktop88L, and (f) Ktop88M. The color bar corresponds to the magnitude of buoyancy term for panels (a) to (f). These plots are generated for buoyancy terms that are Y averaged over the entire inner domain.

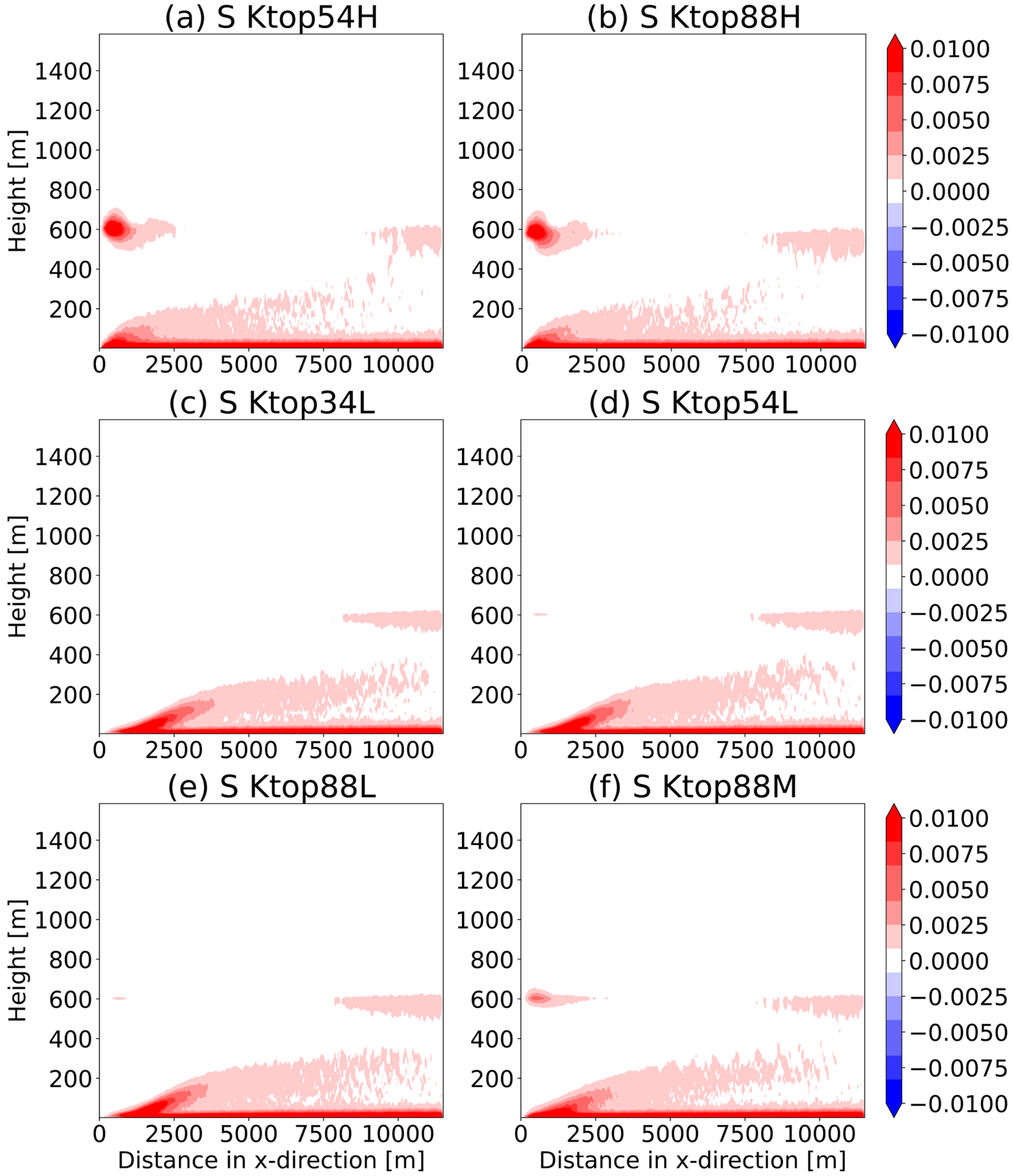

Figure D.6: Y averaged shear term after applying momentum perturbation with higher amplitudes (Table 5.1) with (a) Ktop54H, (b) Ktop88H, (c) Ktop34L, (d) Ktop54L, (e) Ktop88L, and (f) Ktop88M. The color bar corresponds to the magnitude of shear term for panels (a) to (f). These plots are generated for shear terms that are Y averaged over the entire inner domain.

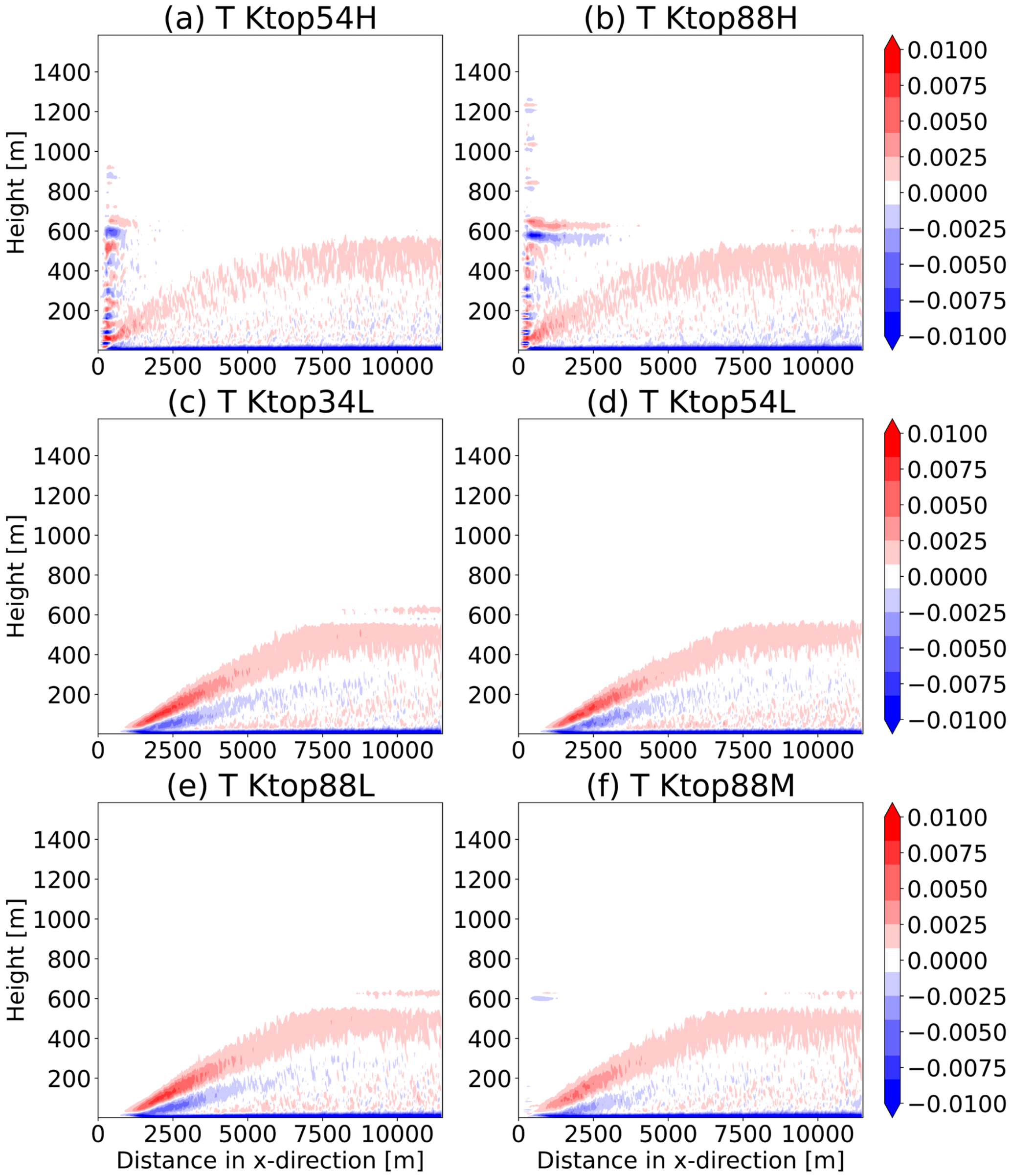

Figure D.7: Y averaged transport term after applying momentum perturbation with higher amplitudes (Table 5.1) with (a) Ktop54H, (b) Ktop88H, (c) Ktop34L, (d) Ktop54L, (e) Ktop88L, and (f) Ktop88M. The color bar corresponds to the magnitude of transport term for panels (a) to (f). These plots are generated for transport terms that are Y averaged over the entire inner domain.

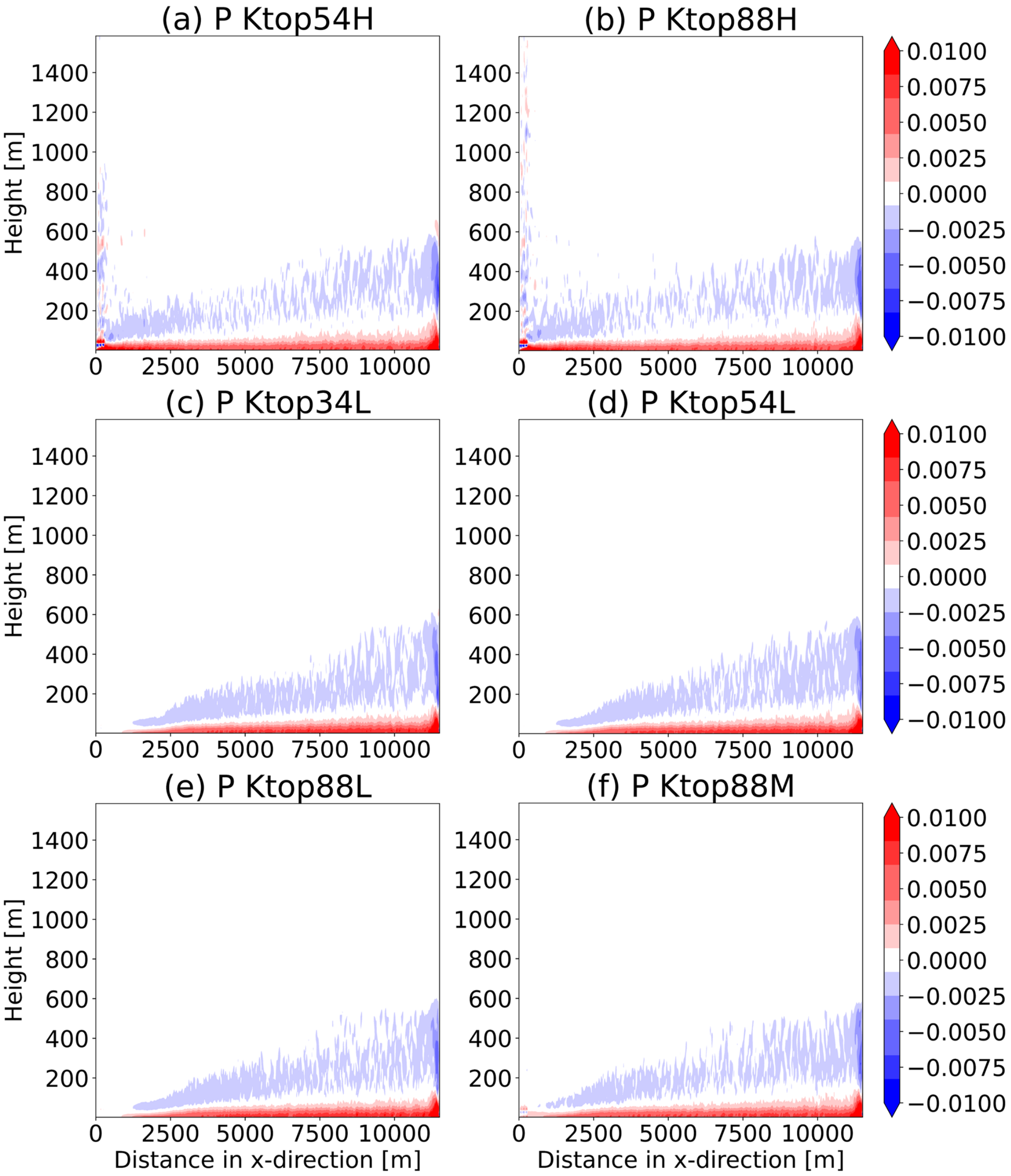

Figure D.8: Y averaged pressure correlation term after applying momentum perturbation with higher amplitudes (Table 5.1) with (a) Ktop54H, (b) Ktop88H, (c) Ktop34L, (d) Ktop54L, (e) Ktop88L, and (f) Ktop88M. The color bar corresponds to the magnitude of pressure correlation term for panels (a) to (f). These plots are generated for pressure correlation terms that are Y averaged over the entire inner domain.

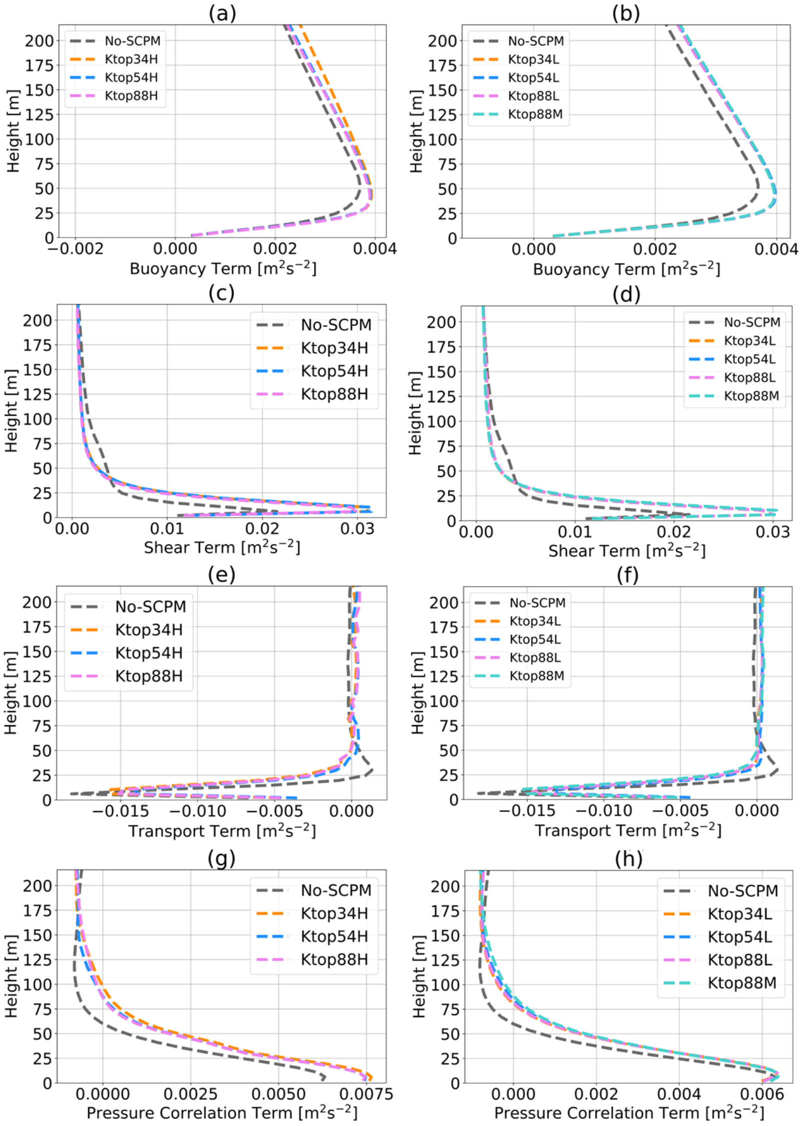

Figure D.9: Area averaged TKE budget terms after applying momentum perturbation following (Table 5.1), for the buoyancy term with (a) higher amplitudes, (b) lower and medium amplitudes; for the shear production term with (c) higher amplitudes (d) lower and medium amplitudes; for the turbulent transport with (e) higher amplitudes (f) lower and medium amplitudes; and for the pressure correlation term with (g) higher amplitudes, (h) lower and medium amplitudes. The plots from (a) to (h) are shown for the entire simulation domain up to 216 m. These profiles are generated for TKE budget terms that are area averaged over the entire inner domain.

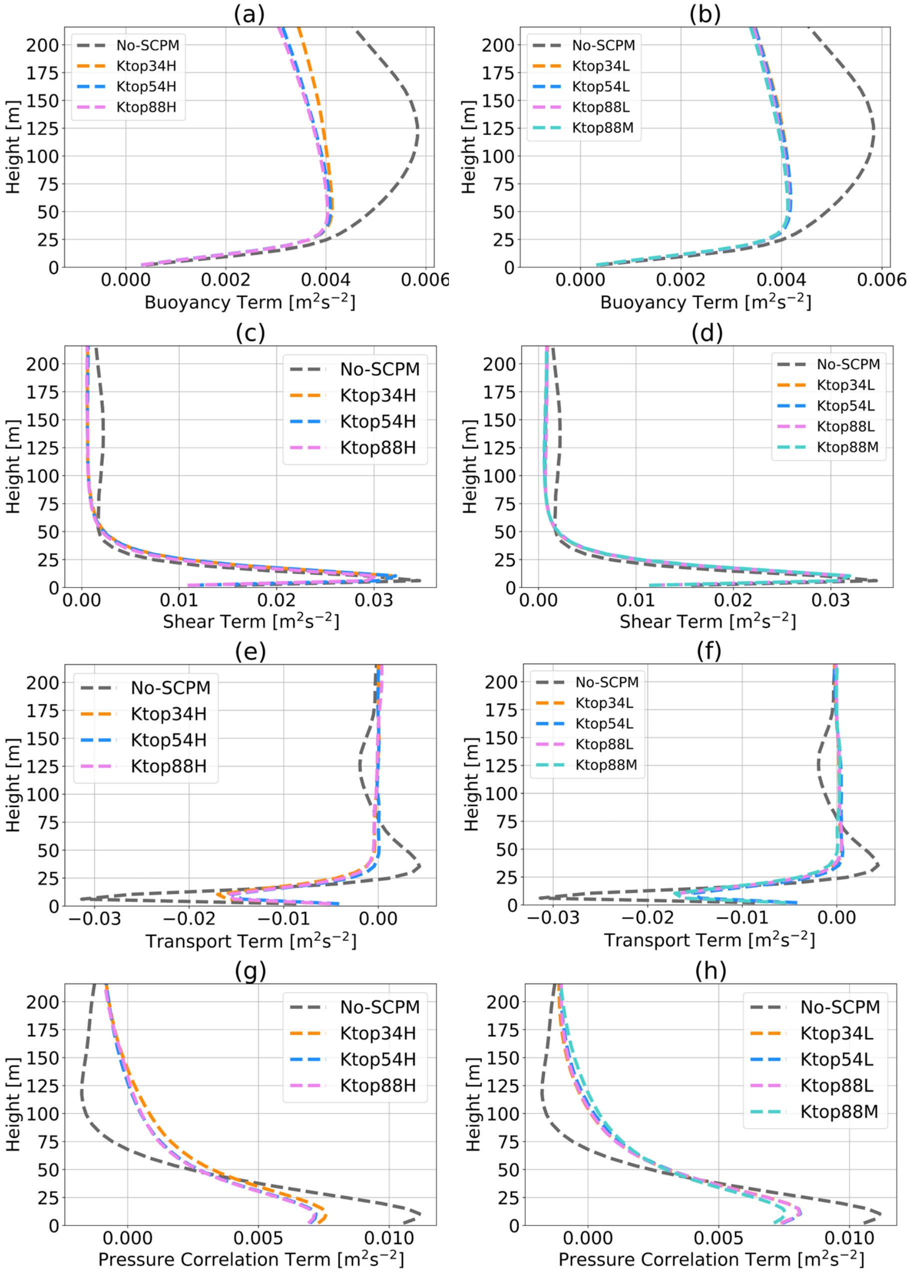

Figure D.10: Area averaged TKE budget terms after applying momentum perturbation following (Table 5.1), for the buoyancy term with (a) higher amplitudes, (b) lower and medium amplitudes; for the shear production term with (c) higher amplitudes (d) lower and medium amplitudes; for the turbulent transport with (e) higher amplitudes (f) lower and medium amplitudes; and for the pressure correlation term with (g) higher amplitudes, (h) lower and medium amplitudes. The plots from (a) to (h) are shown for the entire simulation domain up to 216 m. These profiles are generated for TKE budget terms that are area averaged over last three quarters of the domain i.e., over all y and x from 2,880 m to 11,520 m.

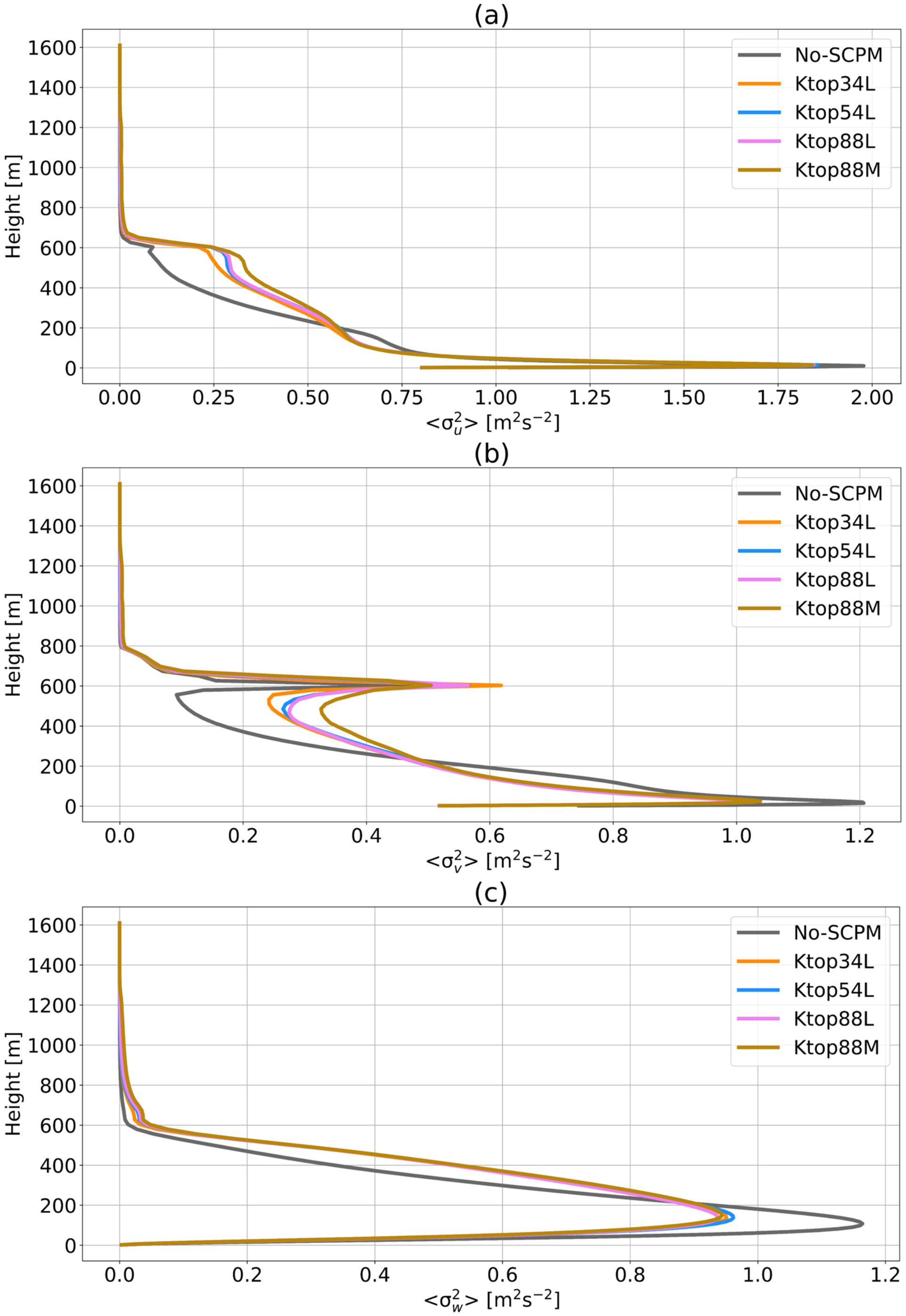

Figure D.11: XY-averaged (a) σ_u^2, (b) σ_v^2, and (c) σ_w^2 for all the cases shown in Table 5.1 for No-SCPM, lower, and medium amplitude simulations i.e., No-SCPM, Ktop34L, Ktop54L, Ktop88L, & Ktop88M. These results are shown from the last simulation period at 20 Z.